TRANSIENT MODELING AND CONTROL OF A SMALL-SCALE AND SELF-PRESSURIZED ELECTROLYSIS SYSTEM

by

Ilias Daniil

to obtain the degree of Master of Science
at the Delft University of Technology,
to be defended publicly on Thursday January 21, 2021 at 10:30 AM.

Student number:	4848659	
Project duration:	February 2020 – January 2021	
Thesis committee:	Dr. ir. J. W. Haverkort ,	TU Delft, supervisor
	Prof. dr. D. J. E. M. Roekaerts,	TU Delft, chair
	Dr. R. Delfos,	TU Delft
	Ir. J. van Kranendonk,	ZEF B.V., supervisor

P&E report number: 3041

TU Delft

Z E F
ZERO EMISSION FUELS

Abstract

Zero Emission Fuels B.V. (ZEF) is a start-up company developing a fully autonomous methanol synthesis micro-plant that will be energy driven by solar panels. The process implements an alkaline water electrolyzer, which supplies the methanol synthesis reactor with hydrogen. The electrolysis system includes a small-scale stack of cells and is designed to operate at 90 ^{o}C and the high pressure of 50 bar, with a 30% potassium hydroxide electrolyte. The system is also self-pressurized through the continuous accumulation of the electrolysis gases in the closed flash separation vessels. To control the process, the company has designed a novel system that aims to maintain the gas pressure at 50 bar and the liquid electrolyte level inside the flash separators at a fixed point.

The present work has two main objectives. The first is to characterize the transient dynamic response of the company's current experimental electrolysis setup under the effect of the operating conditions and control. The second objective is to predict the level of gas crossover that is induced during the system's operation and evaluate the risk of explosive mixtures formation. Two different models were developed to fulfill the research targets.

The first model is based on a 1-d transient hydraulic network analysis. Simulations were conducted using Simulink for a current density range of 500-5000 A$\cdot$m^{-2}. The model predicts the electrolyte flow and pressure response in the various elements and locations of the network respectively, indicating also the oscillatory behavior induced by the operation of the valves. A key finding is the high differential pressure between the stack anodes-cathodes that is caused when the valves open, posing a danger for the integrity of the separators between the half-cells.

The second model was developed in MATLAB and uses the predicted flow response of the first model to estimate the crossovers by solving numerically the unsteady 1-d advection-diffusion equation in the corresponding elements. The effect of the supersaturated electrode boundary layer was also considered as an enhancing parameter of the mass transport through the separators of the cells and a sensitivity analysis was conducted. The main finding is that this parameter has an important effect, especially on the hydrogen crossover inducing 1% higher hydrogen impurity when it is increased by a factor of 10. The crossovers of both hydrogen and oxygen are found to gradually increase and reach an almost stable value under the effect of the control system. A comparison of the model with preliminary experimental data indicates a supersaturation intensity between 5 and 15 times higher than the solubility of the components. In this range, the system will safely operate above 2000 A$\cdot$m^{-2} without the formation of explosive mixtures.

Acknowledgements

With the present work, my academic journey at TU Delft comes to an end and I would like to express my gratitude to everyone who supported my efforts.

Firstly, I would like to thank the ZEF founding members who trusted my skills and offered me the opportunity to be part of the team and conduct my graduation project with them. Special thanks to Jan Van Kranendonk for being a source of inspiration during this project and for his continuous guidance and support.

I would also like to express my gratitude to my supervisor from TU Delft, Dr.i.r J.W. Haverkort. Your expertise and insightful feedback throughout the project helped me understand better any difficult concept, sharpen my thinking and finalize my research.

Finally, I would like to express my gratitude to my parents for their continuous and unconditional support in every step of my life.

Ilias Daniil
Delft, January 2021

CONTENTS

List of Figures

List of Tables

Nomenclature

Abbreviations

AWE	Alkaline Water Electrolysis
CSTR	Continuous Stirred Tank Reactor
DC	Direct Current
FDM	Finite Difference Method
LEL	Lower Explosion Limit
LHS	Left Hand Side
PEM	Proton Exchange Membrane
RHS	Right Hand Side
SOE	Solid Oxide Electrolysis
UEL	Upper Explosion Limit
ZEF	Zero Emission Fuels

Physical Constants

F	Faraday constant: 96485.33 $\mathrm{C \cdot mol^{-1}}$
g	gravitational acceleration: 9.81 $\mathrm{m \cdot s^{-2}}$
R_g	Universal gas constant: 8.314 $\mathrm{J \cdot mol^{-1} \cdot K^{-1}}$

Dimensionless numbers

Pe	Péclet
Re	Reynolds
Sh	Sherwood
Sc	Schmidt

Greek Symbols

Δ	Change in [-]
ϵ	Porosity [-]
ε_{ro}	Roughness [m]
η	Overpotential [V]

λ_D	Linear friction coefficient [-]
λ_L	Local friction coefficient [-]
μ	Dynamic viscosity [$\mathrm{Pa \cdot s}$]
ν	Stoichiometric coefficient [-]
ν_L	Kinematic viscosity [$\mathrm{m^2 \cdot s^{-1}}$]
ρ	Density [$\mathrm{kg \cdot m^{-3}}$]
σ	Surface tension [$\mathrm{N \cdot m^{-1}}$]
τ	Tortuosity [-]
τ_w	Shear stress [Pa]
ω	Acentric factor [-]

Roman Symbols

A	Area [$\mathrm{m^2}$]
a	Acceleration [$\mathrm{m \cdot s^{-2}}$]
c	Concentration [$\mathrm{mol \cdot m^{-3}}$]
c^*	Solubility [$\mathrm{mol \cdot m^{-3}}$]
D	Diffusivity [$\mathrm{m^2 \cdot s^{-1}}$]
d	Diameter [m]
f_G	Gas evolution efficiency [-]
F	Force [N]
H	Enthalpy [$\mathrm{kJ \cdot mol^{-1}}$]
h	Height [m]
I	Current [A]
j	Current density [$\mathrm{A \cdot m^{-2}}$]
K	Permeability [$\mathrm{m^2}$]
K_H^{cc}	Dimensionless Henry constant [-]
K_H^{cp}	Henry constant [$\mathrm{mol \cdot m^{-3} \cdot bar^{-1}}$]
K_H^{px}	Henry constant [bar]
k	Mass transfer coefficient [$\mathrm{m \cdot s^{-1}}$]
k_S	Sechenov constant [-]

k_v	Valve flow coefficient [$Nm^3 \cdot h^{-1}$]
L	Length [m]
$\dot{m}$	Mass flow rate [$kg \cdot s^{-1}$]
$\dot{N}$	Molar flow rate [$mol \cdot s^{-1}$]
$\dot{n}$	Molar flux [$mol \cdot s^{-1} \cdot m^{-2}$]
P	Pressure [Pa or bar]
p	Partial pressure [Pa or bar]
$\dot{Q}$	Volumetric flow rate [$m^3 \cdot s^{-1}$]
R	Resistance [Ω]
r	Radius [m]
S	Entropy [$kJ \cdot kg^{-1} \cdot K^{-1}$]
SF	Supersaturation factor [-]
SG	Specific gravity [-]
T	Temperature [K]
t	Time [s]
U	Electric potential or voltage [V]
u	Velocity [$m \cdot s^{-1}$]
V	Volume [m^3]
v	Molar volume [$m^3 \cdot mol^{-1}$]
w	Mass fraction [%]
y	Tank liquid height [m]
$\dot{y}$	Tank liquid velocity [$m \cdot s^{-1}$]
$\ddot{y}$	Tank liquid acceleration [$m \cdot s^{-2}$]
z	Number of transferred electrons [-]
G	Gibbs free energy [$kJ \cdot mol^{-1}$]

Subscripts

an	anode
br	break-off
c	critical

ca	cathode
conv	convective
diff	diffusive
e	electrode
eb	electrode micro-convection
ec	electrode macro-convection
eff	effective
g	gas
gen	generated
l	liquid
oc	open circuit
p	pipe
pa	pipe anode
pc	pipe cathode
rev	reversible
sat	saturation
sep	separator
t	tank
tn	thermoneutral

Chemical

CH_3OH	Methanol
CO_2	Carbon dioxide
H_2	Hydrogen
H_2O	Water
KOH	Potassium hydroxide
$NaOH$	Sodium hydroxide
O_2	Oxygen
OH	Hydroxide

1

INTRODUCTION

1.1. HYDROGEN ECONOMY

After the industrial revolution in the 18th century, the global economy experienced rapid changes and became strongly based on industry and machine manufacturing. The development in many sectors improved the living standards and the world population is increasing year after year, resulting in growing energy demand. It is estimated that in 2050, around 9 billion people will consume 30 TW of energy, while half of this amount was consumed by 7 billion people in 2011 [14]. Most of the energy produced today comes from the utilization of fossil fuels that are responsible for large greenhouse gas emissions and contribute to the crucial phenomenon of global warming [24]. The environmental concern along with the gradual depletion of fossil fuel sources have shifted the interest to alternative and sustainable solutions.

Hydrogen is the most abundant substance in the universe. It was initially observed at the beginning of the 16th century by the Swiss physician Paracelsus during an experiment when he added iron into sulfuric acid and noticed that the produced gas in bubble form was ignitable. However, the official detection of hydrogen is attributed to the English scientist Henry Cavendish in 1766, when he carried out similar experiments and recognized that the byproduct bubbles from the reaction of zinc with hydrochloric acid were a distinct element. He also proved that by burning these bubbles, water was produced and put an end to the belief that water was a distinct substance. Later in 1788, using the work of Cavendish, the French chemist Antoine Lavoisier named the new element hydrogen [64].

Considering the need to build an environmentally friendly future with less dependence on fossil fuels, hydrogen is evaluated as an effective energy bearer that can be utilized to replace fossil fuels in many industrial processes. According to literature [29], the main applications today that require hydrogen are oil refining and ammonia production, with 70Mt of pure hydrogen demand, while around 45 Mt are used in the fuel production (methanol, syngas) and iron industries. Despite the abundance of hydrogen in the universe, it does not exist in pure form on earth but as a component in chemical compounds [14]. Thus, what is also important in the 'green' transition is the method of hydrogen production and its environmental footprint. Today, half of the global hydrogen needs are covered from natural gas reforming and around 30 % from oil reforming [18], processes that are responsible for greenhouse gas emissions. However, hydrogen can be produced in a sustainable way via the water electrolysis process driven by renewable energy sources [5]. Such technology is applied by Zero Emission Fuels as a subsystem in an innovative power to gas project.

1.2. ZERO EMISSION FUELS B.V.

Zero Emission Fuels B.V. (ZEF) is a startup company in the Netherlands developing a methanol production micro-plant that can be adapted directly at the backside of a single solar panel. The company's vision is that big solar farms with a large number of micro-plants will be developed instead of having a single methanol synthesis plant. The advantages of this strategy are less complexity of the system, dynamic operation and potential for mass production of micro-plants, which will result in lower capital costs [4]. Figure 1.1 depicts a simplified process diagram of the micro-plant.

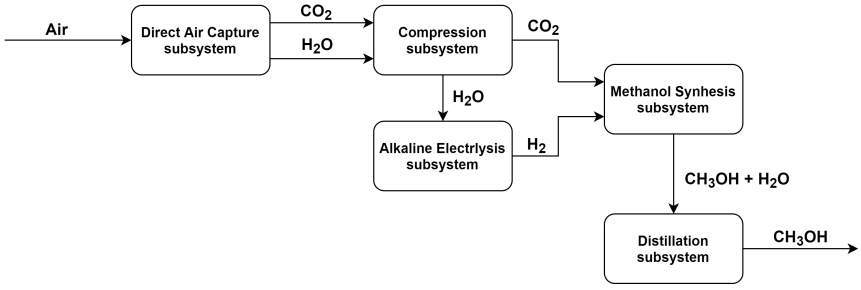

Figure 1.1: ZEF process diagram.

The process starts with the direct air capture subsystem. It is used to capture carbon dioxide and moisture (water) from the atmospheric air. Then, both components are driven to the compressors, where the pressure is increased to 50 bar (this pressure is preferred to enhance the kinetics of the methanol synthesis reaction). The compressed water is then guided to the alkaline electrolysis unit while the carbon dioxide is supplied to the reactor. The electrolysis unit consists of three smaller subsystems: a degasser that is using the produced oxygen to 'clean' the water stream from any residual carbon dioxide, the electrolyzer (known also as 'stack') that is splitting water into hydrogen and oxygen and two flash separators that separate the produced gases from the alkaline solution. The produced hydrogen along with carbon dioxide are fed to the methanol synthesis reactor where a mixture of methanol and water is produced. The final stage of the process is a distillation subsystem where methanol is separated from water with high purity. All the energy needs of the micro-plant are covered with electricity supplied by the solar panel.

ZEF electrolysis system specifications:

The alkaline electrolysis unit of ZEF is a core part of the micro-plant as it supplies the reactor with hydrogen, one of the two components needed to produce methanol. The system's specifications are summarized in table 1.1.

The electrolyzer is a stack of 18 cells designed and compressed in a way to ensure that it can withstand the high pressure of 50 bar and remain leak-tight during operation. Regarding the cells, a zero-gap bipolar configuration is selected, meaning that the separators and electrodes are in contact reducing the ohmic losses caused by the electrolyte resistance. Furthermore, a Zirfon Perl UTP 500 membrane with 0.5 mm thickness is applied to separate the oxygen and hydrogen evolution cell compartments. As it is reported in the manufacturer data sheet [1], this product offers high chemical stability, low ionic resistance and can withstand strong alkaline solutions and high temperatures resulting in an enhanced electrolysis performance.

Table 1.1: ZEF electrolysis system specifications.

Operating pressure	50	bar
Operating temperature	90	^{o}C
Operating cell potential	2	V
Operating current density	3330	$A \cdot m^{-2}$
Cell geometry	Zero-gap	-
Cell net area	63.36	cm^2
Electrolyte concentration	30	%wt
Cell separator type	Zirfon Perl UTP 500	-
Number of cells	18	-

The high normal operating pressure of 50 bar is an important parameter that affects the whole electrolysis system and its safety. To keep the pressure variation at a fixed level and also ensure that the flash tanks will not dry out of electrolyte, the company has implemented a novel system with liquid level sensors, pressure sensors and purging valves, which is illustrated and analytically described in chapter 3. In typical industrial electrolyzers, a pump is used for the electrolyte circulation. However, the ZEF system does not include a pump and the flow is naturally induced due to the convection effect caused by the bubble evolution and also due to the gas pressure variations inside the flash tanks (caused by the gas accumulation and purging valves operation).

1.3. THESIS OBJECTIVE AND METHODOLOGY

A crucial phenomenon that is related to the safe operation of AWE systems is the level of gas crossover, meaning the quantity of a produced gas that can cross permeate and mix with the opposite side gas, posing a risk of falling into the explosive limits. The evolving gases can crossover to the opposite side in dissolved form through the separators of the cells and electrolyte flow inside the piping network, especially in the ZEF case where a mixing electrolyte cycling strategy is adopted.

With the implemented control strategy, ZEF argues that the phenomenon of crossover can be limited since the regular operation of the valves would also purge some of the opposite side accumulated gas, tending to stabilize its quantity during the normal operation in a minute or hour time scale, depending on the operational conditions. The level of gas crossover and how is affected by operational and control parameters of the system is the main target to be evaluated in this thesis. Except for this phenomenon, the effect of the valve operation on the electrolyte flow and possible risks will be examined.

Consequently, the graduation project is divided into two main tasks. The first one focuses on characterizing the transient dynamic behavior of the AWE system under the effect of the relevant physical phenomena and the control system response. This scope is served by a transient hydraulic network model that simulates the operation during the startup (pressure increase till 50 bar) and part of the main operating window (pressure maintained at 50 bar) until the system presents a stable behavior. The model predicts the flow velocity in the different elements (pipes, half-cells, flash tanks), the pressure in relevant points, estimates the electrolyte level and gas density in the flash tanks and gives

an insight on the oscillating phenomena that can occur by the opening of the valves. The second task focuses on the gas crossover prediction. Using the computed hydraulic network parameters from the first model (pipe velocities, pressure difference between half-cells and valve response), transient mass transfer equations (using appropriate numerical schemes) are solved to evaluate the level of dissolved components ending up to the opposite side tank.

Taking into consideration the aforementioned targets, the following research questions have been developed:

1. What is the dynamic response of the ZEF electrolysis system in a time frame including the pressure build-up period and part of the main operating state?
2. Does the valve opening pose risks affecting the integrity of the system?
3. What is the level of crossover induced by the operating and controlling parameters? Is the company's hypothesis about the limited crossover effect fulfilled?
4. How are the dynamic response and crossovers affected if the system operates at different current densities?

1.4. REPORT STRUCTURE

This thesis report is divided into 7 main chapters. **Chapter 1** was the introduction part of the thesis, where general information about the company and project were given and also the research questions and methodology were stated. The following chapters are structured as mentioned below:

- **Chapter 2** includes general theoretical knowledge about alkaline water electrolysis, describes the way that dissolved gases can crossover to the opposite side and analyzes the physical mechanisms that affect the phenomenon. Moreover, relevant previous work done in transient modeling and crossovers is illustrated.
- **Chapter 3** presents an overview of the ZEF system that was modeled, describes how the control system operates and includes geometrical and operational parameters that were used in the models.
- **Chapter 4** provides an analytical description of the developed models, including the assumptions made, the governing equations and some information on the used software.
- **Chapter 5** provides and analyzes the results of the project. A comparison with preliminary experimental data is also conducted.
- **Chapter 6** summarizes the main conclusions of the research.
- **Chapter 7** includes recommendations for improvements, extension of the current work and advice for possible system modifications and upgrades based on the results.

2

THEORY

2.1. WATER ELECTROLYSIS

Electrolysis is a chemical process used to divide water molecules into oxygen and hydrogen by applying electric current according to the following reaction, which is global and independent from the selected method.

$$H_2O(l) \rightarrow H_2(g) + \frac{1}{2}O_2(g) \tag{2.1}$$

A typical water electrolysis system consists of two metallic electrodes soaked inside an electrolyte solution. The electrodes are connected to a DC power source and after a certain value of the supplied potential, oxygen is produced at the positively charged electrode (anode), while hydrogen is formed at the negatively charged electrode (cathode). Furthermore, the two sides are usually separated with a diaphragm (membrane). The role of this separator is to prevent the mixing of the evolving gases in bubble form while being permeable to ions and water molecules [44]. A simple schematic of the basic electrolysis process is presented in figure 2.1.

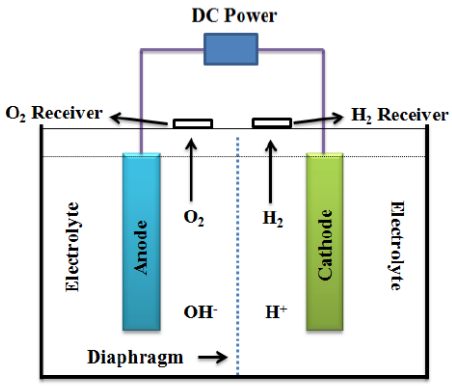

Figure 2.1: Basic electrolysis process. [42]

Today, three main water electrolysis techniques have been developed: alkaline water electrolysis (AWE), proton exchange membrane (PEM) electrolysis and solid oxide electrolysis (SOE). AWE is the oldest and most mature technology and together with PEM are commercially available, while SOE electrolyzers are promising but not widely used [12]. Alkaline electrolyzers will be discussed in the following section, as this is the technology adopted by ZEF to produce hydrogen.

2.2. ALKALINE WATER ELECTROLYSIS BASIC THEORY

Alkaline electrolyzers are widely used in industry. Their operation follows the same principle of a typical electrolysis system. The electrodes are usually made from Nickel based alloys that offer high activity and low cost [51]. As for the electrolyte, the most common selection is an aqueous potassium hydroxide (KOH) solution with 25 – 30 %wt concentration, which is not corrosive for the electrodes and provides high ionic conductivity [63]. The hydrogen production occurs at the cathode of a single cell (reduction reaction), where the electrons split water into hydrogen and hydroxide anions, while the oxygen evolution (oxidation reaction) happens at the anode, where the hydroxide anions recombine after passing through the separator to form oxygen and water. The chemical reactions that describe the gases evolution in the alkaline electrolyzer cells are the following:

$$\text{Cathode}: 2H_2O + 2e^- \rightarrow H_2 + 2OH^- \tag{2.2}$$

$$\text{Anode}: 2OH^- \rightarrow \frac{1}{2}O_2 + H_2O + 2e^- \tag{2.3}$$

From a thermodynamics perspective, the split of water into oxygen and hydrogen is an endothermic process that requires energy in the form of electricity or heat in order to start and be maintained. This minimum energy barrier for water decomposition is given by the Gibbs free energy equation:

$$\Delta G^o = \Delta H^o - T \cdot \Delta S^o \tag{2.4}$$

where G^o is the standard Gibbs free energy, H^o is the water energy of formation, T is the temperature and S^o is the ideal gas entropy. At standard conditions (T =298.15 K and P =1.01325 bar) the Gibbs free energy of water is -237.23 kJ·mol^{-1} (ΔH^o =-285.83 kJ·mol^{-1}, ΔS^o =-0.163 kJ·mol^{-1}·K^{-1}). The standard reversible cell potential of water electrolysis is estimated using the change of Gibbs standard free energy with the following formula:

$$\Delta G^o = -z \cdot U^o \cdot F \tag{2.5}$$

where z is the number of electrons transferred per hydrogen molecule ($z = 2$) and F is the Faraday constant. Therefore, the reversible cell potential at standard conditions is 1.23 V. Furthermore, an additional amount of heat has to be provided to maintain a constant temperature. This heat is equivalent to 0.25 V and thus, the minimum supplied voltage to maintain isothermal conditions in the cell is 1.48 V and is called thermoneutral potential [43]. If the supplied electrical potential is above the thermoneutral, the reaction becomes exothermic resulting in energy production in the form of heat at the electrodes with the restriction that the temperature of the cell does not change [65].

From the aforementioned theory, it is clear that the electrolysis process can occur with a supplied electrical potential equal to the thermoneutral. However, in a real system, there are sources of irreversibilities resulting in slow reactions. To overcome these barriers and enhance the kinetics, an additional electrical potential over the thermoneutral should be applied. This overpotential is an aggregation of the following contributions [63]:

i Activation energy of the reactions at the two electrodes (anode and cathode).

ii Losses caused by bubbles covering the electrodes, which enhance the activation losses.

iii Losses by the resistance of the electrolyte.

iv Losses by the resistance of the separator.

v Losses caused by electrical connections.

The losses mentioned at ii, iii, iv and v are usually referred as ohmic losses. Therefore, the actual voltage of an electrolysis cell is described by the following equation:

$$U_{\text{cell}} = U_{\text{oc}} + \eta_{\text{an}} + \eta_{\text{ca}} + R_{\text{cell}} \cdot j \cdot A_{\text{cell}} \tag{2.6}$$

where U_{oc} is the open circuit potential, η_{an}, η_{ca} are the anode and cathode overpotentials, R_{cell} is the total cell ohmic resistance, j is the supplied current density and A_{cell} is the net cell electrolysis area. Figure 2.2 depicts how the current density affects the various losses of an electrolyzer operating at environmental temperature. The anode overpotential is generally higher than cathode overpotential, while the ohmic losses become dominant at high current densities with a greater increase [40].

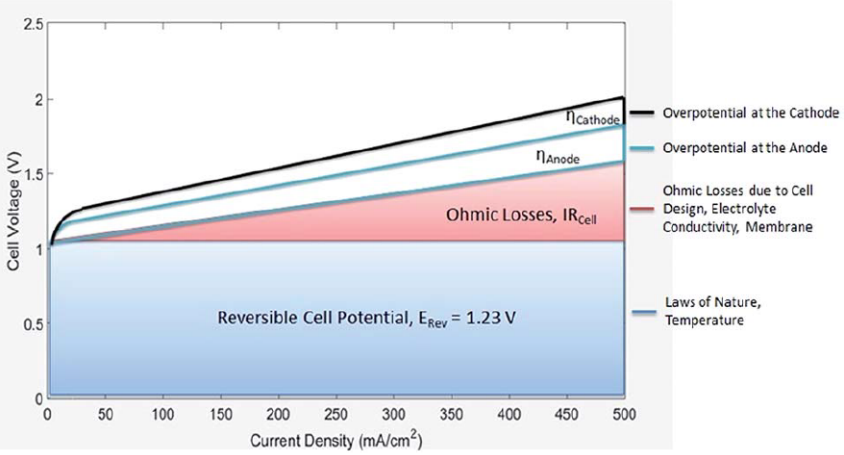

Figure 2.2: Effect of losses on cell electrical potential at different current densities. [40]

Two other factors that affect the total cell voltage are the operating temperature and pressure. Several semi-empirical models have been developed in order to estimate these effects. Ulleberg [66] investigated the temperature effect and proved that the total cell voltage decreases at higher temperatures. Sanchez et al [52] updated Ulleberg's model to take into consideration the operating pressure and observed that the total cell voltage does not change significantly at higher pressures and is slightly increased.

The theoretical molar fluxes of the produced gases in an alkaline electrolysis cell can be calculated using the law of Faraday as [6]:

Anode:

$$\dot{n}_{O_2} = \frac{\nu_{O_2}^{\text{an}} \cdot j \cdot A_{\text{cell}}}{z \cdot F} \tag{2.7}$$

Cathode:

$$\dot{n}_{H_2} = \frac{\nu_{H_2}^{ca} \cdot j \cdot A_{cell}}{z \cdot F} \tag{2.8}$$

2.3. CELL GEOMETRY OF ALKALINE ELECTROLYZERS

Regarding the cell configuration of alkaline electrolyzers, traditionally the cells are assembled in a way forming a stack. There are two different designs that are used to form electrolysis stacks.

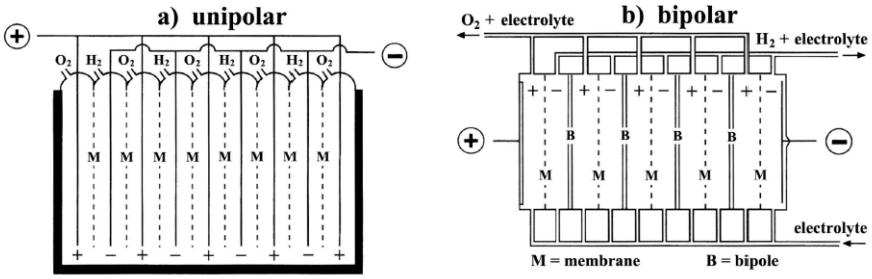

Figure 2.3: Alkaline electrolysis stack design: (a) unipolar and (b) bipolar. [44]

UNIPOLAR (OR MONOPOLAR) DESIGN:

In electrolyzers with unipolar configuration, the different cells are connected in parallel so that each cell has the same voltage as the whole stack, while the sum of individual cell's current is equal to the total stack current. More specifically, all the positive and negatively charged electrodes are interconnected with the DC source, while porous membranes are used to separate them. Moreover, the same chemical reactions occur at both sides of each electrode [44]. The unipolar configuration has some advantages over the bipolar regarding the manufacturing procedure. It is less complex during fabrication and assembly with low upkeeping needs. Furthermore, monopolar electrolyzers have little current losses (leaking currents) [35]. However, the main drawback of the unipolar configuration is that low voltage operation requires more transformation [63].

BIPOLAR DESIGN:

In bipolar electrolyzers, the cells are connected in series. This is the opposite state from the unipolar configuration due to all cells have the same current, while the sum of their voltages is equal to the total voltage supplied to the stack. Furthermore, different reactions take place at each side of an electrode in a way that one side has the role of the cathode, while the opposite side serves as the anode of the following cell. As for the interconnections, only two electrodes (these at the edges) are directly connected to the DC source, while electricity is transferred through the cells via metal 'bipolar' plates that are used for the separation of the cells. Bipolar electrolyzers have also porous membranes to separate the reaction chambers [44]. Compared to unipolar electrolyzers, the bipolar require a more complex design as there is a possibility of gas, ions and current leaking between the adjoining cells [63].

Another geometrical aspect that is taken into consideration is the gap between the electrodes and the separator. Generally, the cells of many commercial alkaline electrolyzers have a layout consisting of two solid electrodes placed at a distance from the separator, while the gap between them is filled with electrolyte. As mentioned in section 2.2, the electrolyte contributes to ohmic losses and consequently, this electrolyte filled gap increases the ohmic resistance of the cells [40]. An alternative cell design, named zero-gap, includes two porous electrodes that are in contact with the cell membrane in a way that their distance is equal to the separator thickness. The electrodes have a porous structure to let the electrolyte pass through. In traditional alkaline electrolyzers, the electrode distance is usually greater than 2 mm [40], while for the zero-gap setup and Zirfon Perl separator, it is reduced to 0.5 mm [45]. The combination of porous electrodes with the zero-gap contributes also to the decrease of losses caused by electrode bubble coverage [40].

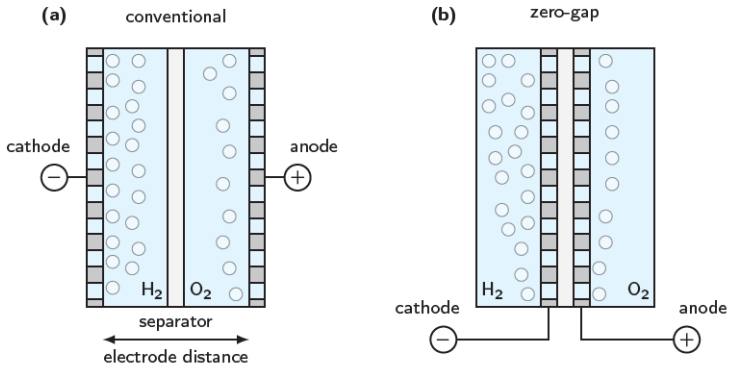

Figure 2.4: (a) traditional vs (b) zero-gap alkaline electrolyzer design. [11]

2.4. GAS CROSSOVER IN ALKALINE ELECTROLYZERS

In a perfect electrolysis system, the produced gases would be released with 100% purity. However, this does not happen in reality as cross-contamination of oxygen into hydrogen and vice versa is being observed. This phenomenon, called 'gas crossover', is affected by several parameters such as the operating conditions (temperature/pressure), the properties of cell separators and the electrolyte cycling strategy.

During normal operation, it is important to monitor the purity of the evolving gases at the collecting reservoirs to ensure that the gas mixtures remain out of the explosive limits, determine the shutdown conditions and thus bear out the safe operation [26]. Schroder et al [47] performed experiments to estimate the H_2/O_2 mixtures explosive limits at both low and high temperatures and pressures. According to their findings, for 80 ^{o}C and 50 bar operating conditions (relevant for ZEF system), the LEL and UEL are 5.3 mol% H_2 and 95 mol% H_2 respectively.

The gas crossover can be categorized according to the way it is happening and the involved physical mechanisms. Regarding the way, the produced gases can crossover in a dissolved form inside the electrolyte either through the cell separators or through the mixing electrolyte cycles. The electrolyte mixing is a common method followed to maintain a balance of the electrolyte concentration between the anodes/cathodes. More specifically, water consumption in the cathodes (eq 2.2) causes local concentration differences and

thus there is a point in the system where the electrolyte cycles are mixed. Furthermore, extra water is added in order to replenish the consumed quantity [22]. Two main physical mechanisms trigger the gas crossover in an alkaline electrolyzer [58]:

- Mass diffusion caused by concentration differences of the dissolved gases.
- Mass convection due to pressure gradients along the flow and electro-osmosis.

In the following subsections, the effect of the aforementioned mechanisms on the gas crossover through cell separators and electrolyte mixing will be further explained.

2.4.1. GAS CROSSOVER THROUGH THE SEPARATOR

In an alkaline electrolysis cell, the anodic and cathodic compartments include O_2 and H_2 in bubble form (gas phase) and also dissolved inside the electrolyte with a concentration equal to their solubility or slightly supersaturated [27]. The separator is placed between the half-cell compartments to block the mixing of the evolving components. However, because of its porous structure, it is possible that the dissolved gases can permeate. Trinke et al [58] studied the crossovers in PEM and alkaline electrolyzers and reported that the dissolved gas permeation is been triggered by concentration difference across the separator (mass diffusion), differential pressure of anode/cathode (mass convection) and also through a phenomenon called electro-osmotic drag (considered in mass convection mechanism).

A. MASS DIFFUSION:

Mass diffusion can be estimated using Fick's laws [45]. Under the assumption of steady-state, when the concentration gradient of dissolved gases is constant across the separator and there is not pressure difference between the half-cell compartments (meaning no flow), molar flux is calculated using the below formula (Fick's first law of diffusion):

$$\dot{n}_i^{\text{diff}} = -D_i^{\text{eff}} \cdot \frac{\partial c_i}{\partial x} = -D_i^{\text{eff}} \cdot \frac{c_{i,\text{ca}} - c_{i,\text{an}}}{L_{\text{sep}}} \tag{2.9}$$

where i refers to the examined component, D_i^{eff} is the effective diffusivity of i in the separator, L_{sep} is the thickness of separator, while $c_{i,\text{ca}}$ and $c_{i,\text{an}}$ are the concentrations of i in the cathode and anode respectively (if the component is moving from anode to cathode). For transient problems, the second law of Fick, which describes the rate of concentration accumulation inside the separator as proportional to the local curvature of concentration gradient, is used:

$$\frac{\partial c_i}{\partial t} = D_i^{\text{eff}} \cdot \frac{\partial^2 c_i}{\partial x^2} \tag{2.10}$$

The effective diffusivity is a property based on the diffusion coefficient of the examined component in the electrolyte, modified in a way that the geometrical structure of the separator is taken into account [21]:

$$D_i^{\text{eff}} = D_i \cdot \frac{\varepsilon}{\tau} \tag{2.11}$$

where ε is the porosity of the separator and τ the tortuosity. Data for the porosity are usually provided by the manufacturers (i.e. for Zirfon Perl UTP 500 used by ZEF the porosity is 0.5), while for the tortuosity, no experimental data where found in literature. However, Haug et al [22] combined data from the work of Schalenbach et al [45] and estimated a value of 3.14. Another option to calculate the tortuosity of the separator is to use the model proposed by Bruggeman [57]. He assumed that the mass transport barriers

through a porous material have the form of spheres or cylinders and derived a correlation that estimates the tortuosity by using the porosity of the material:

$$\tau = \begin{cases} \varepsilon^{-0.5}, \text{ spheres} \\ \varepsilon^{-1}, \text{ cylinders} \end{cases} \tag{2.12}$$

B. MASS CONVECTION OR ADVECTION:

Mass convection is a second physical mechanism that is responsible for gas crossover through the separator. In general, the steady-state and transient advection equations are listed below:

$$\dot{n}_i^{\text{conv}} = u \cdot c_i \tag{2.13}$$

$$\frac{\partial c_i}{\partial t} + u \cdot \frac{\partial c_i}{\partial x} = 0 \tag{2.14}$$

where u is the velocity of electrolyte moving perpendicular through the separator. According to [58], two possible mechanisms that can cause advective mass movement through the separator are the differential pressure between the anode/cathode of a cell and the electro-osmotic drag.

Anode/cathode differential pressure:

During the operation of an alkaline electrolyzer, the control valves that are used to maintain a pressure balance in the system may cause pressure gradients between the cell anodes/cathodes, which force the electrolyte and thus dissolved species to permeate through the separator. By knowing the pressure difference, it is possible to estimate the electrolyte velocity through the separator using the Darcy equation [45], [58]:

$$\dot{Q} = \frac{K_{\text{sep}} \cdot A_{\text{sep}}}{\mu \cdot L_{\text{sep}}} \cdot \Delta P \tag{2.15}$$

where $\dot{Q}$ is the volumetric flow rate, K_{sep} is the permeability of the separator, A_{sep} is the cross section area of the separator, L_{sep} is the thickness of the separator, μ is the dynamic viscosity of the electrolyte and ΔP is the absolute pressure difference between the anode and cathode. The permeability of the separator can be calculated using Kozeny equation [39]:

$$K_{\text{sep}} = \frac{\varepsilon \cdot d_{\text{pore}}^2}{32 \cdot \tau} \tag{2.16}$$

where d_{pore} is the pore diameter.

Using equation 2.15, the advective velocity is equal to the product of volumetric flow rate and cross section area. Consequently, the unsteady advection equation 2.14 becomes:

$$\frac{\partial c_i}{\partial t} + \frac{K_{\text{sep}} \cdot \Delta P}{\mu \cdot L_{\text{sep}}} \cdot \frac{\partial c_i}{\partial x} = 0 \tag{2.17}$$

Electro-osmotic drag and flow:

Convective mass transfer of dissolved gases through the separator can also be triggered by the phenomenon called electro-osmotic drag. More specifically, during the operation of an alkaline electrolyzer, the applied electric field causes the movement of OH^- ions through the separator from cathodes to anodes. It is possible that solvent and thus dissolved gases can be dragged with the ions through the separator and be driven to the opposite side of the cell [62]. Thus, electro-osmotic drag may enhance H_2 crossover and reduce that of O_2 [58]. In literature, there are only a few experimental works that would provide insight into the importance of this mechanism in alkaline electrolysis systems (with Zirfon Perl separators).

Trinke et al [58] report in their research that the influence of electro-osmotic-drag crossover in AWE can be considered low and may be enhanced in high current densities. However, in recent research conducted by Haverkort [23], a behavior opposing the transport of OH^- ions to the anodes was observed. More specifically, for high KOH concentration (5.7 M), it was found that an electro-osmotic flow from anode to cathode dominates over the drag force. This would cause an enhanced O_2 crossover to the cathode side. This project focuses on diffusive and pressure driven convective mechanisms and so electro-osmosis was neglected.

2.4.2. ELECTROLYTE SUPERSATURATION AT THE ELECTRODES

The local supersaturation phenomenon at the electrodes boundary layer is an important parameter for the gas evolution that can also enhance the crossover through the cell separator, especially in the case of zero-gap design, where the electrodes are in contact with the separator [21]. In general, it is reported [19] that the evolving species are firstly composed in dissolved form inside a boundary layer close to the electrodes before the bubble formation. The bubble growth takes place at the nucleation sites on the electrodes, which are surface irregularities and in order to become active, a supersaturation of species in the electrolyte is demanded [58]. The term supersaturation is related to the divergence of the concentration of the dissolved gases (O_2 and H_2) from their saturation state, known as solubility.

The existence of supersaturation at the electrodes boundary layer is a phenomenon studied and experimentally proven in literature [50], [59]. De Jonge et al [17] studied the O_2 and H_2 evolution in a 30% aqueous KOH solution with transparent Nickel coated electrodes. For the O_2 evolution, they examined different current densities and rising operational pressures up to 7.5 bar at 298 K temperature. They reported that O_2 supersaturation increases in higher current densities and pressures. A similar trend was noted for the H_2 supersaturation that was examined only at different current densities with a supersaturation ratio of 100 at 400 $\mathrm{A/m^2}$.

Vogt [61], [60] examined the mass transfer mechanisms at the electrode vicinity trying to find an approach to estimate the supersaturation concentration under the assumption that the concentration at the electrolyte bulk is equal to the solubility. According to his research, there are two relevant mechanisms:

- Mass convection from the electrode to the half-cell bulk.
- Mass transfer of dissolved gases from the supersaturated electrode boundary layer to the growing bubbles that are still attached to the electrode surface.

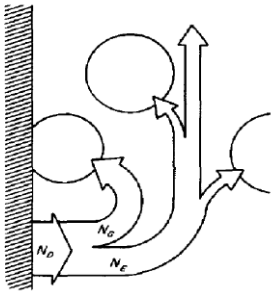

Figure 2.5: Mass transfer mechanisms of dissolved gas from the electrode: N_D refers to the mass flux of a substance D coming out from the electrode and is separated into N_G that goes to the bubble-liquid interface and to N_E that travels to the bulk of the half-cell. [59]

Vogt [61] proposed the following simplified formula to estimate the dissolved gas supersaturation inside the electrode boundary layer:

$$\frac{c_{i,\mathrm{e}}}{c_{i,\mathrm{sat}}} = 1 + \frac{\nu_i \cdot j}{z \cdot F \cdot k_{i,\mathrm{e}} \cdot c_{i,\mathrm{sat}}} \cdot \left(1 - \frac{2}{3} \cdot f_{i,G}\right) \tag{2.18}$$

where $k_{i,\mathrm{e}}$ is the mass transfer coefficient, $c_{i,\mathrm{e}}$ is the supersaturation concentration of gas i at the electrode boundary layer, $c_{i,\mathrm{sat}}$ is the saturation concentration of i at the bulk (under the assumption that the bulk remains saturated) and $f_{i,G}$. is the gas evolution efficiency. According to Vogt [61], two sub-mechanisms have an effect on the aforementioned mass transfer coefficient $k_{i,\mathrm{e}}$: macro-convection due to the electrolyte flow after the electrode and micro-convection due to events happening during the bubble growth and detachment. So, the overall mass transfer coefficient can be calculated by the following formula [61]:

$$k_{i,\mathrm{e}} = \left(k_{i,\mathrm{ec}}^2 + k_{i,\mathrm{eb}}^2\right)^{0.5} \tag{2.19}$$

where $k_{i,\mathrm{ec}}$ and $k_{i,\mathrm{eb}}$ are the macro and micro convection mass transfer coefficients respectively. For the micro-convection coefficient, Vogt [59] conducted experiments with platinum electrodes and estimated values for both O_2 and H_2.

The macro-convection mass transfer coefficient can be estimated using the Sherwood number formula [61]:

$$k_{i,\mathrm{eb}} = \frac{\mathrm{Sh} \cdot D_i}{d_{\mathrm{br}}} = \frac{0.93 \cdot \mathrm{Re}^{0.5} \cdot \mathrm{Sc}^{0.487} \cdot D_i}{d_{\mathrm{br}}} \tag{2.20}$$

where D_i is the gas i diffusion coefficient, d_{br} is the bubble break-off diameter, Re is the Reynolds number, Sc is the Schmidt number and Sh is the Sherwood number. The Reynolds and Schmidt numbers are calculated using the following equations [61]:

$$\mathrm{Re} = \frac{\nu_i \cdot j \cdot R_g \cdot T \cdot f_{i,G} \cdot d_{\mathrm{br}}}{z \cdot F \cdot P \cdot \nu_L} \tag{2.21}$$

$$\mathrm{Sc} = \frac{\nu_L}{D_i} \tag{2.22}$$

where ν_i is the stoichiometric coefficient of i, j is the current density, R_g is the gas constant, T is the electrolyte temperature, P is the operating pressure, ν_L the electrolyte kinematic viscosity, z is the number of transferred electrons and F is the Faraday constant. The bubble break-off diameter refers to the diameter of a single bubble when it is detached from the electrode. Several empirical correlations have been proposed after conducting experiments and the general finding is that the bubble break-off diameter is larger in low current densities [22]. However, other researchers made the opposite observation [22], which means that a completely accurate formula is difficult to be formed as the bubble break-off diameter depends also on other operating conditions such as the electrode material and the type of electrolyte [48].

The gas evolution efficiency is another parameter that is estimated experimentally. In literature, there are only a few available correlations and mainly for the case of hydrogen evolution. Haug et al [22] proposed the following equation after elaborating experimental data from various researchers for H_2 evolution in KOH electrolyte with Nickel electrodes:

$$f_{H_2,G} = 0.25744 \cdot j^{0.14134} \tag{2.23}$$

The authors argue that the above expression is in agreement with other experimental works with similar operating conditions and the resulting efficiencies are below unity for

the typical industrial current density operating window (1000-4000 $A \cdot m^{-2}$) [16]. For oxygen evolution efficiency, no available data were found in the literature.

In the zero-gap design, the fact that the cell separator is in contact with the supersaturated electrode inserts an additional mass transfer mechanism related to the crossover to the opposite half-cell compartment, which was not taken into account in Vogt's approach and so it was not used in this study. The local supersaturation at the separator boundary was used as a crossover enhancing parameter in the sensitivity analysis.

2.4.3. GAS CROSSOVER THROUGH ELECTROLYTE MIXING

As mentioned before, dissolved gases can crossover due to the electrolyte mixing cycles through the pipe that connects the cathodic and anodic compartments of an alkaline electrolyzer. According to Trinke [58], this is the mechanism that has the largest contribution to the overall gas crossover. Thus, by knowing the velocity profile of the electrolyte flowing inside the piping system, it is possible to predict the transient mass transport of dissolved components and evaluate their concentration at the opposite side. As in the case of the separator crossover, the physical mechanisms that affect the mass transport inside the pipes are advection due to electrolyte flow and diffusion because of local concentration differences. Consequently, the dissolved gases transport through the piping system can be evaluated by solving the transient 1-d advection-diffusion equation:

$$\frac{\partial c_i}{\partial t} + u_{\text{pipe}} \cdot \frac{\partial c_i}{\partial x} = D_i \cdot \frac{\partial^2 c_i}{\partial x^2} \tag{2.24}$$

However, the shear flow of electrolyte inside the pipes can enhance the effective diffusivity of the transported components under a certain condition. This phenomenon is called Taylor dispersion and was initially studied by Taylor for both laminar [53] and turbulent [54] flow regimes. More specifically, Taylor examined how the advection and diffusion mechanisms affect the transport of a soluble component inside a circular tube, moving with the mean flow velocity under laminar Poiseuille flow conditions [53]. In Poiseuille flow, the axial velocity follows a parabolic profile with its maximum value at the center of the tube, while the mean velocity is equal to the half value of the maximum velocity [37]. When mass advection in the axial direction dominates (high Pe number), the axial molecular diffusion can be neglected. However, radial diffusion may have a considerable effect on the average mass transport.

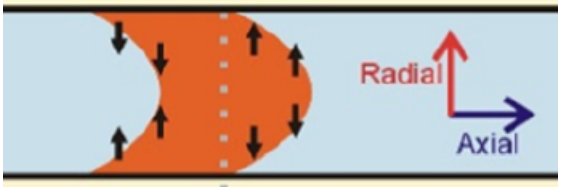

Figure 2.6: Poiseuille flow in a circular tube showing the different dispersion of a soluble component at the front and the back side of a pulse. [8]

Figure 2.6 depicts how the soluble component mass transport is affected by the flow conditions under the Taylor dispersion regime and laminar flow. As can be noticed, at the head of the pulse, the concentration is greater in the center of the tube compared to the walls, so the effect of radial diffusion (with direction to the tube walls) is slowing down the axial mean speed of mass transport. At the rear side of the pulse, the opposite phenomenon

happens, as the concentration is higher near the walls and radial diffusion (with direction towards the pipe center) contributes to increasing mass transport axial mean velocity.

Consequently, Taylor derived a virtual diffusion coefficient in order to describe the aforementioned effects. This coefficient is used in a purely 1-d diffusion equation as [53]:

$$\frac{\partial c_i}{\partial t} + u_{\text{pipe}} \cdot \frac{\partial c_i}{\partial x} = D_{\text{Taylor},i} \cdot \frac{\partial^2 c_i}{\partial x^2} \tag{2.25}$$

where $D_{\text{Taylor},i}$ is the Taylor virtual diffusion coefficient and for laminar flow is calculated as [53]:

$$D_{\text{Taylor},i} = \frac{r_{\text{pipe}}^2 \cdot u_{\text{pipe}}^2}{48 \cdot D_i} \tag{2.26}$$

where u_{pipe} and r_{pipe} are the pipe's mean velocity and radius, while D_i is the diffusion coefficient of the examined component. For turbulent flow, Taylor followed similar derivation and proposed the below formula [54]:

$$D_{\text{Taylor},i} = 10.1 \cdot r_{\text{pipe}} \cdot u_* \tag{2.27}$$

where u_* is the shear or friction velocity and is defined as a function of the shear stress and density [54]:

$$u_* = \sqrt{\frac{\tau_w}{\rho}} \tag{2.28}$$

Equation 2.27 is also written in a different way as:

$$D_{\text{Taylor},i} = 10.1 \cdot r_{\text{pipe}} \cdot u_{\text{pipe}} \cdot \left(\frac{u_*}{u_{\text{pipe}}} \right) \tag{2.29}$$

where the ratio of the shear over the mean flow velocity can be found as a function of Reynolds number in [54].

Taylor dispersion equation 2.25 is valid when the following condition is satisfied [53]:

$$\frac{L_{\text{pipe}}}{u_{\text{pipe}}} \gg \frac{r_{\text{pipe}}^2}{3.8^2 \cdot D_i} \tag{2.30}$$

2.5. PREVIOUS WORK ON CROSSOVERS AND TRANSIENT MODELING

In literature, various studies have been published regarding the operation of AWE and are mainly based on analysis related to electrochemistry and thermodynamics. In the field of gas crossovers, only a few works were found and focus on models predicting the gas purities on a steady time regime.

Haug et al [22] developed a zero-dimension model that can predict the crossover in an atmospheric pressure single cell under different operational conditions and electrolyte cycling strategies. More specifically, the two compartments of the cell (anode and cathode) were modeled as CSTR (typical in chemical engineering) with the possibility of mass exchange through the cell's separator. The authors took also into account the mass transfer between the evolving bubbles and the liquid saturated electrolyte. Their main finding regarding the operational parameters is that the gas crossover is higher in low current densities, while it tends to reduce in higher operational temperatures. Regarding the electrolyte management, a cycle mixing strategy presents higher H_2 impurity in the O_2 flash tank contrary to separated electrolyte cycles and this difference is considerably higher in low current densities.

In another work, Schalenbach et al [46] examined the effect of the pressure difference between the opposite cell compartments on the H_2 crossover through the separator for AWE operating at 80 ^{o}C and 6 bar absolute pressure for different separator types. They concluded that with a 1% absolute pressure difference, the convection mass transfer mechanism through the separator becomes dominant over the diffusion. They also found a similar trend regarding the higher level of crossover in low current densities.

In the field of control and dynamic transient modeling of AWE systems, a gap in the literature is identified, since extended relevant research was not found. In recent work, David et al [15] developed and experimentally validated a semi-physical dynamic transient model for the case of a self pressurized electrolyzer operating at high pressures (tested up to 70 bar) and its pressure control system. Based on mass and energy conservation laws for the various modules, the model predicts fluctuations of pressure and electrolyte level at the gas separators caused by the evolving gases and purging valve operation, while giving an insight on the dissolved gas concentration throughout the system. Regarding the crossovers, the main finding was that H_2 impurity inside the O_2 flash separator reached 2% at 70 bar, a value that is enhanced contrary to lower operating pressures. This model also does not take into account the inertia dominated oscillating behavior of the electrolyte that can be caused by the valve opening.

3

ZEF ELECTROLYSIS SYSTEM

3.1. PROCESS OVERVIEW

ZEF develops a self-pressurized electrolysis system with natural electrolyte recirculation. This means that the pressure is built up by the continuous gas production into the stack and controlled with the use of purging valves, while the electrolyte is flowing under natural convection effects without the implementation of a pump. The lack of a pump reduces the energy needs of the system and saves space for the micro-plant. Currently, the company develops an experimental setup to test the system's aspects and behavior under the influence of the real operating conditions and process control. This experimental setup, that ZEF has named 'bunker twin' is modeled in this project. Figure 3.1 presents a schematic of the electrolysis process in the 'bunker twin'.

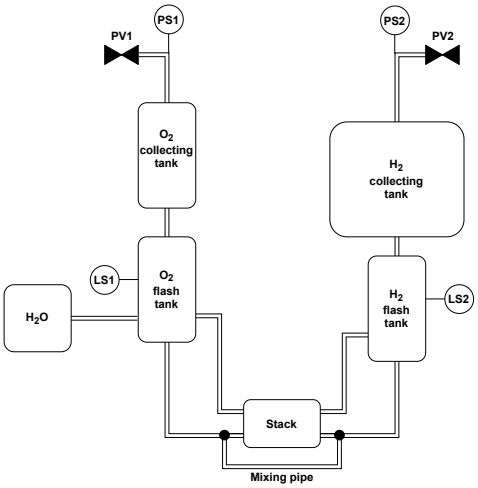

Figure 3.1: ZEF bunker twin schematic including the stack, flash tanks, buffers, two electrolyte level sensors (LS1 & LS2), two pressure sensors (PS1 & PS2) and two gas purging valves (PV1 & PV2).

The core of the system is an 18-cell stack, where O_2 and H_2 are produced at the anodes and cathodes respectively. The evolving gases in the form of bubbles are driven to the flash

tanks, under the effect of buoyancy force, where are separated from the liquid electrolyte. For the scope of this report, the oxygen side will be referred to as the 'left side' and the hydrogen side as the 'right side'. After the flash separation, the gases are collected in cylindrical tanks, named buffers. H_2 is collected in the right side buffer, which is designed larger due to the different gas production rates with analogy H_2:O_2 = 2:1 (eq. 2.3 and 2.2).

The different electrochemical reactions that take place at the cells of the stack are causing divergence in the local electrolyte concentration, as water is produced at the anodes with a double quantity consumed at the cathodes. To maintain a balance of the concentration, the two sides are communicating and mixing through a pipe below the stack as presented in Figure 3.1. The consumed water quantity is replenished with compressed water pumped in the O_2 flash tank.

3.2. CONTROL SYSTEM DESCRIPTION

The process control system includes two electrolyte level sensors in the flash tanks (LS1 and LS2), two gas pressure sensors (PS1 and PS2) and two solenoid gas purging valves (PV1 and PV2). ZEF has adopted a strategy to control the system pressure by maintaining the electrolyte level in the flash tanks and continuously monitoring the accumulated gases pressure in the buffers. To achieve the electrolyte level control in O_2 flash tank, the buffer is designed smaller leading to faster pressure increase at the left side, despite the lower gas production rate and thus electrolyte moves to the right side. The valves open for fixed time intervals during the system's operation puffing out gas according to the signals from the sensors and can operate simultaneously. The level sensor at the left side (LS1) ensures that the electrolyte level will remain continuously above a fixed level. When the liquid level drops below the sensor, a signal triggers the O_2 purging valve (PV1), gas is released to the environment and thus, the pressure drop in the O_2 buffer forces the electrolyte to move backward. This sub-controlling system is active for the whole operating window of the electrolyzer. The aforementioned procedure is visually described in the following set of figures.

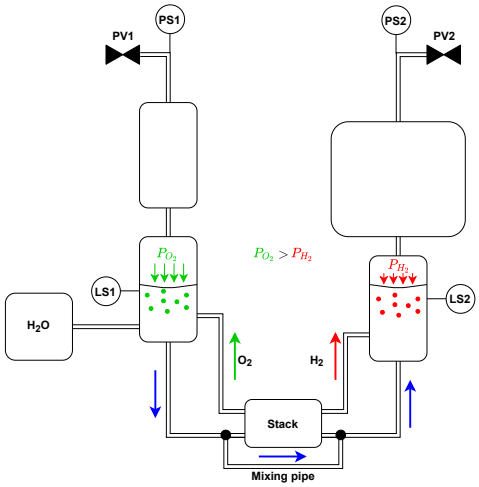

Figure 3.2: Purging valves closed, both level sensors wet, continuous gas production causes electrolyte movement from left side to right side, O_2 flash tank electrolyte level starts decreasing.

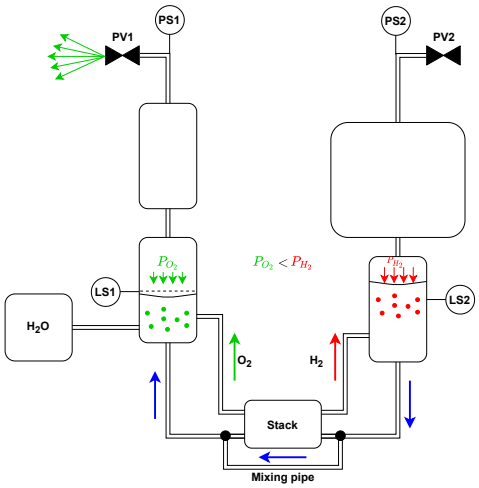

Figure 3.3: Left side level sensor (LS1) becomes dry, O_2 purging valve (PV1) opens and releases gas to the environment, liquid electrolyte follows backward direction moving from right to left side, O_2 flash tank electrolyte level starts rising.

On the opposite side, the control system behaves differently. The operation of O_2 flash tank level sensor (LS1) ensures that electrolyte will be present on both sides. Water consumption at the cathodes will gradually reduce the total water amount in the system. When the electrolyte level in the right side falls below the level sensor LS2, a signal informs the control system to add water inside the O_2 flash tank. As for the purging valve (PV2), it is triggered every time the gas pressure inside H_2 buffer (PS2) reaches the control point, which is the system's final operating pressure (50 bar).

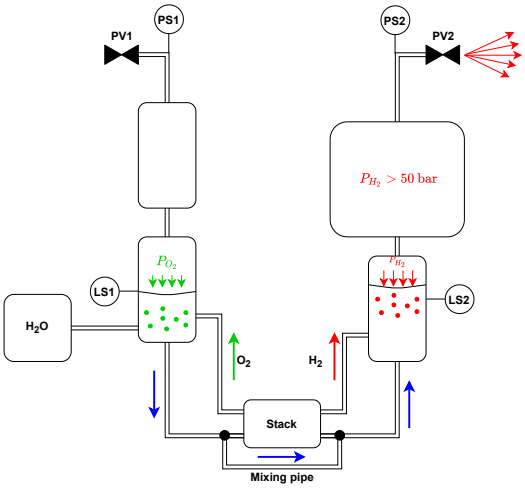

Figure 3.4: Pressure in H_2 buffer exceeds 50 bar, purging valve PV2 opens, liquid moving faster to the right side.

To sum up, with the described system, ZEF achieves to effectively control both electrolyte level in the flash tanks and gas pressure in the buffers. The role of purging valves

is important as their operation affects the dynamic behavior of the whole system since the liquid electrolyte is moving back and forth inside the piping, stack and flash tanks, presenting an oscillatory behavior. This effect is interesting especially after the system reaches its final control pressure of 50 bar when both purging valves can operate simultaneously resulting in increased momentum of the moving liquid and probably higher pressure gradients between the two sides.

3.3. GEOMETRIC CHARACTERISTICS

The following tables include data regarding the geometry of the various electrolysis system parts that are used in modelling and some parameters of the control system:

Table 3.1: Dimensions of flash tanks and buffers.

O_2 flash tank		
Diameter	34.8	mm
Length	105	mm
O_2 buffer		
Diameter	34.8	mm
Length	105	mm
Total O_2 side volume	$2.018 \cdot 10^{-4}$	m^3
H_2 flash tank		
Diameter	34.8	mm
Length	137	mm
H_2 buffer		
Diameter	72.9	mm
Length	105.5	mm
Total H_2 side volume	$5.707 \cdot 10^{-4}$	m^3

Table 3.1 includes the dimensions of the flash tanks and buffers. The total volume of the H_2 side is around 2.8 times larger than the O_2 side.

Table 3.2: Electrolysis cells data.

Half-cell width	4	mm
Electrode thickness	0.5	mm
Separator thickness	0.5	mm
Bipolar plate thickness	0.5	mm
Net cross area	63.36	cm^2
Number of cells	18	-
Total stack length	144	mm

Table 3.2 summarizes geometrical data for the cells. Each half-cell (anode or cathode) is 4 mm thick including the electrode and the half separator, which is compressed between the two half-cells. The adjoining cells are separated by bipolar plates, which prevent the mixing of gases as described in chapter 2. The total length of the stack includes also 2 steel end-plates that are used to compress the cells and keep them in their position.

Table 3.3: Purging valves and sensors data.

Purging valves opening duration		
O2 valve (PV1)	100	ms
H2 valve (PV2)	100	ms
Level sensor height position		
O2 tank (LS1)	59	mm
H2 tank (LS2)	59	mm

The level sensors height position is measured from the bottom of the flash tanks. Moreover, the hydraulic factor of both purging valves is 0.017 $Nm^3 \cdot h^{-1}$. Geometrical data and a more detailed schematic about the piping system are included in chapter 4.

4

MODELING

4.1. INTRODUCTION

For the scope of this thesis, the modeling procedure was divided into two main models. The first one predicts the transient dynamic response of the ZEF electrolysis system. More specifically, having the gas production as input, the model simulates the electrolyte flow in the pipe network and predicts how it is affected by the pressure build-up and purging valves opening during the two operating states. State 1 is the startup period when the system's pressure increases until it reaches the main operating point of 50 bar. As described in chapter 3, during state 1, only O_2 purging valve is working to maintain a balance in electrolyte level. State 2 is the main operating window of the system when both purging valves are working to control the electrolyte level and system's pressure. The second model predicts the dissolved gas flow in the system. Using the results of the first model (liquid electrolyte velocity in the pipes and pressure in relevant points of the system), transient mass transport equations were solved by applying numerical schemes and coupling the different elements with appropriate interface conditions. The main scope of the second model is to estimate the level of cross-contamination in the flash tanks.

4.2. ELECTROLYSIS SYSTEM DYNAMIC RESPONSE MODEL

4.2.1. GENERAL INFORMATION AND NETWORK SCHEMATIC

The development of this model is based on a 1-d unsteady pipe network analysis, where the system is split into nodes and elements [49]. Pipes and tanks are considered as elements, while their linking points are treated as nodes. To characterize the flow and estimate velocities and pressures, a mathematical model was developed by applying mass and momentum conservation at the elements and continuity principle at the nodes. The bubbles are entering continuously the flash tanks where the accumulated gas pressure acts as an external force on the liquid electrolyte that contributes to its movement into the network (a list of all the assumptions is be presented in the next pages). The following figure and tables present in detail the hydraulic network structure and its geometrical data.

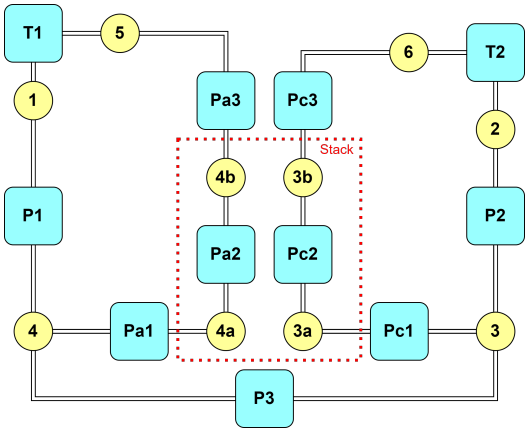

Figure 4.1: Hydraulic network with elements (blue squares) and nodes (yellow circles). Elements Pa2 and Pc2 represent the stack anodes and cathodes respectively. To reduce the model complexity, the half-cell compartments were treated as two single pipes assuming that the flow through all the anodes and cathodes respectively is identical.

Table 4.1: Pipe length and diameter.

Element	Length (m)	Diameter (mm)
P1	0.46	4
P2	0.31	4
P3	0.24	4
Pa1 & Pc1	0.172	4
Pa2 & Pc2	0.07	6.5
Pa3	0.462	4
Pc3	0.312	4

Table 4.2: Nodes height.

Node	Height (m)
1	0.193
2	0.163
3 & 4	0.07
3a & 4a	0.07
3b & 4b	0.152
5	0.243
6	0.213

For the nodal height, the reference point with zero height was set to be the centerline of element P3. Also, the height difference of the two flash tanks is 3 cm (difference between node 1 and 2).

4.2.2. MODEL ASSUMPTIONS

The following assumptions are made for the mathematical model derivation:

- The supplied current density is assumed to be steady without fluctuations.
- Electrolyte flow in the pipes is assumed to be incompressible.
- The operating temperature is assumed to be steady and equal to 90 ^{o}C (ZEF specification).
- Water production/consumption at the anodes/cathodes respectively is neglected and assumed that it is continuously replenished.
- The flow through half-cells (i.e. anodes) is assumed to be identical. For simplification of the hydraulic network, the stack is modeled as a simple tube with a hydraulic diameter (Pa2 and Pc2 for anodes/cathodes in Figure 4.1).
- A two-phase flow approach is not considered. The flow is assumed to be governed by the pressure difference between the flash tanks.
- A quasi-steady approach is followed for the determination of the pipe friction coefficient.
- The liquid electrolyte pressure at the bottom of the flash tanks (where they are connected to pipe P1 and P2) and at the height where pipes Pa3 & Pc3 enter the flash tanks, is assumed to be equal to the hydrostatic pressure plus the accumulated gas pressure above the liquid electrolyte, neglecting the dynamic term.
- The possible electrolyte flow between the half-cell compartments due to differential pressure over the separators is not taken into account to reduce the model complexity.
- The extra gas fraction in the flash tanks/buffers caused by the crossovers was not considered in this model.

4.2.3. MATHEMATICAL MODEL

For consistency in the model derivation, the electrolyte flow direction is assumed to be positive from the right to the left side regarding pipes P1, P2 and P3. For the rest system, flow is considered positive when it is driven towards the flash tanks. This accordance, is illustrated in the following figure.

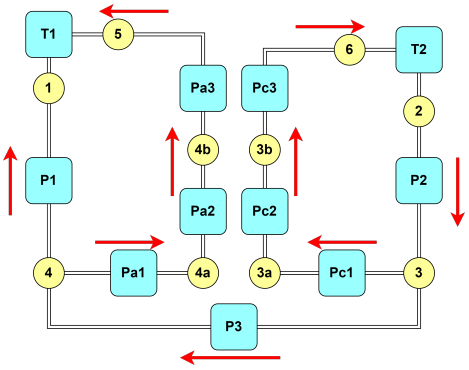

Figure 4.2: Positive direction of electrolyte flow.

As mentioned before, the model consists of transient mass and momentum balances at the various elements of the system. Under the incompressibility assumption, all the fluid inside an element is moving with the same velocity that changes with time and not spatially. The equations set is similar for the pipes. For the case of the flash tanks, where the total liquid volume changes, a special deforming control volume is selected.

EQUATIONS FOR THE PIPES:

A general unsteady 1-d momentum equation for incompressible flow in a pipe with length L and cross section A is given below [7]:

$$\rho \cdot A_{\mathrm{p}} \cdot L_{\mathrm{p}} \cdot \frac{\partial u_{\mathrm{p}}}{\partial t} = \left(P_{\mathrm{in}} - P_{\mathrm{out}}\right) \cdot A_{\mathrm{p}} + \rho \cdot g \cdot A_{\mathrm{p}} \cdot \left(h_{\mathrm{in}} - h_{\mathrm{out}}\right) - F_{\mathrm{friction}} \tag{4.1}$$

The above momentum conservation is an expression of Newton's second law and describes the rate of change of the linear momentum due to the acting forces. The LHS represents the aforementioned momentum change and is equal to the product of the total liquid mass times the flow acceleration. The RHS includes the aggregation of the acting forces. The first term is the force owing to the pressure gradient between the pipe ends, the second term is the gravity force contribution, while the third term is the friction force. In the previous equation, $h_{\mathrm{in}} - h_{\mathrm{out}}$ is the height difference between the pipe inlet and outlet.

EQUATIONS FOR THE FLASH TANKS LIQUID PART:

The model equations for the case of the flash tanks are different since the liquid volume changes with time. For this reason, a deforming control volume that includes the liquid electrolyte is used to derive the transient mass and momentum balances. The following figure depicts the used control volumes for both flash tanks. For the analytical derivation of the following equations, refer to appendix A.1.

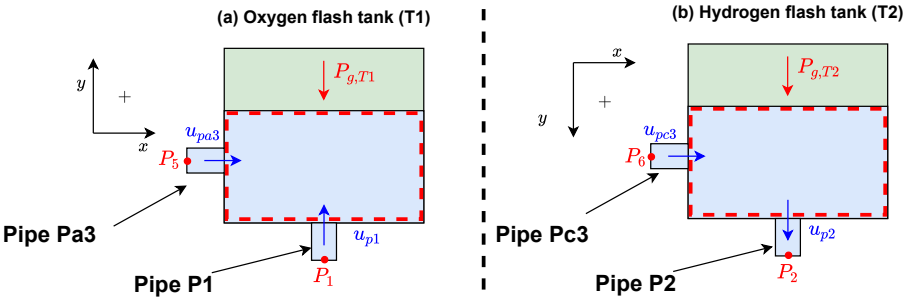

Figure 4.3: Selected control volumes (red dashed lines) for both flash tanks.

The positive flow direction is adapted to be in agreement with figure 4.3. The selected control volumes can deform at the y direction following the liquid electrolyte movement. The pressure at top liquid surface is equal to the accumulated gas pressure and at the pipe connections has the value of the corresponding nodes. The transient mass conservation equation for the deforming control volume reads:

$$\rho \cdot A_{\mathrm{t}} \cdot \dot{y}_{\mathrm{t}} = A_{\mathrm{p}} \cdot \left[\sum \left(\rho \cdot u_{\mathrm{p,in}}\right) - \sum \left(\rho \cdot u_{\mathrm{p,out}}\right)\right] \tag{4.2}$$

where A_{t} is the tank cross section area and $\dot{y}_{\mathrm{t}}$ is the liquid velocity inside the tank (rate of control volume deformation). The LHS represents the mass accumulation of the liquid

electrolyte inside the flash tank, while the RHS includes the mass amount that enters and exits the control volume. By differentiating the above equation, a similar expression for the acceleration can be derived. The momentum conservation equation is split into two separate equations for the corresponding directions. The y axis equation has the following form:

$$\rho \cdot A_t \cdot y_t \cdot \ddot{y}_t + \rho \cdot A_t \cdot \dot{y}_t^2 + i \cdot \rho \cdot A_p \cdot u_p^2 = i \cdot (P_g - P_n) \cdot A_p + i \cdot \rho \cdot g \cdot y_t \cdot A_p - F_{friction} \tag{4.3}$$

where i is -1 for oxygen flash tank (T1) and 1 for hydrogen flash tank (T2), $\ddot{y}_t$ is the liquid acceleration, y_t is the liquid height, P_g is the gas pressure above the control volume, P_n is the pressure of the node below the flash tank (n=1 for tank T1 and n=2 for tank T2), u_p is the flow velocity of the pipe below the tank (P1 for T1 and P2 for T2 in fig. 4.3) and $F_{friction}$ is the linear friction force (estimated using equation 4.12, as in the case of the pipes). The x axis equation reads as:

$$0 = \rho \cdot u_p^2 \cdot A_p + (P_n - P_g) \cdot A_p - \rho \cdot g \cdot (y_t - y_p) \cdot A_p \tag{4.4}$$

where u_p refers to flow velocity of the pipe connected on the lateral surface of the cylindrical tank (Pa3 for T1 and Pc3 for T2 in fig. 4.3), P_n is the pressure of node 5 for T1 and node 6 for T2, while y_p is the distance of Pa3 and Pc3 from the bottom of the flash tanks.

EQUATIONS FOR THE FLASH TANKS GASEOUS PART:

The gaseous phase (flash tanks + buffers) pressure is a parameter that affects the system's behavior since the electrolyzer is self-pressurized. As stated in the assumptions list, the evolving gases continuously enter the gas phase of the flash tanks with a molar flow rate that is estimated using Faraday law (eq. 2.7 for O_2 and eq. 2.8 for H_2). Consequently, a transient material balance for the gas phase is derived to estimate the mass of the accumulated components and the pressure is calculated using a real gases law.

$$\frac{\partial(\rho_g \cdot V_g)}{\partial t} = \dot{m}_{g,in} - \rho_g \cdot \dot{Q}_{valve} \tag{4.5}$$

$$V_g = V_t - A_t \cdot y_t \tag{4.6}$$

where ρ_g is the density of the accumulated gas, V_g is the gas phase volume, V_t is the total volume, $\dot{m}_{g,in}$ is mass flow rate of the produced gas and $\dot{Q}_{valve}$ is the volumetric flow rate that exits the system when a valve is in operation. ZEF is using solenoid valves that operate in a way described in chapter 3. For this model, the gas volumetric flow rate through the valves is calculated using the below formulas (in $m^3 \cdot h^{-1}$) [2]:

$$P_{out} \geq \frac{P_g}{2} \rightarrow \dot{Q}_{valve} = 514 \cdot k_v \cdot \sqrt{\frac{\Delta P \cdot P_{out}}{SG \cdot T}} \cdot \frac{P_{ref}}{P_g} \cdot \frac{T}{T_{ref}} \tag{4.7}$$

$$P_{out} < \frac{P_g}{2} \rightarrow \dot{Q}_{valve} = \frac{257 \cdot P_g \cdot k_v}{\sqrt{SG \cdot T}} \cdot \frac{P_{ref}}{P_g} \cdot \frac{T}{T_{ref}} \tag{4.8}$$

where P_g (in bar) is the gas pressure inside the flash tanks, P_{out} (in bar) is the discharge pressure (environmental pressure), k_v (in $Nm^3 \cdot h^{-1}$) is the valve flow coefficient, SG is the specific gravity of the gas that passes through the valve and T is the operating temperature. The valve flow coefficient is a characteristic parameter that is given in normal conditions (20 ^oC and 1 bar) and expresses the volumetric flow rate when the pressure drop through the valve is 1 bar. Both of the aforementioned equations are multiplied by a term to convert normal to actual conditions. Moreover, the above equations are used by many

valve manufacturers for sizing purposes. In equation 4.8, the resulting volumetric flow rate depends only on the upstream pressure and when converted to actual conditions, it is steady. This is the choking phenomenon meaning the limiting point when the flow rate through the valve is steady and does not depend on pressure drop variations. This limiting point is also called critical point. In equations 4.7 & 4.8, it is assumed that the critical point is 50% of the upstream pressure (gas pressure in the flash tanks). Thus, when the downstream pressure (environmental) is lower than the critical pressure ($0.5 \cdot P_g$), then the flow is supercritical (choked) and equation 4.8 holds.

MASS CONSERVATION AT TEE SECTIONS AND ELEMENT CONNECTIONS:

As can be seen in figure 4.1, the hydraulic network includes two tee sections (nodes 3 and 4) where the flow may present splitting or mixing behavior. The application of continuity principle at these nodes results:

$$\sum (\rho \cdot u_{p,in} \cdot A_p) = \sum (\rho \cdot u_{p,out} \cdot A_p) \tag{4.9}$$

A similar equation is used for the acceleration by differentiating the above continuity formula.

FRICTION FORCE:

In hydraulic networks analysis, the friction force that opposes the flow direction is a result of linear or major and local or minor contributions. The linear part accounts for the viscosity and pipe roughness effect if the element (pipe) is straight, while the minor part includes 'barriers' of the flow such as sudden expansions or contractions, bends, elbows and tee sections [30].

Linear friction contribution:

The linear friction force is the product of the pipe wall shear stress times the internal wetted area:

$$F_{linear,friction} = \tau_w \cdot \pi \cdot d_p \cdot L_p \tag{4.10}$$

The shear stress is related to the widely used Darcy-Weisbach friction factor λ_D using the following correlation [13]:

$$\tau_w = \frac{\lambda_D \cdot \rho \cdot u_p^2}{8} \tag{4.11}$$

After some numerical manipulations, the linear friction force of the pipe flow takes the following form as a function of the Darcy coefficient λ_D:

$$F_{linear,friction} = \lambda_D \cdot \frac{\rho \cdot L_p \cdot A_p}{2 \cdot d_p} \cdot u_p \cdot |u_p| \tag{4.12}$$

where the flow velocity is written in a way to ensure that friction force has always the correct sign.

For the Darcy friction factor, several empirical correlations have been proposed for laminar and turbulent flow regimes. For this model, Churchill equation [13] is implemented, since it provides satisfactory results for both regimes.

$$\lambda_D = 8 \cdot \left[\left(\frac{8}{Re} \right)^{12} + \frac{1}{(A+B)^{1.5}} \right]^{\frac{1}{12}} \tag{4.13}$$

$$A = \left\{ 2.457 \cdot \ln \left[\frac{1}{\left(\frac{7}{\mathrm{Re}}\right)^{0.9} + 0.27 \cdot \frac{\varepsilon_{ro}}{d_\mathrm{p}}} \right] \right\}^{16} \tag{4.14}$$

$$B = \left(\frac{37530}{\mathrm{Re}} \right)^{16} \tag{4.15}$$

$$\mathrm{Re} = \frac{\rho \cdot |u_\mathrm{p}| \cdot d_\mathrm{p}}{\mu} \tag{4.16}$$

where ε_{ro} is the pipe roughness.

The aforementioned Darcy friction factor is based on analysis derived for steady-state pipe flow. For transient problems, most of the work found in literature is based on studies related to water hammer theory, which incorporates transient oscillating flow phenomena. An example of a widely used 1-d transient friction model is the one developed by Brunone [38], which takes into account the instantaneous local acceleration of the flow and 'corrects' the steady Darcy friction factor by adding a virtual unsteady contribution. Bergant et al [9] performed experiments with a fast valve closure and compared several models. Brunone's model had the best fit to the experimental data for both laminar and turbulent flow experiments, while the 'quasi-steady' approach by using only the Darcy friction factor provided satisfactory results at the beginning (highest amplitude of oscillations) but presented less damping in 1 s timescale. For the scope of this thesis, the implementation of the unsteady friction term is neglected since it increased dramatically the computational time and caused random crashes during the model execution due to numerical issues. Consequently, an underestimation of damping effects after the valve opening is expected.

Local friction contribution:

The local friction force contribution is estimated using the following equation:

$$F_\mathrm{local,friction} = \lambda_L \cdot \frac{\rho \cdot A_\mathrm{p}}{2} \cdot u_\mathrm{p} \cdot |u_\mathrm{p}| \tag{4.17}$$

where λ_L is the local friction loss coefficient. This coefficient is 0.5 for pipe contraction, 1 for expansion, 0.3 for 90^o pipe bend and 1 for branched flow in tee section [30].

4.2.4. USED SOFTWARE

Based on the previous derivation, a set of equations is built for the hydraulic network with variables that change over time, creating an algebraic loop that needs to be solved iteratively. The total set of equations is included in appendix A.2. The mathematical model was implemented and solved using Simulink.

Simulink is a graphical environment appropriate for designing, modeling and simulating dynamic systems. It includes libraries with predefined blocks for modeling of both discrete and continuous-time states. The designed transient hydraulic circuit is a continuous system, meaning that its variables are changing continuously over time. Moreover, the rapid variations of the model parameters (pressures, velocities, flash tanks liquid height) caused by the operation of the valves, make the problem stiff. Simulink offers both fixed and variable time step intervals options. The fixed-step solvers are using the same time step defined by the user before the simulation execution. For a stiff system, the fixed time step should be set very small to be able to predict a stable solution when the dynamics change rapidly, with a cost for the computational time. On the other hand, variable step solvers can alter the time step during simulation, by reducing it when the dynamics change fast

to improve accuracy and increasing it in slower states, saving computational time. The user can modify the time step margins (minimum and maximum values) and also define the relative and absolute error tolerance.

Regarding the model solution at each time step, an iterative procedure is demanded. Simulink includes algebraic loop algorithms that detect automatically the variables that affect the loop, depending on how the model blocks are defined by the user. Based on these variables, the solver applies iterations concerning the defined global error tolerance till it converges to the solution and moves to the following time step. More information about the program and the used solvers is provided in appendix A.3.

4.3. CROSSOVERS MODEL

4.3.1. GENERAL INFORMATION

Having characterized the dynamic response of the electrolysis system under the effect of pressure build-up and control valves opening, a second model was developed to quantify the level of gas crossover on both flash tanks. This was achieved by solving transient 1d mass transport equations, using the predicted velocities and pressures from the previous model as inputs and coupling the different hydraulic network elements with appropriate interface conditions.

As described in chapter 2, dissolved gases can pass to the opposite side through the cells separators and the mixing electrolyte cycles. To calculate the transport of the dissolved components through the various network elements, the transient advection-diffusion equation (eq. 2.24) was solved numerically by applying the Finite Difference Method (FDM). The flash tanks, half-cell compartments and pipes leading the bubbles to the flash tanks were treated as Continuously Stirred Tank Reactors (CSTR), where the accumulated species are perfectly mixed with the same concentration in the whole liquid volume [31]. A simplified scheme illustrating the system with the two CSTR is included in the following figure:

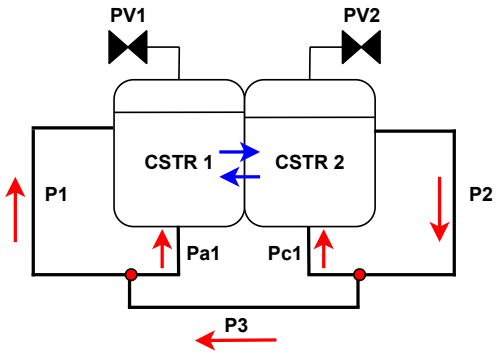

Figure 4.4: The presented scheme is similar to the hydraulic network in fig 4.1 with the difference that the CSTR 1 includes T1, Pa2 and Pa3, while CSTR 2 includes T2, Pc2 and Pc3. The red arrows show the positive direction of the flow and the blue ones indicate the mass transfer between the two CSTR due to advection & diffusion through separators of the cells.

4.3.2. MODEL ASSUMPTIONS

The following assumptions are made for the crossovers model (the mentioned element names refer to figures 4.1 and 4.4):

- The operating temperature is steady and equal to 90 ^{o}C.

- As mentioned before, the half-cells, flash tanks (T1 & T2) and pipes carrying the bubbles to the flash tanks (Pa3 & Pc3) are treated as CSTR. This means i.e. for the O_2 side that the concentration of O_2 or H_2 at these elements has the same value.
- The bubbles are assumed to have a large surface area absorbing any extra quantity that is transferred from the supersaturated electrodes boundary layer to the electrolyte bulk. Consequently, the concentration of O_2 at the O_2 side and H_2 at the H_2 side is assumed to be equal to their solubility and is affected only by the change of gas pressure.
- Ideal mixing is assumed at the nodes representing the pipe tee branches (nodes 3 & 4).
- The gas phase pressure in the relevant elements is assumed to be equal to the gas phase pressure in the flash tanks.
- Only dissolved components are taken into account for the crossover through the separators of the cells. It is reported in the literature that the Zirfon Perl material is impermeable to bubbles [45].
- The absolute cell-pressure is assumed to be the average pressure of the nodes representing the inlet and outlet of the cell (nodes 4a & 4b for anodes and 3a & 3b for cathodes in figure 4.1). This pressure is used to estimate the advective crossover velocity through the separators.
- Henry's equilibrium law is assumed for the gas-liquid phase in the CSTR elements.
- Numerical schemes are set and solved for the elements carrying the liquid electrolyte to the stack (P1 & Pa1 for O_2 side and P2 & Pc1 for H_2 side), the element connecting the two sides (P3) and the separators of the cells.

4.3.3. NUMERICAL SCHEMES

For the discretization of the transient 1d advection-diffusion equation (eq. 2.24), an implicit approach was followed. Every element of the hydraulic network that was solved numerically, was split spatially into several nodes. For better consistency in the following description, the subscript j will refer to the examined node, while the upper script t will refer to the examined time.

Using Taylor series expansion, the concentration time derivative term was discretized with a first order forward difference formula, the advection term with a first order backward difference formula (or forward taking into consideration the flow direction) and the diffusion term with a second order centered difference formula [33]. The combination of the used time and spatial advection terms discretization is known as the first order upwind scheme.

$$\text{if } u^{t+1} > 0 \rightarrow \frac{c_j^{t+1} - c_j^t}{\Delta t} + u^{t+1} \cdot \frac{c_j^{t+1} - c_{j-1}^{t+1}}{\Delta x} = D \cdot \frac{c_{j+1}^{t+1} - 2 \cdot c_j^{t+1} + c_{j-1}^{t+1}}{\Delta x^2} \tag{4.18}$$

$$\text{if } u^{t+1} < 0 \rightarrow \frac{c_j^{t+1} - c_j^t}{\Delta t} + u^{t+1} \cdot \frac{c_{j+1}^{t+1} - c_j^{t+1}}{\Delta x} = D \cdot \frac{c_{j+1}^{t+1} - 2 \cdot c_j^{t+1} + c_{j-1}^{t+1}}{\Delta x^2} \tag{4.19}$$

If the above equations are used for the pipe elements, the velocity u was the one implemented from the hydraulic network model results and the diffusivity D was H_2 or O_2

property in 30% aqueous KOH solution and 90 ^{o}C. If the equations solve the advection-diffusion through the cell separator, the used velocity was calculated from Darcy equation 2.15, while the effective diffusivity of H_2 or O_2 was estimated using equation 2.11.

The reason for the selection of an implicit numerical approach is its unconditional stability. The results from the hydraulic circuit Simulink model were used as inputs, including the time step. If an explicit scheme with the same discretization was chosen, the two following criteria should be satisfied for stable solutions [10]:

$$\text{advective stability} \rightarrow \left| u \cdot \frac{\Delta t}{\Delta x} \right| \leq 1 \tag{4.20}$$

$$\text{diffusive stability} \rightarrow D \cdot \frac{\Delta t}{\Delta x^2} \leq 0.5 \tag{4.21}$$

Without being able to modify the time step, since it was imported from Simulink model, there would be cases that both criteria would not be satisfied leading to unstable solutions. The major drawback of the selected implicit method is the considerably higher computational time.

A shorter form of the aforementioned equations 4.18 and 4.19 is presented below:

$$\text{if } \; u^{t+1} > 0 \; \rightarrow \; (-A_1 - A_2) \cdot c_{j-1}^{t+1} + (1 + A_1 + 2 \cdot A_2) \cdot c_j^{t+1} + (-A_2) \cdot c_{j+1}^{t+1} = c_j^t \tag{4.22}$$

$$\text{if } \; u^{t+1} < 0 \; \rightarrow \; (-A_2) \cdot c_{j-1}^{t+1} + (1 - A_1 + 2 \cdot A_2) \cdot c_j^{t+1} + (A_1 - A_2) \cdot c_{j+1}^{t+1} = c_j^t \tag{4.23}$$

with:

$$A_1 = \frac{u^{t+1} \cdot \Delta t}{\Delta x} \quad \& \quad A_2 = \frac{D \cdot \Delta t}{\Delta x^2} \tag{4.24}$$

In the above equations, all the parameters referring to new time $t+1$ are located on the LHS building a tridiagonal matrix, while the RHS includes information for the old time t. To solve the system of equations and calculate the concentration values at the new time $t+1$, Thomas algorithm was used (refer to appendix B.3). Furthermore, if the flow parameters satisfy the Taylor dispersion condition (eq. 2.30), then the above equations were solved using the Taylor diffusivity given from equation 2.26 for laminar and equation 2.29 for turbulent regime.

4.3.4. ELEMENT INTERFACE CONDITIONS

To couple the various elements of the system (fig. 4.4), a strategy with assigned values at their edges that change at every time step was followed. Based on the positive flow direction (red arrows in fig. 4.4), the first node of each element was set analogously to be at the flow inlet. So, the model includes different elements of the hydraulic network that were split spatially into nodes to solve the discretized advection-diffusion equation (eq. 4.22 or 4.23), two tee sections where the associated elements numerical schemes share a common edge node and two CSTR tanks. The liquid dissolved components concentration inside the CSTR was used as the interface value for the connected pipes and the cells separators. In this sub-section, the methodology for the coupling of the different elements and the estimation of the molar fluxes needed to calculate the CSTR tanks concentrations will be explained.

COUPLING PIPES TO CSTR TANKS

The concentration of dissolved components inside the elements that were treated as CSTR, was used as the value at the edge nodes of the relevant connected pipes and was updated at each time step as can be seen in the following figures.

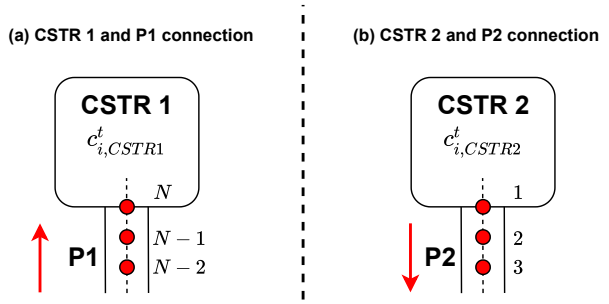

Figure 4.5: For both elements P1 & P2, the concentration at the edge nodes (N for P1 and 1 for P2) has the same value as the concentration inside the flash tanks. The subscript i refers to the examined dissolved component. The red arrows indicate the positive flow direction as presented in figure 4.4.

The component i molar flux at P1/CSTR 1 interface was estimated using the N and N-1 node as:

$$\text{if } \; u^t_{\text{P1}} > 0 \; \rightarrow \; \dot{n}^t_i = u^t_{\text{P1}} \cdot c^t_{i,N-1} - D_i \cdot \frac{c^t_{i,N} - c^t_{i,N-1}}{\Delta x} \tag{4.25}$$

$$\text{if } \; u^t_{\text{P1}} < 0 \; \rightarrow \; \dot{n}^t_i = u^t_{\text{P1}} \cdot c^t_{i,N} - D_i \cdot \frac{c^t_{i,N} - c^t_{i,N-1}}{\Delta x} \tag{4.26}$$

where the concentration of element's P1 last node (N) and element's P2 first node are equal to the concentration of i inside the corresponding CSTR. Similarly, at P2/CSTR 2 interface where the flow direction is considered positive when exits CSTR 2, the component i molar flux was estimated as:

$$\text{if } \; u^t_{\text{P2}} > 0 \; \rightarrow \; \dot{n}^t_i = u^t_{\text{P2}} \cdot c^t_{i,1} - D_i \cdot \frac{c^t_{i,2} - c^t_{i,1}}{\Delta x} \tag{4.27}$$

$$\text{if } \; u^t_{\text{P2}} < 0 \; \rightarrow \; \dot{n}^t_i = u^t_{\text{P2}} \cdot c^t_{i,2} - D_i \cdot \frac{c^t_{i,2} - c^t_{i,1}}{\Delta x} \tag{4.28}$$

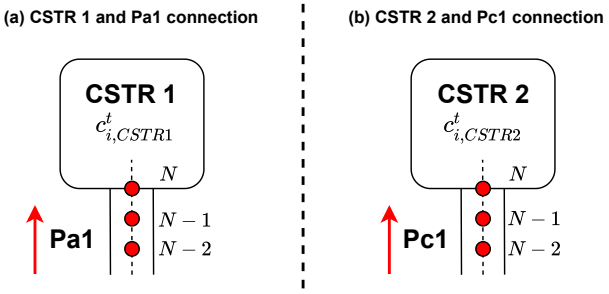

Figure 4.6: For both elements Pa1 & Pc1, the concentration at the last nodes N is set to be equal to the component i concentration inside the half-cell compartments, which is the same as the one inside the flash tanks due to the CSTR assumption.

At the interface coupling Pa1 & Pc1 to the CSTR, the molar fluxes were estimated in the same way as in equations 4.25 and 4.26 since the positive flow direction is the same.

COUPLING PIPES AT TEE SECTIONS

The hydraulic network includes two tee sections where the connected elements share a common node (3 and 4 in figure 4.1). The concentration of the examined component i at these nodes was calculated at each time step depending on the known flow behavior (splitting or mixing). An example is depicted in the following figure for the tee section (node 4) including elements P1, Pa1 and P3.

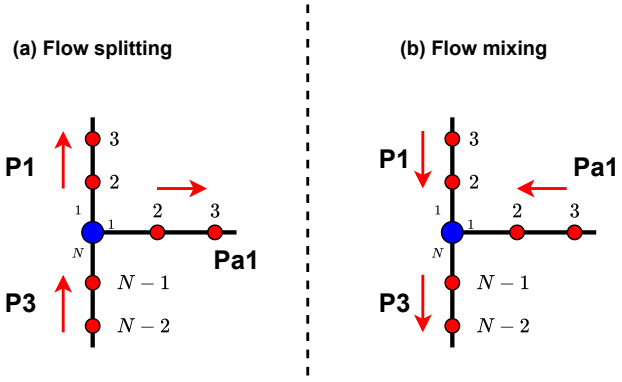

Figure 4.7: The common node with blue color serves as the last node of element P3 and the first node for both elements P1 & Pa1. When the flow splits into two branches (a), the common node concentration was set to have the same value as N-1 node of P3. When the flow is mixing (b), the concentration of node 2 for both P1 & Pa1 was taken into account.

According to figure 4.7, when the flow is splitting, the concentration of component i at the common node is equal to the N-1 node of element P3:

$$c_i^t = c_{i,N-1,\mathrm{P3}}^t \tag{4.29}$$

When the flow is mixing, the concentration is:

$$c_i^t = \frac{u_{\mathrm{P1}}^t \cdot c_{i,2,\mathrm{P1}}^t + u_{\mathrm{Pa1}}^t \cdot c_{i,2,\mathrm{Pa1}}^t}{u_{\mathrm{P3}}^t} \tag{4.30}$$

Based on the aforementioned equations, every possible flow direction was taken into account for the concentration estimation at the common node. A similar derivation was used for the second tee section at the H_2 side (node 3), connecting the elements P2, Pc1 and P3.

COUPLING SEPARATORS TO CSTR TANKS

Besides the transport of the dissolved components through the piping network, crossover happens through the separators of the cells. Each CSTR includes all half-cells of the stack, in which the flow and crossovers were assumed to be identical (CSTR 1 includes the stack anodes and CSTR 2 the stack cathodes). Consequently, the molar flow rate of the examined component i was estimated for one cell and multiplied by the number of the cells for the total flow rate that enters or exits a CSTR.

According to the model assumptions, the liquid concentration of O_2 and H_2 in both CSTR is equal to their solubility affected by the gaseous phase pressure. For the O_2

crossover, the liquid concentration in CSTR 1 was assigned at every time step to the first node of the separator's numerical scheme, multiplied by a factor (SF) to take into account the enhanced crossover due to the supersaturation phenomenon that was described in chapter 2 and the similar procedure was followed for the H_2 crossover in CSTR 2. A schematic presenting the O_2 crossover through the cell separator is included in the below figure:

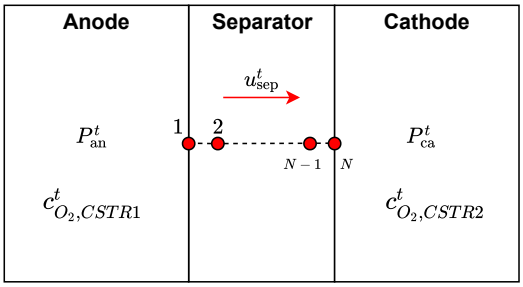

Figure 4.8: Schematic presenting the O_2 crossover from anode to cathode. The red arrow indicates the positive flow direction for greater anodic absolute pressure. The separator was split into several nodes. At time t, the first two nodes where taken into account for the flux at the anode side of the separator, while the last two nodes were used for the estimation of the flux at the cathode side.

Based on the above figure, the O_2 molar flux at the left edge of the separator (anode side) is:

$$\text{if } u^t_{sep} > 0 \rightarrow \dot{n}^t_{O_2,\text{CSTR1}} = c^t_{O_2,1} \cdot u^t_{sep} - D^{\text{eff}}_{O_2} \cdot \frac{c^t_{O_2,2} - c^t_{O_2,1}}{\Delta x} \tag{4.31}$$

$$\text{if } u^t_{sep} < 0 \rightarrow \dot{n}^t_{O_2,\text{CSTR1}} = c^t_{O_2,2} \cdot u^t_{sep} - D^{\text{eff}}_{O_2} \cdot \frac{c^t_{O_2,2} - c^t_{O_2,1}}{\Delta x} \tag{4.32}$$

The O_2 molar flux at the right side of the separator (cathode side) is:

$$\text{if } u^t_{sep} > 0 \rightarrow \dot{n}^t_{O_2,\text{CSTR2}} = c^t_{O_2,N-1} \cdot u^t_{sep} - D^{\text{eff}}_{O_2} \cdot \frac{c^t_{O_2,N} - c^t_{O_2,N-1}}{\Delta x} \tag{4.33}$$

$$\text{if } u^t_{sep} > 0 \rightarrow \dot{n}^t_{O_2,\text{CSTR2}} = c^t_{O_2,N-1} \cdot u^t_{sep} - D^{\text{eff}}_{O_2} \cdot \frac{c^t_{O_2,N} - c^t_{O_2,N-1}}{\Delta x} \tag{4.34}$$

A similar derivation was set for the opposite case of H_2 crossover through the separator from cathode to anode.

4.3.5. CSTR EQUATIONS

The last part of this model was the estimation of the O_2 and H_2 concentrations inside the CSTR tanks, which include a liquid phase with the aforementioned components in dissolved form and a gaseous phase. Data for the liquid and gaseous volume of the flash tanks at every time step were implemented from the results of the previous hydraulic circuit model, since the liquid electrolyte height in the flash tanks is known.

Based on figure 4.4, a transient total mass balance of O_2 and H_2 for CSTR 1 is:

$$\frac{dN_{O_2,\text{CSTR1}}}{dt} = \dot{N}_{O_2,\text{gen}} + \dot{N}_{O_2,\text{P1}} + \dot{N}_{O_2,\text{Pa1}} - \dot{N}_{O_2,\text{PV1}} - \dot{N}_{O_2,\text{sep,CSTR1}} \tag{4.35}$$

$$\frac{dN_{H_2,\text{CSTR1}}}{dt} = \dot{N}_{H_2,\text{P1}} + \dot{N}_{H_2,\text{Pa1}} - \dot{N}_{H_2,\text{PV1}} + \dot{N}_{H_2,\text{sep,CSTR1}} \tag{4.36}$$

where $\dot{N}_{O_2,\text{gen}}$ is the generated O_2 in the anodes, $\dot{N}_{O_2,\text{sep,CSTR1}}$ & $\dot{N}_{H_2,\text{sep,CSTR1}}$ are the dissolved quantities leaving or entering CSTR 1 through the separators while $\dot{N}_{O_2,\text{PV1}}$ & $\dot{N}_{H_2,\text{PV1}}$ are the quantities leaving the system when the valve PV1 is open. Similarly for CSTR 2:

$$\frac{dN_{H_2,\text{CSTR2}}}{dt} = \dot{N}_{H_2,\text{gen}} - \dot{N}_{H_2,\text{P2}} + \dot{N}_{H_2,\text{Pc1}} - \dot{N}_{H_2,\text{PV2}} - \dot{N}_{H_2,\text{sep,CSTR2}} \tag{4.37}$$

$$\frac{dN_{O_2,\text{CSTR2}}}{dt} = \dot{N}_{O_2,\text{Pc1}} - \dot{N}_{O_2,\text{P2}} - \dot{N}_{O_2,\text{PV2}} + \dot{N}_{O_2,\text{sep,CSTR2}} \tag{4.38}$$

The above differential equations were solved numerically with a first order forward difference formula for the time derivative term on the LHS:

$$\frac{dN_i}{dt} \approx \frac{N_i^{t+1} - N_i^t}{\Delta t} \tag{4.39}$$

To solve the aforementioned mass balances and estimate the quantities at $t+1$, the total quantity at time t was needed to be calculated. The total component i quantity inside a CSTR at time t is the sum of gas and liquid phase contributions:

$$N_i^t = N_{i,\text{g}}^t + N_{i,\text{l}}^t \tag{4.40}$$

At this point, the assumption of Henry law equilibrium between the two phases was used. According to this law, the amount of dissolved component i is proportional to its partial pressure above the liquid:

$$K_{H,i}^{cp} = \frac{c_{\text{l},i}^t}{p_i^t} \tag{4.41}$$

where $K_{H,i}^{cp}$ is the Henry constant, which has a specific value for O_2 and H_2 in aqueous potassium electrolyte (see section 4.4). Henry's law is also expressed in a dimensionless form as the ratio of the liquid over the gas concentration:

$$K_{H,i}^{cc} = \frac{c_{\text{l},i}^t}{c_{\text{g},i}^t} = \frac{N_{\text{l},i}^t \cdot V_\text{g}^t}{N_{\text{g},i}^t \cdot V_\text{l}^t} \tag{4.42}$$

where V_g^t & V_l^t are the gas and liquid phase volumes of the corresponding CSTR. For ideal gas, the conversion between the two aforementioned Henry's law expressions is:

$$K_{H,i}^{cc} = R \cdot T \cdot K_{H,i}^{cp} \tag{4.43}$$

With equations 4.40, 4.42 and 4.43, the total amount of component i at time t was estimated for use in the mass balances to calculate the $t+1$ value.

In CSTR 1 mass balances (eq. 4.35 & 4.36), the molar flow rates of O_2 and H_2 that exit the tank when the valve PV1 opens were estimated using the below approximations:

$$\dot{N}_{O_2,\text{PV1}}^t = \dot{Q}_{\text{PV1}}^t \cdot \frac{N_{O_2,\text{g}}^t + N_{H_2,\text{g}}^t}{V_\text{g}^t} \cdot \frac{p_{O_2}^t}{p_{O_2}^t + p_{H_2}^t} \tag{4.44}$$

$$\dot{N}_{H_2,\text{PV1}}^t = \dot{Q}_{\text{PV1}}^t \cdot \frac{N_{O_2,\text{g}}^t + N_{H_2,\text{g}}^t}{V_\text{g}^t} \cdot \frac{p_{H_2}^t}{p_{O_2}^t + p_{H_2}^t} \tag{4.45}$$

where $\dot{Q}_{\text{PV1}}^t$ is the gas volumetric flow rate that exits the system through valve PV1 (implemented from the previous hydraulic network model). Similar approximations were used for CSTR 2.

4.4. PHYSICAL PROPERTIES

In this section, the various physical properties that were used in the developed models will be presented. For the scope of this thesis, the thermal behavior of the system was not examined and the temperature was considered steady and equal to 90 °C (ZEF specification). Consequently, the below properties refer to this specific temperature.

ELECTROLYTE PROPERTIES

ZEF is using an aqueous 30% potassium hydroxide electrolyte. Le Bideau et al [34] published a review of different thermophysical properties for use in alkaline electrolysis modeling. They include charts and fitted equations for both $NaOH$ and KOH electrolytes at various concentrations and temperatures. From this paper, the values for density and dynamic viscosity were implemented in the models.

Table 4.3: Density and dynamic viscosity of 30% KOH electrolyte.

Parameter	Value	Unit
ρ	1300	$kg{\cdot}m^{-3}$
μ	0.08	mPa·s

OXYGEN AND HYDROGEN PROPERTIES IN KOH ELECTROLYTE

The O_2 and H_2 diffusivities were implemented by the work of Tham et al [55], who reported values for different temperatures and electrolyte concentrations.

Table 4.4: O_2 and H_2 mass diffusivities in 30% KOH electrolyte.

Parameter	Value	Unit
D_{O_2}	$2.3 \cdot 10^{-9}$	$m^2 \cdot s^{-1}$
D_{H_2}	$7 \cdot 10^{-9}$	$m^2 \cdot s^{-1}$

Regarding the solubility of O_2 and H_2 in electrolyte solutions, only a few data were found in literature and not in a wide range of temperatures. For the scope of this research, the model developed by Haug [20] in his PhD thesis was implemented, which can predict the solubility for both O_2 and H_2 in a wide range of electrolyte concentrations. The description and equations of the model are included in appendix B.1. The following figure illustrates the resulting solubilities as a function of their partial pressure.

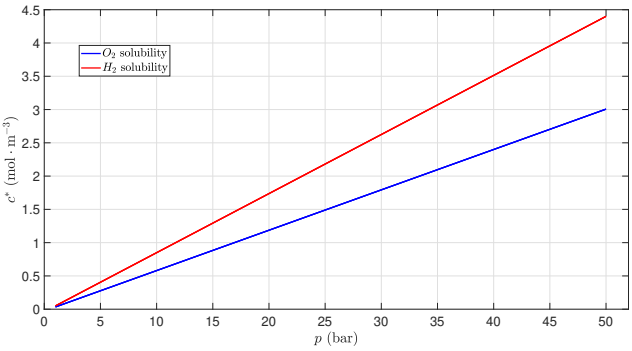

Figure 4.9: O_2 & H_2 solubilities as function of partial pressure above the liquid.

The Henry constants for both components are the slopes of the lines in the above figure and are presented in the following table.

Table 4.5: O_2 and H_2 Henry constant in 30% KOH electrolyte.

Parameter	Value	Unit
K^{cp}_{H,O_2}	0.0607	$\text{mol}\cdot\text{m}^{-3}\cdot\text{bar}^{-1}$
K^{cp}_{H,H_2}	0.0888	$\text{mol}\cdot\text{m}^{-3}\cdot\text{bar}^{-1}$

EQUATION OF STATE FOR GASES PRESSURE CALCULATION IN HYDRAULIC CIRCUIT MODEL

In the hydraulic circuit analysis model, equation 4.5 was used to calculate the mass and so the density of the accumulated electrolysis gases inside the flash tanks. To calculate the pressure, Peng Robinson equation of state (EOS) was applied [36]:

$$P = \frac{R_g \cdot T}{\nu - b} - \frac{a}{\nu\cdot(\nu+b)+b\cdot(\nu-b)} \tag{4.46}$$

where ν is the molar volume, P is the pressure, T is the temperature and R_g is the gas constant.

$$a = 0.45724\cdot\frac{R_g^2\cdot T_c^2}{P_c}\cdot\left[1+\kappa\cdot\left(1-\sqrt{\frac{T}{T_c}}\right)\right]^2 \tag{4.47}$$

$$\kappa = 0.37464 + 1.54226\cdot\omega - 0.26992\cdot\omega^2 \tag{4.48}$$

$$b = 0.0778\cdot\frac{R_g\cdot T_c}{P_c} \tag{4.49}$$

where ω is the acentric factor, and T_c & P_c are the critical temperature and pressure respectively. The following table includes the used values in Peng Robinson equation of state.

Table 4.6: O_2 and H_2 parameters used in Peng Robinson EOS.

Parameter	Oxygen	Hydrogen	Units
T_c	-118.6	-240	^{o}C
P_c	5050	1298	kPa
ω	0.022	-0.22	-

SEPARATOR PROPERTIES

Some properties for Zirfon Perl separators are included in the manufacturer's data sheet and others are experimentally estimated and reported in literature. The following table summarizes all these properties that were used in the models.

Table 4.7: Zirfon Perl separator properties.

Parameter	Value	Unit	Reference
L_{sep}	0.5	mm	[52]
ϵ	0.5	-	[1]
τ	3.14	-	[22]
K	$2\cdot10^{-16}$	m^2	[58]

5

RESULTS AND DISCUSSION

5.1. INTRODUCTION

In this chapter, the results of the two models will be presented and analyzed. Section 5.2 deals with the transient hydraulic network model that was developed to predict the electrolysis system dynamic response concerning gas production and process control. Section 5.3 presents the results of the second model that was developed to quantify the level of gas crossover induced by the predicted behavior of the first model.

5.2. ELECTROLYSIS SYSTEM DYNAMIC RESPONSE MODEL

5.2.1. INITIAL CONDITIONS

In addition to the geometrical aspects and physical properties that were presented in chapters 3 and 4, initial conditions were also implemented as a starting point of the simulations since the model is transient. These conditions are associated with the initial values of the various differential equations and were kept the same for all the simulated cases.

At time zero, the system was set to be calm, meaning that the liquid electrolyte velocity is zero in all the elements (figure 4.1). The initial electrolyte level in the O_2 flash tank was set to be 6 mm above the level sensor height since the guidance for future experiments is to fill the system with electrolyte until this sensor is wet. To have a balance and not electrolyte movement between the two sides, the corresponding level in the H_2 flash tank was set analogously by also taking into account the height difference between the two flash tanks. The initial gas pressure above the liquid electrolyte was set to be atmospheric in both flash tanks. The aforementioned initializations are summarized in the below table.

Table 5.1: Electrolysis system dynamic response model initial conditions. The initial velocity u was set to be zero for all the network elements.

Parameter	Value	Unit
u	0	$m \cdot s^{-1}$
y_{t1}	65	mm
y_{t2}	95	mm
$P_{g,t1}$	1.01325	bar
$P_{g,t2}$	1.01325	bar

5.2.2. ZEF SPECIFICATIONS

In this subsection, the results of the first model for the ZEF system specifications will be presented. A configuration with 18 cells and 3330 $A \cdot m^{-2}$ current density was simulated. The simulation duration was 3600 s.

FLASH TANKS GAS PRESSURE

Figure 5.1 depicts the behavior of O_2 and H_2 pressures in the flash tanks. With a first look, the two different operating states are noticeable. The first state is the system's startup, where the pressure increases till the control point of 50 bar. At this time interval that lasts around 386 s, only the purging valve at the O_2 side (PV1 in figure 4.1) is operating to maintain the electrolyte level above the control point of 59 mm. Subsequently, the main operating state of the system is visible with both purging valves working to control the electrolyte level and pressure. As will be seen later in the electrolyte level graphs, when the pressure in the H_2 flash tank reaches 50 bar, PV2 valve opens and the electrolyte is moving from O_2 to H_2 side. Once the level sensor in the O_2 flash tank becomes dry, the PV1 valve also opens and this simultaneous valve operation leads to a pressure drop of around 4 bar.

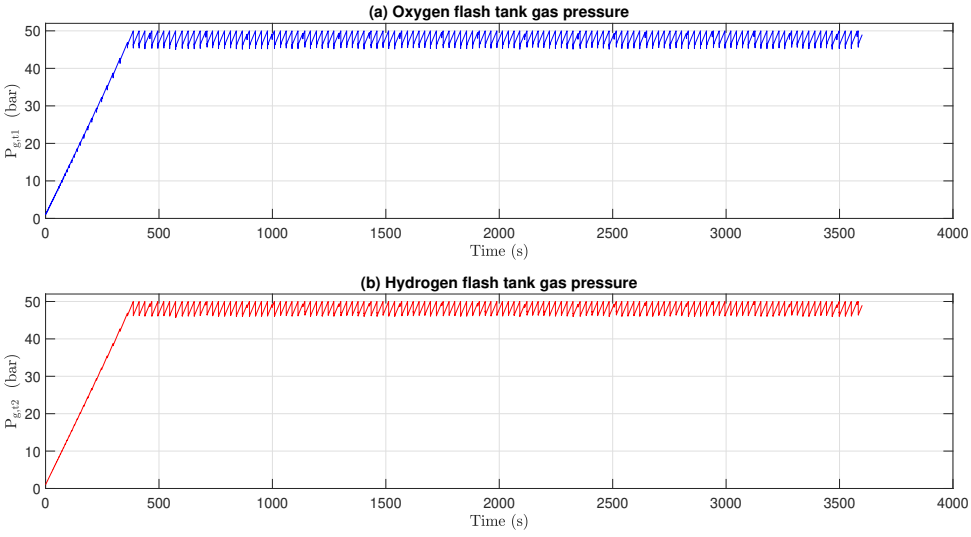

Figure 5.1: Overview of (a) O_2 and (b) H_2 pressure response in the corresponding flash tanks for a simulation duration of 3600 s.

Moreover, another observable difference between the two graphs is that the pressure drop seems to be slightly larger in the O_2 flash tank. A closer view focused on a valve opening during the main operating state is included in figure 5.2 to give a better insight of the pressure response.

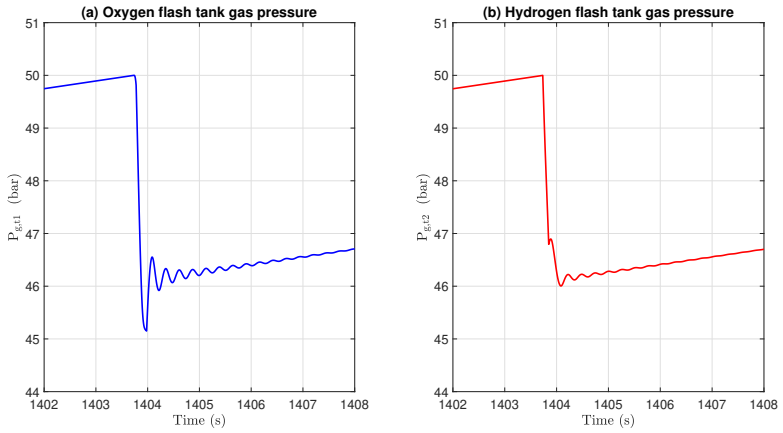

Figure 5.2: Pressure drop and oscillatory behavior caused by the simultaneous valve opening during the main operating state of the system in (a) O_2 and (b) H_2 flash tanks.

Figure 5.2 indicates the level of pressure drop and the oscillatory behavior that is induced right after the close of the valves. The larger pressure decrease in the O_2 flash tank that was visible in figure 5.1 is caused by the higher amplitude of the oscillation. For the O_2 flash tank the maximum amplitude is around 1 bar, while for the H_2 flash tank, it is 0.18 bar. This is happening probably due to the different volumes of the tanks and the different gas production rates. For both cases, the oscillatory behavior is damping and almost vanishes after 3 s. Another noticeable fact is a sharp and slight pressure increase in the H_2 flash tank at around 47 bar just before 1404 s. This 'disturbance' is caused when the H_2 side valve (PV2) closes but the electrolyte control valve (PV1) is still open.

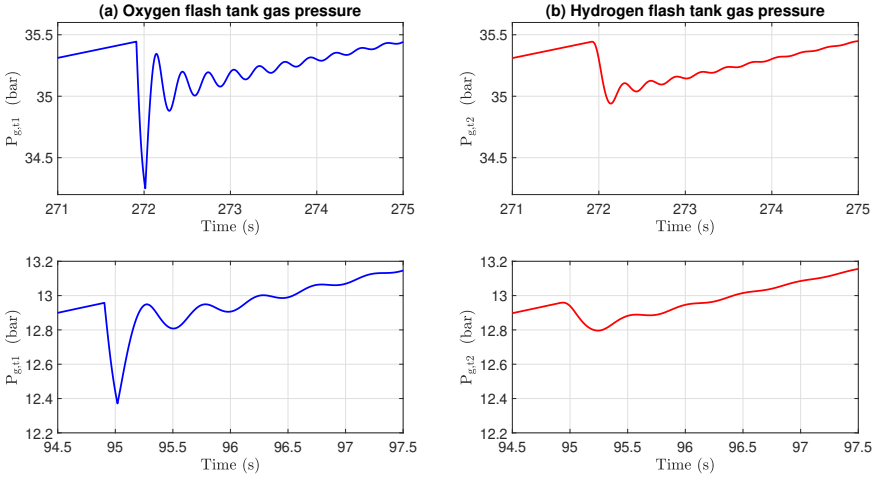

Figure 5.3: Pressure drop caused by the electrolyte level control valve (PV1) in (a) O_2 flash tank and (b) H_2 flash tank during the system startup at different times.

In addition to the previous graph, figure 5.3 shows the pressure drop caused in both flash tanks from the O_2 side valve (PV1) operation at different times during the system

startup. Here the response is similar with higher oscillation amplitude for the O_2 tank pressure. Furthermore, the pressure drop induced by the valve decreases in lower pressures since the mass flow rate passing through the valve is higher for larger upstream (tank) and downstream (environment) pressure difference.

A more general observation from figures 5.2 and 5.3 is that the higher oscillation amplitude of O_2 pressure is causing an instantaneous larger pressure difference between the two sides that reaches a maximum value of around 1.69 bar during the main operating state. The effect of these oscillations with the fluctuating pressure difference is of high importance for the integrity of the separators in the stack, as there is a risk of rupture [41] with consequences for the whole system due to the mixing of the electrolysis gases that will be caused in case of separators failure. This differential pressure between the anodes and cathodes will be discussed in the following paragraph.

PRESSURE DIFFERENCE BETWEEN THE HALF-CELL COMPARTMENTS

The different cells of the stack are connected in series and an estimation of the absolute pressure was made by taking the average value of the network nodes that are located before and after the stack elements (Pa2 for anodes & Pc2 for cathodes). These nodes as presented in figure 4.1 are 4a & 4b for the anodes and 3a & 3b for the cathodes.

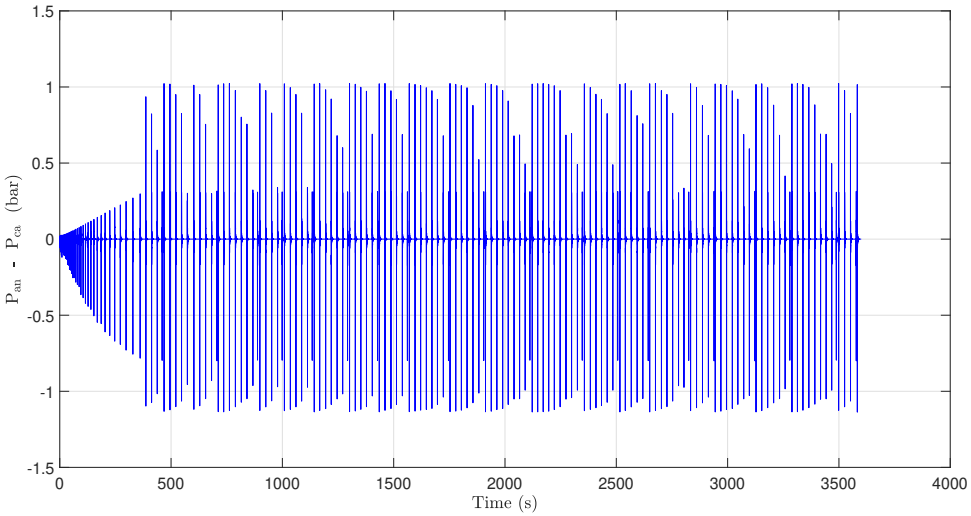

Figure 5.4: Overview of the differential pressure between the anodes and cathodes of the stack in the whole simulation time range.

Figure 5.4 illustrates the differential pressure between the half-cell compartments that is caused by the operation of the valves. It is clear that the simultaneous valve opening during the main operating state is responsible for high-pressure difference spikes that reach an absolute value of 1.137 bar. It should be mentioned that this pressure difference may be overestimated since the flow was assumed to be incompressible. Part of these pressure gradients may be absorbed by the bubbles leading to lower values than the predicted. In the time intervals when the valves do not operate and electrolyte flows slowly from O_2 side to H_2 side, the anodic/cathodic absolute pressure difference has a very low average value of 8 Pa (higher anodic).

FLASH TANKS ELECTROLYTE LEVEL

Figure 5.5 shows an overview of the electrolyte level response in both flash tanks. As in the case of the pressure response, the two operating states can be identified. Before the pressure reaches the control point of 50 bar for the first time (at 386 s), the electrolyte level in the O_2 flash tank is constantly kept above the level sensor height (59 mm) and the valve operation contributes with an average of 8 mm level rise (from 59 mm to 67 mm). It can also be seen that the fluctuations are denser close to zero time. This indicates that during the startup period, the O_2 tank valve operates less frequently as time passes. Every time the valve opens, the upstream O_2 pressure is higher than in the previous opening resulting in a higher pressure drop (as explained in figure 5.3). Therefore, more mass is lost at higher pressure drops, but the gaseous O_2 mass entering the tank, which is produced in the anodes, is the same. This is the reason for the observed delay between the aforementioned valve opening at the startup. At the main operating state, larger fluctuations of the electrolyte level are observed since the two valves can operate simultaneously. Regarding the electrolyte level in the H_2 flash tank, it follows exactly the opposite direction.

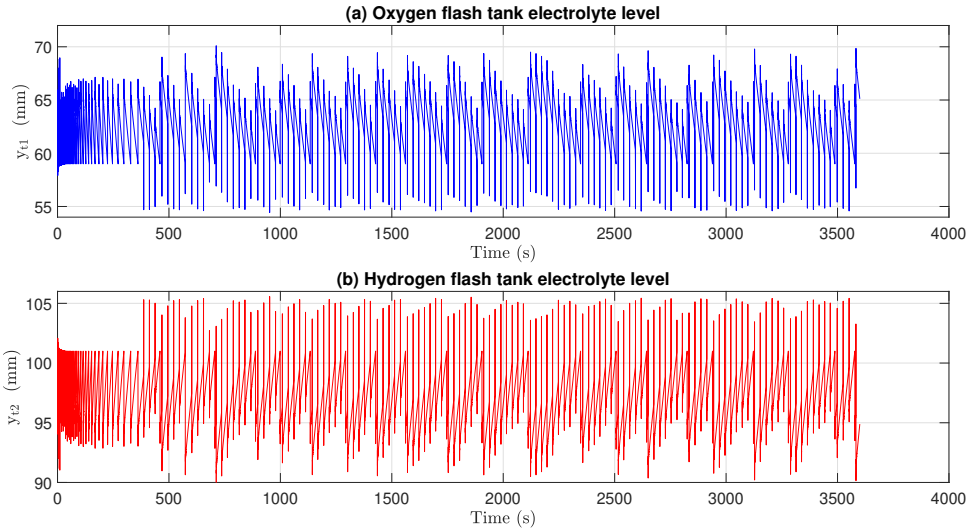

Figure 5.5: Overview of electrolyte level response in (a) O_2 and (b) H_2 flash tanks.

Figure 5.6 depicts a closer look at the electrolyte oscillating behavior caused right after the O_2 flash tank valve (PV1) closes during the startup period with the gas pressure being around 29.3 bar. A maximum amplitude of 1.3 mm is observed, while the oscillating profile is completely damped after 5 s. As mentioned before, the electrolyte response in the H_2 tank follows exactly the opposite behavior. When the O_2 side valve opens at 224.5 s, electrolyte is moving from H_2 to O_2 side causing a decrease (H_2 tank) and increase (O_2 tank) of the levels respectively. After the closure of the valve, the electrolyte is slower following the opposite direction from O_2 to H_2 side due to faster pressure increase as described in chapter 3.

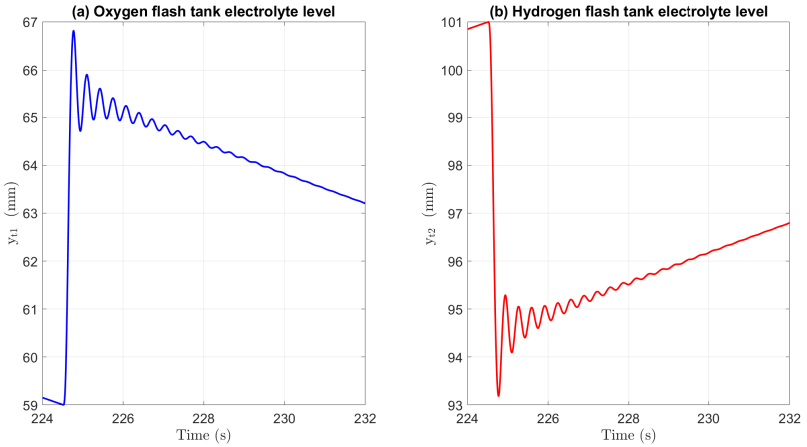

Figure 5.6: Electrolyte level response caused by the O_2 flash tank valve opening during the system startup.

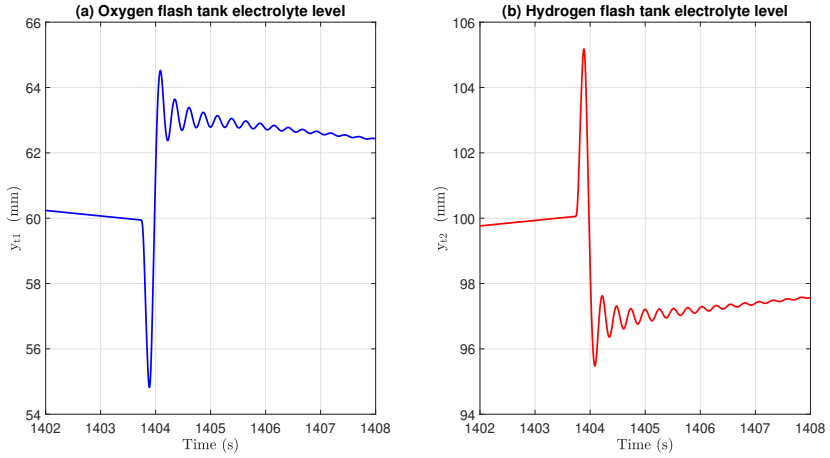

Figure 5.7: Electrolyte level response by both valves simultaneous operation during the normal operating state.

Figure 5.7 illustrates a simultaneous opening of both purging valves during the main operating state. At 1403.8 s, the pressure in H_2 flash tank reaches the control point of 50 bar and so PV2 opens. This leads electrolyte to move faster from O_2 to H_2 side resulting in a sharp decrease of the liquid level in O_2 flash tank. Once the level goes below 59 mm (in this case happens almost instantly after PV2 opens), which is the level sensor (LS1) height, O_2 side purging valve PV1 opens. If after the close of PV1 (100 ms) the level is still below 59 mm, it opens again with the same duration, as happens in this figure. This simultaneous operation of both purging valves leads to an average pressure drop of 4 bar as was illustrated and discussed in figure 5.2. After the valve closure, a similar to the previous figures oscillating behavior is observed with also small amplitude and fast damping.

FLOW IN NETWORK PIPES

Figure 5.8 illustrates the electrolyte mass flow rate and direction during the main operating state with both purging valves closed. As can be seen, it is flowing slowly from O_2 side to H_2 side under the effect of the pressure difference between the two flash tanks. Furthermore, the electrolyte flow through the stack anodes (element Pa2) is opposite from the flow of the produced bubbles. This was expected since the buoyancy effect of the bubbles was not considered in the model derivation and the pressure difference between the two flash tanks was assumed to be the driving force. The electrolyte flow rate through the mixing pipe P3 is on average $2.19{\cdot}10^{-4}$ kg·s^{-1} with a direction to the H_2 side. Moreover, when valve PV2 opens to control the pressure, larger O_2 flow rates entering the H_2 side are expected since O_2 was already flowing towards that direction (see figure 5.18). Dissolved H_2, flows to the O_2 side through the mixing line only when the electrolyte control valve (PV1) operates. The crossovers will be discussed in section 5.3.

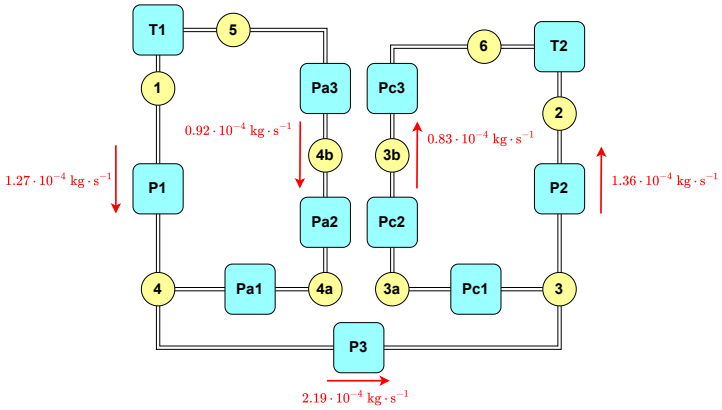

Figure 5.8: Electrolyte flow in the network during the main operating state when the valves are closed and fluctuations caused by oscillations are damped.

Figure 5.9 illustrates the pipe mass flow rate response caused by the O_2 flash tank valve (PV1) opening during the startup period (at the same time interval as in figure 5.6). For comparative purposes, the two branched flow nodes (3 & 4) of the network are used. Thus, as depicted in figure 5.8, the O_2 side node 4 is associated with elements P1, Pa1 and P3. Similarly, the H_2 side node 3 connects P3 to elements Pc1 and P2. The positive and negative values of the flow rates indicate the flow direction as it was set in the mathematical model derivation and illustrated in figure 4.2.

As can be seen in figure 5.9, the valve opening triggers a maximum instantaneous flow rate of 0.07 kg·s^{-1} at the mixing pipe P3. At node 4, the flow splits to 0.038 kg·s^{-1} through element P1 and 0.032 kg·s^{-1} through element Pa1. At node 3 respectively, a flow of 0.042 kg·s^{-1} through element P2 and 0.028 kg·s^{-1} through Pc1 mixes to element P3. The electrolyte flow through the stack cathodes (flow rate in element Pc1) is counter-current from the bubbles flow when the PV1 valve is triggered. As in the previous graphs related to pressure and electrolyte level response, the oscillatory behavior is almost completely damped after 5 s. These spikes of flow rate are important since trigger the mass transport of dissolved H_2 towards the O_2 side through the mixing element P3 during the system's startup.

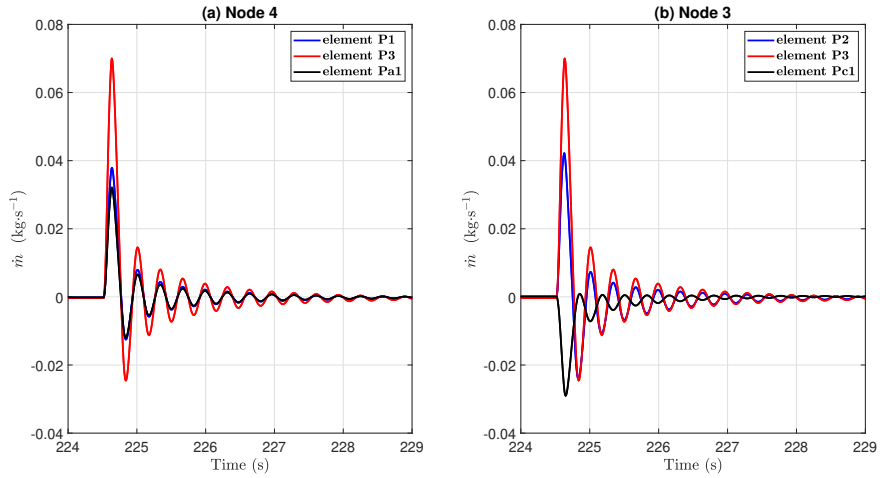

Figure 5.9: Mass flow rates through the elements that are branched in (a) node 4 and (b) node 3 as caused by the O_2 flash tank valve opening during the system startup. The negative values indicate an opposite flow direction from that illustrated in figure 4.2.

Figure 5.10 illustrates a similar mass flow rate response over a simultaneous opening of both purging valves during the system's main operating state (at the same time interval as in figure 5.7). Here, the effect of the O_2 side valve (PV1), which opens right after the other valve (PV2) to control the electrolyte level, is visible. Firstly, when the pressure control valve (PV2) opens, flow is forced towards the H_2 flash tank with a maximum rate of 0.068 kg·s^{-1} in element P3. The simultaneous twice opening of electrolyte control valve PV1 causes an enhanced backward instantaneous flow rate of 0.094 kg·s^{-1} in element P3 towards the O_2 side.

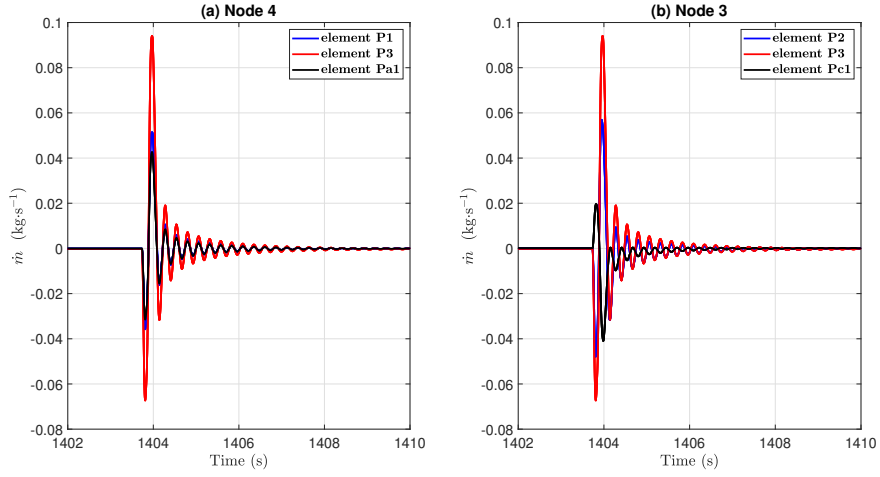

Figure 5.10: Mass flow rates through the elements that are branched in (a) node 4 and (b) node 3 as caused by the simultaneous valve opening during the main operating state of the system. The negative values indicate the opposite flow direction from that presented in figure 4.2.

5.2.3. DIFFERENT CURRENT DENSITIES

In subsection 5.2.2, the transient dynamic response of the ZEF electrolysis system operating at the target current density of 3330 $A \cdot m^{-2}$ was characterized. Here, the effect of different current densities will be discussed.

As described in chapter 3, the examined electrolysis system is self-pressurized, meaning that the operating pressure increases due to the continuous O_2 and H_2 evolution in the stack cells. The produced gases are released at the electrodes in bubble form, driven to the flash tanks where are separated from the liquid electrolyte and finally accumulated at the top side of the flash tanks and in the buffers. The gases production rate was calculated using Faraday's theoretical equations 2.7 & 2.8, which depend on current density. Therefore, for the same electrode surface area, the rate of gas production increases at higher current densities. For the ZEF system, this means that the pressure build-up is slower as the current density decreases resulting in longer startup periods, slower electrolyte movement when the purging valves do not operate and consequently less frequent valve opening.

Table 5.2: Effect of current density on the produced gases mass flow rate and system's startup duration.

$j\,(A \cdot m^{-2})$	$\dot{m}_{O_2}\,(kg \cdot s^{-1})$	$\dot{m}_{H_2}\,(kg \cdot s^{-1})$	Startup duration (s)
500	$4.728 \cdot 10^{-6}$	$5.910 \cdot 10^{-7}$	2568
1000	$9.456 \cdot 10^{-6}$	$1.182 \cdot 10^{-6}$	1297
2000	$1.891 \cdot 10^{-5}$	$2.364 \cdot 10^{-6}$	645
3000	$2.837 \cdot 10^{-5}$	$3.546 \cdot 10^{-6}$	430
4000	$3.782 \cdot 10^{-5}$	$4.728 \cdot 10^{-6}$	321
5000	$4.728 \cdot 10^{-5}$	$5.910 \cdot 10^{-6}$	259

Table 5.2 shows how the varying current density affects the electrolysis system startup duration. As expected, the pressure build-up period is higher at larger current densities, with 4.3 min duration at 5000 $A \cdot m^{-2}$ and almost 10 times longer period at 500 $A \cdot m^{-2}$ (42.8 min). The small divergence from linearity can be explained by the difference in the valve opening frequency. The rest parameters (gas pressures, electrolyte level, mass flow rates) present similar response with the already included in subsection 5.2.2 results for the ZEF target current density, with similar amplitudes and oscillating behavior. Consequently, the effect of current density concerning the system's dynamic response is mainly detected on startup duration and valve opening frequency. In the following section, the effect of current density on gas crossovers will also be presented and discussed.

5.3. CROSSOVERS MODEL

5.3.1. INITIAL CONDITIONS AND NUMERICAL SCHEMES NODES NUMBER

The model developed to estimate the level of gas crossovers uses data from the output of the first hydraulic network model. Therefore, the initial conditions for the pipe velocities, electrolyte level in the flash tanks (and thus gas and liquid volumes) and gas pressures mentioned in table 5.1 hold also for this model.

The rest parameters that were initialized are the O_2 and H_2 concentrations at the various model's elements as are depicted in figure 4.4. For all the spatial discretized elements (P1, P2. Pa1, Pc1 and separator), the concentrations of both O_2 and H_2 at the internal nodes were initially set to be zero. The same value was also set at the two tee

sections. Table 5.3 includes the initial concentrations at the two CSTR, which are also the edge values of the corresponding connected elements as described in chapter 4.

Table 5.3: CSTR component concentrations initial values for the crossovers model.

Parameter	Value	Unit
$c_{O_2,\text{CSTR1}}$	0.0615	$\text{mol}\cdot\text{m}^{-3}$
$c_{H_2,\text{CSTR1}}$	0	$\text{mol}\cdot\text{m}^{-3}$
$c_{O_2,\text{CSTR2}}$	0	$\text{mol}\cdot\text{m}^{-3}$
$c_{H_2,\text{CSTR2}}$	0.09	$\text{mol}\cdot\text{m}^{-3}$

For CSTR 1 that includes the stack anodes, pipe Pa3 and the O_2 flash tank, the initial O_2 concentration was set equal to its solubility at 1 bar (initial gas pressure) and similarly for H_2 in CSTR 2 (stack cathodes, pipe Pc3 and H_2 flash tank). Moreover, initially, no trace of O_2 and H_2 was assumed at the opposite side (CSTR 2 and CSTR 1 respectively) setting these concentrations to zero. At the edges of the separator, the concentrations of the corresponding sides were set equal to the solubilities multiplied by a supersaturation factor that varied in a range of 1-50 for both components.

Since the advection-diffusion equation was solved numerically using the Finite Difference Method, a 'nodal number' dependence study was conducted to ensure the accuracy of the final solution. The same number of nodes was used for the elements representing the pipes of the network and a different selection was made for the separator. This nodal dependence study can be found in appendix B.2. The final selection was 300 nodes for the pipes and 200 for the separator.

5.3.2. ZEF SPECIFICATIONS

A first study on the gas crossovers was conducted for the ZEF target current density of 3330 $\text{A}\cdot\text{m}^{-2}$. As mentioned in section 2.4.2, the local supersaturation phenomenon happening at the electrode boundary layer that is responsible for larger molar fluxes through the cell separators was taken into consideration by using an enhancement factor (SF) of the dissolved gases solubility at the separator edge nodes in both CSTR. The same factor was assumed for both H_2 and O_2. Considering the complexity of the ZEF system with the continuously fluctuating pressures and flows, the model simplifications that could not take accurately into account the local mass transfer phenomena inside the half-cells (CSTR assumption) and the lack of wide research on supersaturation to formulate a reliable model (wide range of current densities, temperatures, pressures and materials), the use of a fixed supersaturation factor aims to provide a preliminary view of the enhanced crossovers caused by the possible level of this phenomenon.

NEGLECTING SUPERSATURATION

Figure 5.11 presents the gas and liquid H_2 content in O_2 tank (CSTR 1) in the whole simulated period by firstly neglecting the electrolyte supersaturation (SF=1). A first look at the chart indicates an almost linear increase during the first 500 s. This is logical considering that this time interval includes the startup period of the system (386 s) when only the valve in the O_2 flash tank operates frequently causing, as viewed in figure 5.9, higher mass transfer to the O_2 side through the pipes. Apart from that, the pressure increase in the flash tanks over this period causes higher dissolved component concentration and thus enhanced mass fluxes both through the separators and the pipes. More specifically, the

H_2 solubility increases linearly from 0.09 mol·m^{-3} at 1 bar to almost 4.5 mol·m^{-3} at 50 bar (figure 4.9). After the first 500 s, the H_2 content increases slower up to 1500 s when it seems to reach a steady average value of 0.1154 mol% in the gas phase and 0.1687 mol% in the liquid phase, values much lower from the LEL of 5.3 mol% H_2 [47].

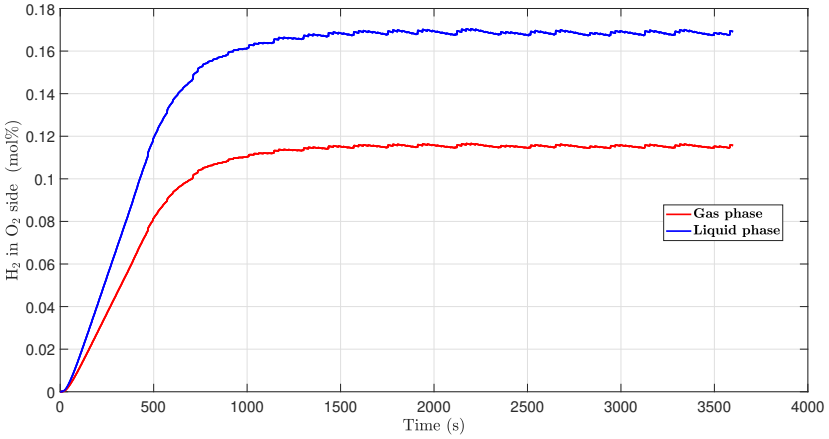

Figure 5.11: Gas and liquid H_2 content in the O_2 side (flash tank + half-cells) during the whole simulating period and without electrolyte supersaturation.

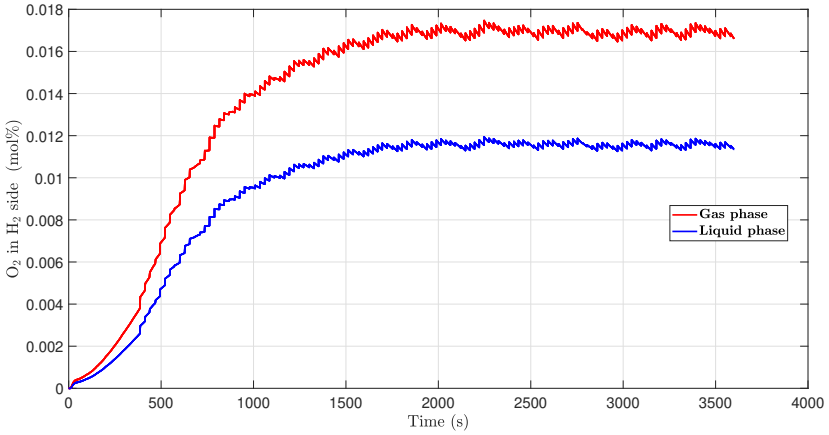

Figure 5.12: Gas and liquid O_2 content in the H_2 side (flash tank + half-cells) during the whole simulating period and without electrolyte supersaturation.

A similar curve for the O_2 content in H_2 tank (CSTR 2) is depicted in figure 5.12. In this case, the difference in the rate of molar fraction increase between the startup and the main operating state is visible. During the startup, O_2 reaches the opposite side through the separators and the mixing line (element P3) at the time intervals when the electrolyte level control valve (PV1) does not operate. After the first 386 s (startup) when the pressure control valve (PV2) starts operating, higher mass transfer is forced towards the H_2 side resulting in a higher dissolved O_2 transfer through the pipes. As in the case of H_2 crossover,

the O_2 content in the H_2 side tends to stabilize after 2000 s and fluctuates under the effect of the purging valves opening with an average value of 0.0169 mol% in the gas phase and 0.0116 mol% in the liquid phase. This means a H_2 purity of more than 99.9 mol% that is much higher than the UEL of 95 mol% [47].

Making a comparison between figures 5.11 and 5.12, it is clear that by neglecting the supersaturation effect, the induced gas crossovers in the context of the ZEF electrolysis system are very low in both flash tanks without a risk of falling into the explosive limits of H_2 & O_2 mixtures. Moreover, the different rate of increase and the final almost steady level of content between the two gases are noticeable with H_2 crossover increasing faster and having a higher content during the main operating state. The higher level of H_2 crossover, which is also reported in literature [22], [45], is attributed to several reasons. Firstly, H_2 has higher molecular diffusivity in aqueous KOH solutions compared to O_2 (see table 4.4), which results in higher diffusive fluxes through the separators of the cells and the piping system. Furthermore, as mentioned before, the H_2 quantity produced in the stack cells is twice larger than the O_2. Apart from these physical reasons, for the specific ZEF electrolysis system, H_2 is forced faster through the piping system to the O_2 side during the startup due to the O_2 flash tank valve operation.

SUPERSATURATION EFFECT

Figure 5.13 illustrates how the gaseous H_2 content in O_2 flash tank is affected by implementing at the edges of the cells separators a supersaturation factor (SF) up to 50 times greater than the solubility. It is evident that this phenomenon can have a strong enhancing influence on the H_2 crossover as an SF increase by 10 induces around 1% higher content. Consequently, when the supersaturation of H_2 is 50 times greater than the solubility, the model predicts a content of 5.2 mol% H_2 in the O_2 flash tank that is slightly below the LEL of 5.3 mol%.

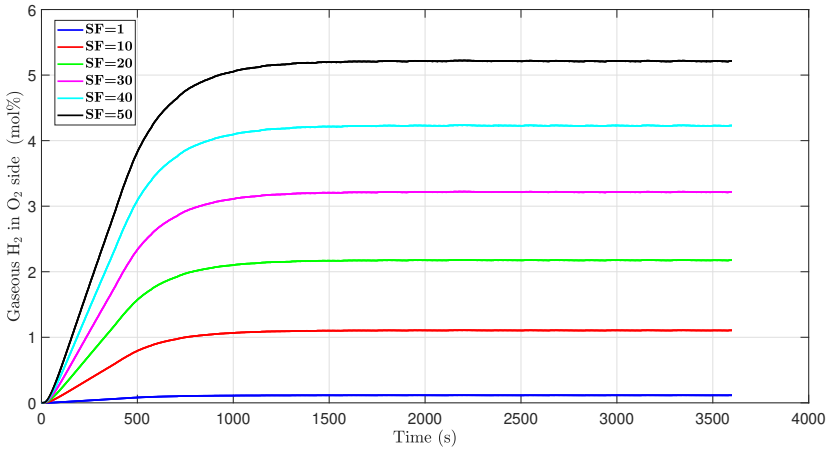

Figure 5.13: Gaseous H_2 content in the O_2 side during the whole simulating period and as a function of supersaturation (SF varies between 1 and 50).

Figure 5.14 illustrates the effect of supersaturation for the case of O_2 crossover. An increase of SF by 10 induces around 0.1% higher content, which is significantly lower in comparison to the corresponding H_2 increase that was observed in figure 5.13. Furthermore,

for SF=50, the O_2 molar fraction does not impose a risk for explosive mixture, since the H_2 purity is predicted to be 99.41%.

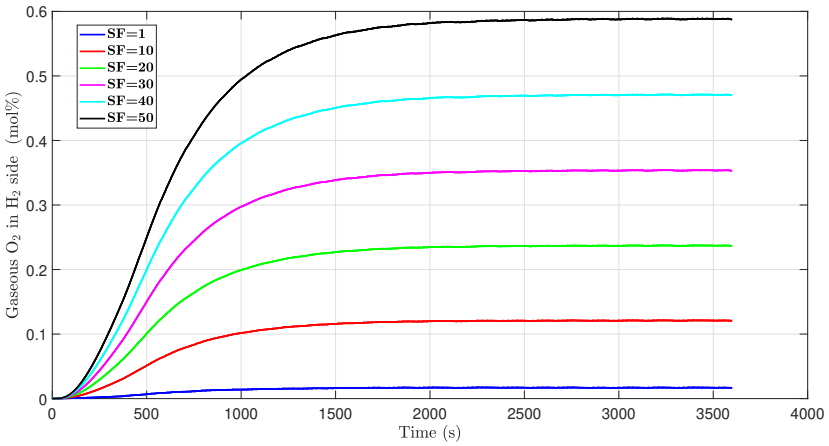

Figure 5.14: Gaseous O_2 content in the H_2 side during the whole simulating period and as a function of supersaturation (SF varies between 1 and 50).

Table 5.4 summarizes the electrolysis gases stabilized average contents in the opposite side tank during the main operating state and for different supersaturation factors as were presented in figures 5.13 and 5.14.

Table 5.4: Results of the average stabilized gases content in the opposite side tank for increasing supersaturation factor (SF).

Parameter	SF=1	SF=10	SF=20	SF=30	SF=40	SF=50
H_2 in O_2 (mol%)	0.1154	1.1049	2.1750	3.2154	4.2275	5.2123
O_2 in H_2 (mol%)	0.01693	0.1207	0.2365	0.3528	0.4696	0.5868

5.3.3. CROSSOVERS BREAKDOWN

In this subsection, a breakdown of the induced crossovers will be presented to identify which mass transfer mechanism dominates. This will be done firstly for the cells separators, to investigate if the pressure spikes caused by the operation of the valves (figure 5.4) induce high convective flows that dominate over the diffusive. Furthermore, the crossover contribution through the stack separators will be compared to the one induced by the mixing electrolyte cycles.

MOLAR FLOW RATE THROUGH THE SEPARATORS

Figure 5.15 compares the total H_2 convective and diffusive molar flow rates that enter the O_2 side through the 18 separators of the stack by neglecting the supersaturation effect (SF=1). It is clear that diffusion is dominant in the whole operating window of the system. The opening of the valves is causing instantaneous fluctuations in both convective and diffusive contributions. When the valves are closed and the oscillations damped, the convective contribution is practically zero (8 Pa pressure difference as discussed in figure 5.4), while diffusion causes an average molar flow rate of 1.08 μmol·s^{-1}. The fluctuations of the diffusive contribution are caused by the convection term since the back and forth mass movement is causing locally higher or lower concentration gradients.

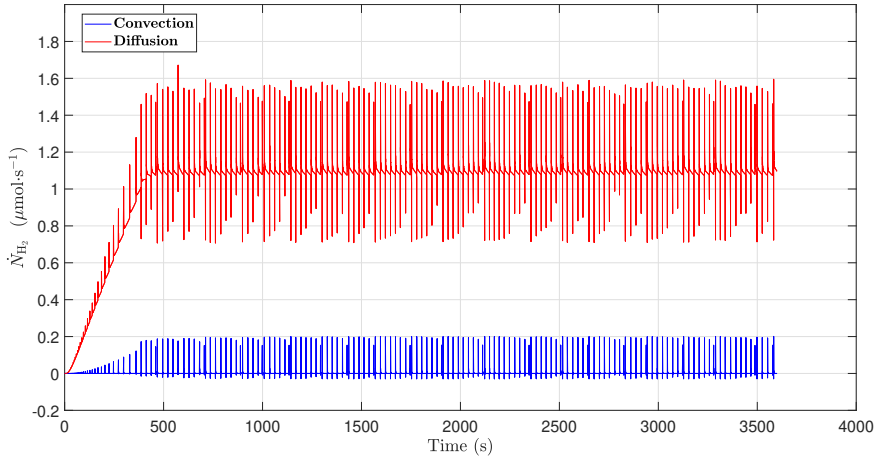

Figure 5.15: Total H_2 molar flow rate that enters the O_2 side (CSTR 1) through the separators of the cells due to convection and diffusion.

Similarly, figure 5.16 depicts the O_2 molar flow rate contribution of convection and diffusion that enter the H_2 side through the separators without the effect of supersaturation. As in the case of H_2 crossover, diffusive flow rates are higher than convective except for some amplitudes caused by the valves during the main operating state. When the valves are closed and oscillations damped, the average diffusive flow rate is 0.225 μmol·s^{-1} and the pressure driven convective is insignificant.

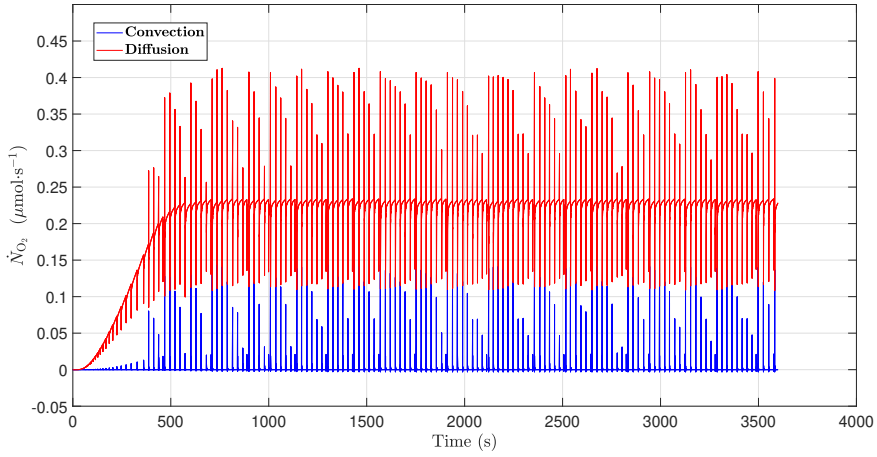

Figure 5.16: Total O_2 molar flow rate that enters the H_2 (CSTR 2) side through the separators of the cells due to convection and diffusion.

Comparing figures 5.15 and 5.16, the H_2 crossover molar flow rate through the separators is higher as was shown and expected by the previous graphs (5.11 & 5.12). In both cases, the diffusion mechanism of mass transport dominates with a greater influence on H_2 crossover (reasons already explained). The convective mechanism enhances the crossover of both components when the operation of the valves is causing pressure gradients between

the half-cell compartments. The maximum share of the convective mechanism during these pressure gradients is around 13% for H_2 and 26% for O_2 compared to the total crossover flow rate.

The influence of the mass transport mechanisms is also indicated with the dimensionless Péclet number [25], which is widely used to characterize both heat and mass transport phenomena and is defined as the ratio of the convective transport rate over the diffusive transport rate.

$$\mathrm{Pe} = \frac{u \cdot L}{D} \tag{5.1}$$

where u is the flow velocity, L is the characteristic length and D is the diffusion coefficient. For the flow through the separators, L is the thickness of Zirfon Perl membrane (0.5 mm) D is the effective diffusivity of H_2 or O_2 (eq. 2.11), while the velocity u is calculated from the Darcy equation (eq. 2.16). Table 5.5 presents the maximum Péclet values that are caused during the main operating state of the system and the minimum values when the valves are closed.

Table 5.5: Effective diffusivity of H_2 and O_2 in Zirfon Perl separators and Péclet number for the maximum and minimum pressure gradients between the half-cell compartments.

Component	$D^{\mathrm{eff}}\,(\mathrm{m^2 \cdot s^{-1}})$	max Pe	min Pe
H_2	$1.115 \cdot 10^{-9}$	25.5	0.002
O_2	$0.366 \cdot 10^{-9}$	77.6	0.006

The Péclet number values in the above table reflect the molar flow rates presented in figures 5.15 and 5.16. When the valves are closed and the pressure difference between the anodes and the cathodes is insignificant, the Péclet number gets its minimum value for both components, with Pe«1, meaning that the mass transport is almost purely diffusive. When the pressure difference gets its maximum value (1.137 bar in figure 5.4), the Pe number is also maximized indicating the effect of convection. Moreover, the maximum Pe for O_2 mass transport is 3 times higher than the one for H_2. This difference can be seen in the aforementioned molar flow rate figures, where the 'gap' between the convective and diffusive contributions for H_2 is larger than for O_2 reflecting the lower share of H_2 convection to the total flow rate.

In the previous crossovers breakdown analysis, the effect of supersaturation was neglected. If it is taken into account, the molar flow rates are proportional to the supersaturation factor (SF), since the concentration at the separator edges (equal to the solubility of O_2 at the anodes and H_2 at the cathodes) is multiplied by this factor. Therefore, the flow rate response depicted in figures 5.15 and 5.16 will be enhanced by the used SF.

MOLAR FLOW RATE THROUGH THE PIPES

In this paragraph, the molar flow rate of the dissolved components entering the opposite side tanks will be presented. Based on figure 4.4, element P3 is the mixing tube letting dissolved components move towards the opposite side tank. Thus, dissolved saturated O_2 can exit from CSTR 1 through elements P1 and Pa1, ending up to CSTR 2 through elements P2 and Pc1. Exactly the opposite route holds for the dissolved H_2. When the valves are closed, as shown in figure 5.8, liquid electrolyte is moving slowly from O_2 side to H_2 side. So, higher concentrations of O_2 are expected to pass through P3 and end up in elements P2 and Pc1. On the contrary, H_2 is driven to the O_2 side via mixing pipe P3 when the electrolyte level control valve (PV1) operates.

Figure 5.17 illustrates the total H_2 molar flow rate that enters the O_2 side through elements P1 and Pa1. As can be seen, during the startup (first 386 s), the highest instantaneous molar flow rates are on average less than 1 μmol·s^{-1} and are caused by the O_2 side valve operation (PV1), which opens to control the electrolyte level. After around 500 s, when the system is in its main operating state, large variations are observed. These flow rate spikes that reach a maximum value of around 28.5 μmol·s^{-1} are caused by the fact that the electrolyte level control valve (PV1) opens often two times in a row to oppose the level decrease caused by the opening of the pressure control valve (PV2) on the H_2 side. These consecutive openings let higher quantities of H_2 contaminate into the O_2 side. This effect was also depicted in figure 5.10.

Comparing the H_2 molar flow rates through the pipes to these through the separators (figure 5.15), for negligible supersaturation (SF=1) it can be said that these flow rate spikes caused by the response of the valves are quite significant, since can become up to 17 times larger than the same spikes observed for the separators. However, when the valves are closed and the electrolyte is flowing slowly towards the H_2 side, the H_2 crossover is completely affected by the mass transport through the separators. If a higher supersaturation factor is used, the flow rates through the pipes do not change, since the concentration of H_2 inside the corresponding CSTR tank (at the bulk) will still be equal to its solubility (supersaturation was considered to enhance the concentration at the edges of the separators). Consequently, as discussed before, the proportional increase of mass transport through the separators due to higher supersaturation factors will make the effect of H_2 crossover due to mixing less significant.

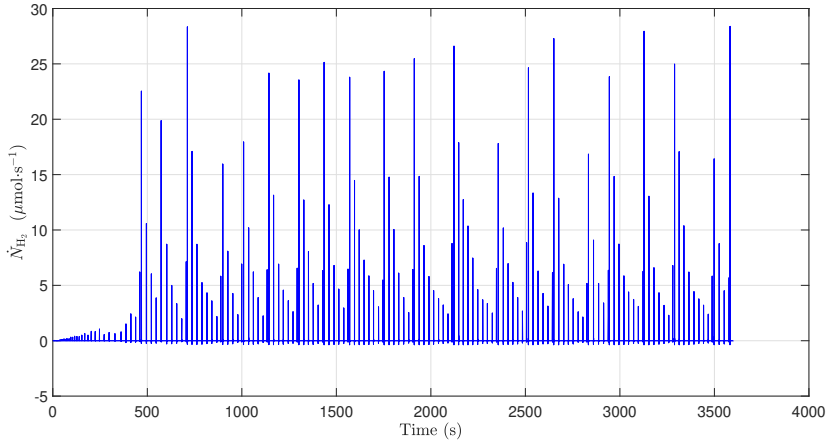

Figure 5.17: Total H_2 molar flow rate that enters the O_2 side (CSTR 1) through elements P1 and Pa1.

On the other hand, figure 5.18 depicts the total O_2 molar flow rate that enters the H_2 side through elements P2 and Pc1. Here, the system startup state can be also clearly seen. O_2 is slowly flowing and entering the opposite side with an small average molar flow rate of 0.01 μmol·s^{-1}. However, this slow movement that happens continuously between the valve openings forces higher O_2 concentrations to elements P2 and Pc1. This fact becomes visible during the main operating state when the pressure control valve (PV2) at the H_2 flash tank opens forcing instantaneous high flow rate spikes that reach a maximum value of 75 μmol·s^{-1}. These observed spikes are higher compared to these of H_2 in figure 5.17 for the reason mentioned above.

Comparing figure 5.18 to the O_2 flow rates entering the H_2 side from the separators (figure 5.16 for SF=1), it is observed that the flow rate spikes through the pipes (P2 and Pc1) can be up to 140 times larger than these of the separators indicating the significance of the mixed electrolyte cycles for the O_2 crossover. However, as shown in figure 5.14, the gaseous O_2 content inside the H_2 flash tank is unlikely to impose a risk for explosive mixture even when a high supersaturation factor is applied.

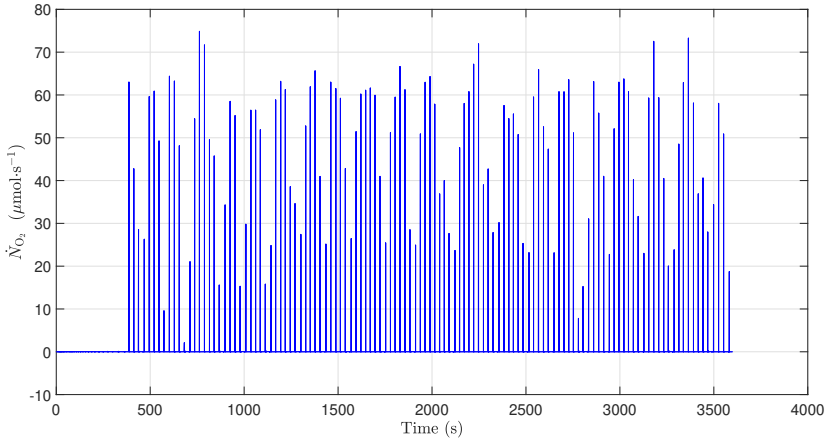

Figure 5.18: Total O_2 molar flow rate that enters the H_2 side (CSTR 2) through elements P2 and Pc1.

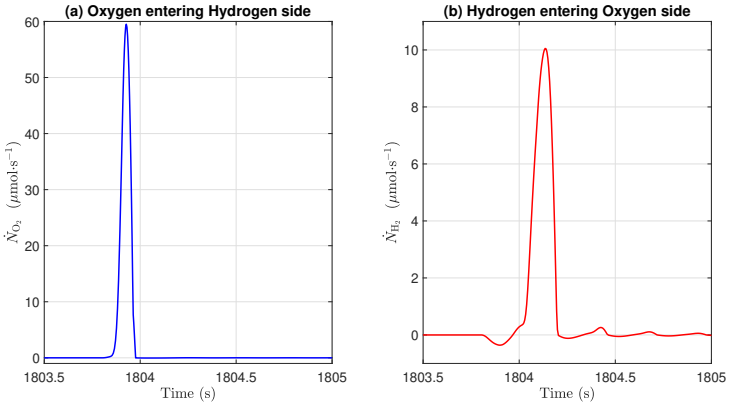

Figure 5.19: Molar flow rates caused by a simultaneous valve operation during the main operating state. (a) depicts the O_2 flow rate that enters the H_2 side (CSTR 2) through elements P2 and Pc1, while (b) depicts the flow rate of H_2 entering the O_2 side (CSTR 1) through P1 and Pa1.

Figure 5.19 depicts the molar flow rates of dissolved O_2 and H_2 that enter the opposite side tank through the pipes, focused on a simultaneous operation of the control valves. Firstly the pressure control valve (PV2) opens forcing the electrolyte to the hydrogen side, which causes an O_2 flow rate spike of 60 μmol·s^{-1}. The consecutive openings of the electrolyte level control valve (PV1) causes higher movement of H_2 to the O_2 side reaching 10 μmol·s^{-1}. As can be seen, the width of the H_2 flow rate spike is larger than that of O_2

indicating the longer PV1 valve opening duration.

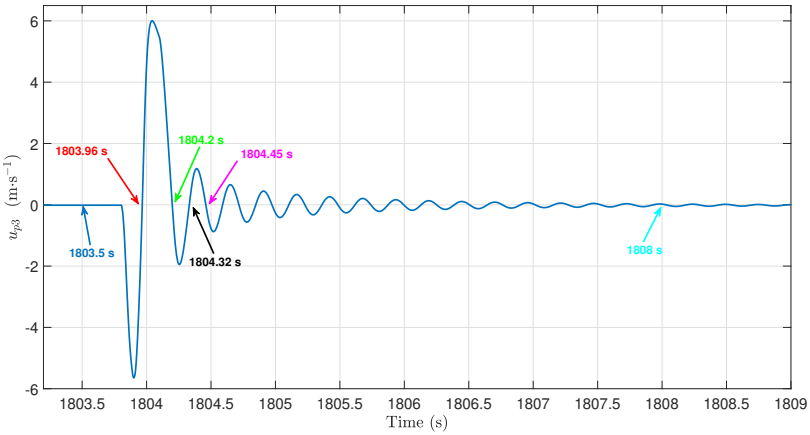

Figure 5.20: Induced velocity profile through the mixing line (element P3) by a simultaneous valve opening.

Figure 5.20 illustrates the flow velocity profile in the mixing line induced by the simultaneous operation of both valves (same time interval as in fig. 5.19). At 1803.5 s, just before the pressure control valve (PV2) opening, the flow velocity is -0.013 m·s^{-1} (direction towards the H_2 side). The positive velocity indicates that the flow is moving towards the O_2 side. The marked time points are used in figure 5.21, which depicts how the O_2 and H_2 spatial concentration profiles in the mixing line are affected by the operation of the valves.

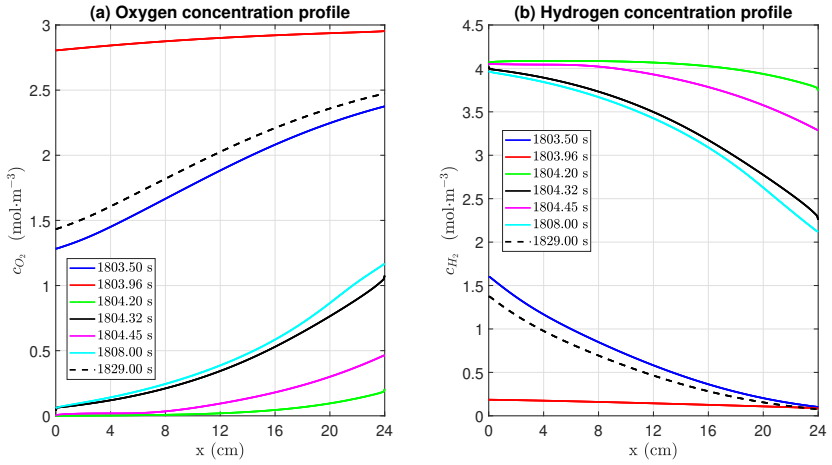

Figure 5.21: Spatial concentration profiles of (a) O_2 and (b) H_2 in the mixing line (P3) at the time points marked in figure 5.20.

The mixing line (element P3) connects the H_2 side ($x = 0$ cm) to the O_2 side ($x = 24$ cm). In figure 5.21, the blue line in (a) and (b) shows the concentration profile of O_2 and H_2 respectively, just before the pressure control valve (PV2) opening. The effect of the PV2

operation is shown by the red line where the flow is forced towards the H_2 side resulting in a higher O_2 presence in the mixing line. The opposite behavior happens when the flow is forced towards the O_2 side by the PV1 valve operation (green line). The black (1804.32 s) and purple (1804.45 s) lines indicate the mass movement caused by the first two oscillations after the closure of PV1, while the light blue line (1808 s) shows the concentrations profile when the oscillations have almost vanished. The dashed black line (1829 s) presents the concentrations just before the next operation of the valves. As can be seen, at that time point, both concentrations are almost equal to these at the previous opening of the valves (1803.5 s - blue lines).

5.3.4. DIFFERENT CURRENT DENSITIES

In this paragraph, the effect of the current density on the crossovers will be investigated. The current density was varied in the range of 500 - 5000 A·m^{-2}, while for consistency in the results and comparison to literature trends, the same supersaturation factor (SF) of 10 was applied for both O_2 and H_2.

Figure 5.22 illustrates the level of gaseous H_2 content in the O_2 flash tank for different operating current densities. The presented contents are the average stabilized values during the main operating state of the system.

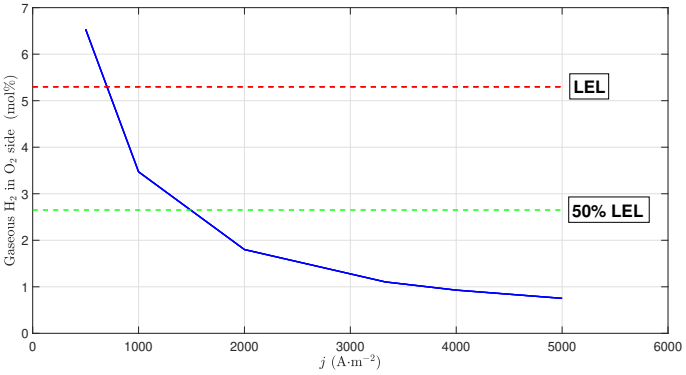

Figure 5.22: Gaseous H_2 content in the O_2 tank as a function of current density and for supersaturation factor SF=10. The lower explosive limit of 5.3 mol% H_2 and the safety limit are also visible.

The main observable trend is that the decrease of current density induces higher H_2 content. This behavior has been experimentally observed in literature [58], [21] and happens because at lower current densities, less O_2 is produced (see table 5.2) to dilute the H_2 that crosses over resulting to higher H_2 content in the O_2 side. Moreover, from the examined current densities, when the system operates at 500 A·m^{-2}, the gaseous mixture in the O_2 flash tank falls into the explosive limits with 6.54 mol% H_2. However, in many industrial applications, a 50% of the lower explosive limit is permitted to be reached for safety reasons and thus the shutdown limit is set to 2.65 %mol H_2 [58]. This means that the examined system can operate safely above 1500 A·m^{-2} for a supersaturation factor of 10. Having a look at table 5.4 where the crossovers for the target current density and increasing supersaturation factors are summarized, it can be seen that from SF=30 and above, the H_2 content falls above the safety limit of 2.65 mol%. Combining this information with the trend shown in figure 5.22, it can be concluded that the supersaturation is

an important phenomenon for the H_2 crossover since at high levels it leads to an explosive mixture posing risk for the safe operation of the system. Also, it will be unsafe to run the system below the target current density if SF>30.

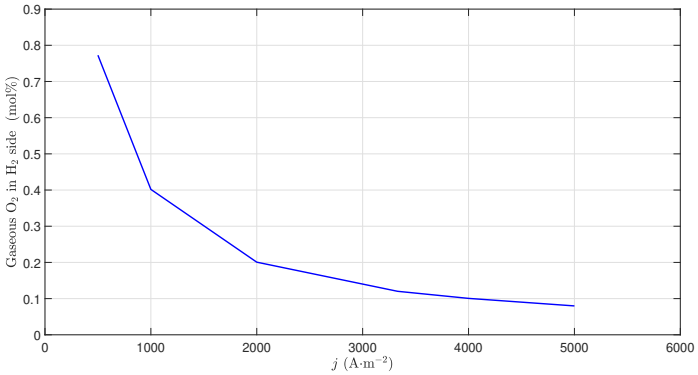

Figure 5.23: Gaseous O_2 content in the H_2 tank as a function of current density and for supersaturation factor SF=10.

A similar trend is observed for the gaseous O_2 content in the H_2 flash tank, which is presented in figure 5.23, but to a much lower extent. Even at low current densities, the H_2 purity remains much higher than the upper explosive limit of 95 mol% H_2 (5 mol% O_2) for a supersaturation factor of 10. But as shown in table 5.4, even with higher supersaturation, an explosive mixture is unlikely to be formed inside the O_2 flash tank. Consequently, O_2 crossover is of minor importance and the contamination of H_2 inside the O_2 side is the dominating phenomenon posing risks for the safe operation of the system as is also discussed in literature [58], [22], [21].

5.4. SUMMARY AND DISCUSSION ON THE MODELS

The main target of this project was to characterize the transient dynamic behavior of the ZEF experimental alkaline electrolysis system and predict the level of gas crossover under the company's specifications. For this scope, two different models were developed.

For the first task, an unsteady hydraulic circuit analysis was applied by treating the system as a network consisting of elements (pipes, flash tanks, half-cell compartments) and nodes. The system is self-pressurized, meaning that it starts operating at atmospheric pressure and the gases that are produced in the stack accumulate inside the closed flash tanks and buffers, increasing gradually the pressure. This pressure increase is faster in the O_2 flash tank since it is designed smaller forcing the electrolyte to the H_2 side. The electrolyte is moving through the network elements due to natural effects because pumps are not used in the system. Two forces are acting on the electrolyte. The first is caused by the differential pressure between the two flash tanks and the second is the buoyancy caused by the evolution of the bubbles inside the half-cells. The effect of buoyancy was neglected to reduce the complexity of the transient model and was assumed that the electrolyte flow is completely affected by the differential pressure between the two sides. Thus the evolving gases were considered to accumulate inside the flash tanks at the same rate that are produced. This assumption is shown in figures 5.8, 5.9, 5.10 with the electrolyte flowing slowly at the opposite direction of the anodic bubbles when the valves are closed and when the H_2 side pressure control valve (PV2) is triggered. Furthermore, the electrolyte flow is

opposing the cathodic bubbles when the level control valve (PV1) opens. As mentioned in the results, during these valve openings the differential pressure can instantly become very high (1.69 bar) causing large electrolyte mass flow rates. At these moments the electrolyte may draw bubbles out of the half-cells (even anodes or cathodes) and lead them through the pipes to the opposite side flash tank enhancing a lot the crossovers if it is considered that the pressure spikes caused by the valves happen in seconds time scale and the system operates in hourly time scale.

The results of the first model, which was developed in Simulink (gas and liquid volumes in the flash tanks/buffers, pipe velocities, pressures in relevant nodes), were used as inputs in the second MATLAB model to predict the level of crossovers induced by the electrolysis system operation. It should be mentioned that the two models are not 'mass conservative'. This means that the models could not run in parallel, so the pressure change that is caused i.e. in O_2 flash tank by the crossed over H_2 (and also O_2 that leaves through the separators) was not part of the first model and the same holds for the H_2 flash tank. According to the aforementioned and taking into account the higher H_2 crossover compared to O_2 (as presented in section 5.3.2), the gas mixture pressure in the O_2 flash tank of the crossovers model is greater than the same pressure of the first model. Similarly, the pressure in the H_2 tank is lower. Furthermore, these differences are larger at higher supersaturation factors since the crossovers are larger. The following table depicts the aforementioned pressure differences between the two models during the main operating state.

Table 5.6: Crossovers model pressure in O_2 and H_2 flash tank compared to the hydraulic circuit model pressures.

Tank	SF=1	SF=10	SF=20	SF=30	SF=40	SF=50
O_2 tank (bar)	+ 0.6	+1.03	+1.48	+1.9	+2.34	+2.76
H_2 tank (bar)	-0.9	-1.1	-1.28	-1.51	-1.71	-1.92

Consequently, under these conditions, the analysis of the crossovers model should be considered preliminary. Even if the crossovers could be implemented in the first model, the result would have been a slightly more often valve opening without significant effects on the dynamics and probably an earlier stabilization of the crossovers curve. So, the model gives an insight into the level of contamination in both flash tanks, the contribution of the mass transfer mechanisms and indicates the importance of supersaturation on the electrodes boundary layer.

5.5. COMPARISON WITH PRELIMINARY EXPERIMENTAL DATA

This section includes a comparison of the thesis results with experimental data from the ZEF bunker twin setup, which was ready for testing at the final stage of the project. Some preliminary data were provided by the company to compare with the predicted results from the models.

The current setup implements a stack of 3 cells and the available experiment was conducted for a current density of 2000 $A \cdot m^{-2}$. For this reason, additional simulations were done to match the geometry aspects of the stack in the experimental setup. The available data for comparison are the measurements of the gas pressure and the opposite side gas content inside the buffers.

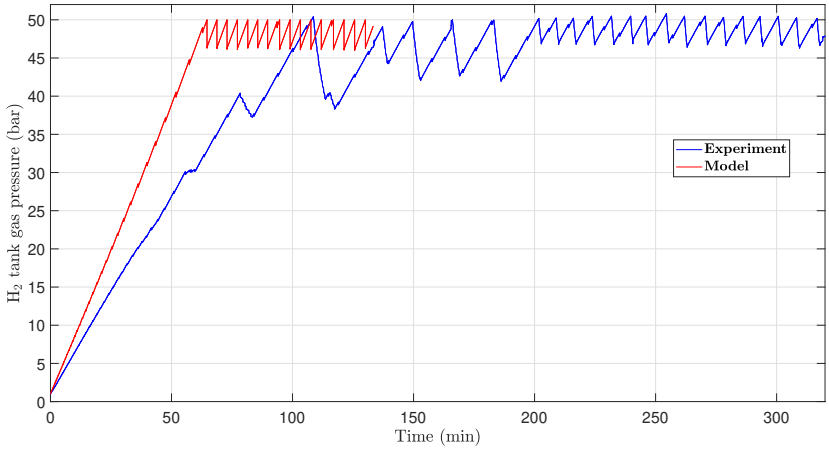

Figure 5.24: A comparison of the gas pressure in the H_2 tank between the model (red line) and the experimental setup (blue line).

Figure 5.24 presents a comparison between the predicted from the model gas pressure response in the H_2 flash tank/buffer and the measured response from the experiment. As can be seen, the model estimates a shorter startup period of around 65 min compared to the experiment where the pressure of 50 bar is reached after 109 min. This was expected since in the model all the produced gas is ideally accumulated in the flash tanks. Moreover, some large pressure drops can be seen in the experimental data both during the startup (when the pressure reaches 30 bar and 40 bar respectively) and the main operating state (between 100 and 200 min). These pressure drops are not part of the normal operation of the system and are caused by the intentional opening of both purging valves at a larger duration than the specified (100 ms) for testing of the gas sensing system. This means that the real startup duration will be at least 10 min shorter. A steady profile of the pressure, which can be compared with the model is reached after 200 min.

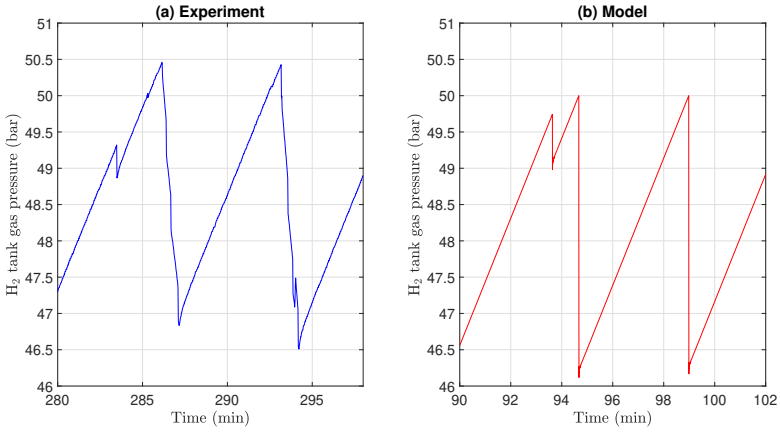

Figure 5.25: A closer view of the H_2 tank pressure drop profile caused by the operation of the valves as measured in the experiment (a) and predicted by the model (b).

Figure 5.25 shows a closer view of the gas pressure profile in the H_2 tank for both experiment and model. As can be seen, the total pressure drop induced by the operation of the valves is almost at the same level with around 3.9 bar measured in the experiment and 3.75 bar predicted by the model. Moreover, the time interval between two consecutive valve openings is 7.1 min in the experiments while a 4.4 min duration is predicted by the model, which is as expected shorter. An oscillatory behavior can not be clearly seen from the experimental data because the sampling time is at the time-scale of seconds (with an average time difference between the samples of 1.16 s) and the predicted amplitudes are in the time-scale of milliseconds. The gas pressure in the O_2 tank has a similar response and the pressure difference between the two tanks fluctuates with an average value of 0.04 bar (higher in the O_2 tank).

A gas purity sensing system is also installed in the buffers of the experimental setup. Figure 5.26 illustrates some measurements taken in the time interval of 230-320 min.

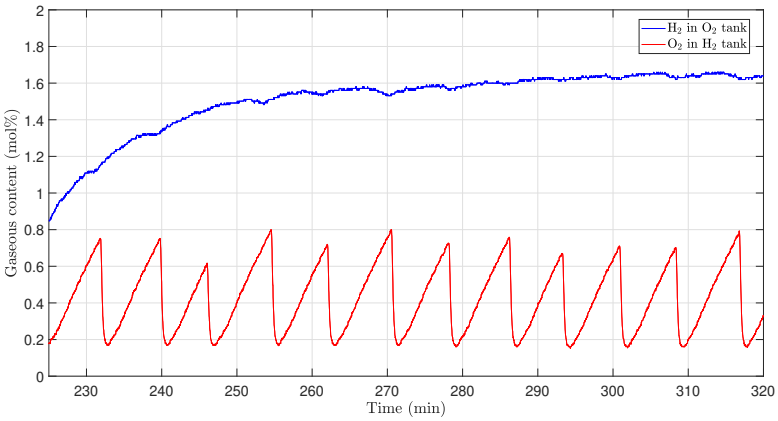

Figure 5.26: Experimental data for the gaseous H_2 and O_2 content in the opposite side tank.

As can be seen in the above figure, the H_2 crossover is higher than that of O_2 and both seem to have reached a stable behavior with an average content of 1.63 mol% and 0.41 mol% respectively.

Table 5.7: Predicted gases content in the opposite side tank for increasing supersaturation factor (SF).

Parameter	SF=1	SF=10	SF=20
H_2 in O_2 (mol%)	0.18	1.68	3.28
O_2 in H_2 (mol%)	0.025	0.18	0.35

Table 5.7 includes the gases stabilized average contents in the opposite side tank for increasing supersaturation factor as are predicted by the model (for 3 cells and 2000 $A \cdot m^{-2}$). Comparing the measured contents to the model predictions, it seems that a possible intensity of supersaturation is between 5 and 15 times higher than the solubility of the components. Moreover, the model probably underestimates the crossover of O_2 and overestimates that of H_2. One possible reason is that more O_2 is forced due to the pressure-driven convection through the separators of the cells when the valves are closed. The experimental setup does not yet implement pressure sensors to the stack for a better insight of the differ-

ential pressure between the anodes and the cathodes. However, the recorded gas pressure difference in the buffers shows larger values than the predictions of the model when the valves are closed and thus, it is possible that a higher pressure in the anodes would enhance the mass transport of O_2 to the cathodes and limit that of H_2 to the anodes.

It should also be mentioned that another factor that has an impact on the crossovers is the operating temperature. The Henry constants that are used in the model are calculated for the target operating temperature of 90 ^{o}C. However, the experimental system does not have insulation yet and the average electrolyte temperature that was recorded is around 35 ^{o}C. The solubility of dissolved gases in electrolyte solutions decreases at higher temperatures [28]. Thus, at 35 ^{o}C more O_2 and H_2 will be dissolved in the aqueous KOH electrolyte enhancing the crossovers.

6

Conclusions

The purpose of this thesis was to characterize the transient dynamic response of the ZEF alkaline electrolysis system and predict the level of gaseous cross-contamination. For this scope, the study was conducted using two models. This chapter summarizes the main conclusions that derive from the analysis of the results.

6.1. Electrolysis system dynamic response

A first simulation was conducted in Simulink for the system operating at the target current density of 3330 $A \cdot m^{-2}$ with a duration of 3600 s. The main observations and conclusions regarding the pressure response are the following:

- The startup, which is the pressure build-up period, lasts around 6.5 min. In the real system, this duration is longer (as observed in the experimental data) since the model assumes that ideally, the evolving gases accumulate in the flash tanks at the same rate that are produced.
- During the startup, only the valve PV1 opens every time the electrolyte level in the O_2 flash tank falls below 59 mm and as the gas pressure increases, it operates less often. The maximum pressure difference induced during the startup is 1.12 bar between the flash tanks and 0.76 bar between the half-cell compartments (stack anodes-cathodes).
- The main operating state is the period when the system has reached the target pressure of 50 bar and both purging valves operate to control the process. The model predicts that both valves open frequently at the same time leading to a total pressure drop of around 4 bar on both sides, with consecutive openings of valve PV1 to effectively control the electrolyte level. At these time intervals, the maximum pressure difference between the gases in the flash tanks reaches 1.69 bar, while a 1.137 bar pressure gradient is estimated between the half-cells.
- When the control valves are closed and the flow is moving slowly inside the stack and the pipes, the differential pressure between the half-cells is balanced and slightly higher in the anodes.
- It is observed that the gas pressure response right after the closure of the valves in the O_2 side is more oscillatory with higher maximum amplitude compared to the

gas pressure response in the H_2 side. Furthermore, the oscillations are completely damped after an average time interval of 4 s. In the real system, a higher damping effect is expected if it is taken into consideration that the exact geometry of the stack was not implemented and also a simpler model for the friction estimation was used, where the instantaneous flow acceleration contribution on the friction was neglected.

- The differential pressure spikes caused by the operation of the control valves are identified as the main problem threatening the integrity of the system. The high-pressure difference in combination with the oscillating response right after the valves closure may damage the separators of the cells and increase the risk of rupture. In that case, the anodic solutions will mix with the cathodic increasing dramatically the cross-contamination of both sides leading the whole system to fail.

The predicted pressure response from the model was also compared to preliminary experimental data for a stack of 3 cells operating at the current density of 2000 $A \cdot m^{-2}$. The model under-predicts the startup period as expected. The pressure drop induced by the operation of the valves shows good agreement with the experiment. A conclusion for the oscillatory behavior can not be made since the sampling period was longer than the time-scale observed in the model.

Regarding the electrolyte flow in the system, the following observations and conclusions are made:

- When the valves are closed, the electrolyte moves slowly towards the H_2 side with the flow been counter-current to the direction of the evolving bubbles in the anodes and the same happens also when the pressure control valve (PV2) opens and the flow is forced faster to the H_2 side.

- A similar back-flow response that opposes the bubbles evolution direction is observed at the cathodes when the electrolyte level control valve (PV1) operates.

- The predicted electrolyte back-flow through the anodes when the valves are closed may not be valid since the effect of the emerged bubble swarm on the flow was not modeled. However, the operation of the control valves can cause such back-flows in both half-cell compartments leading the bubbles out of the stack from its bottom channels. Consequently, it is possible that some bubbles can end up through the pipes to the opposite side enhancing the crossovers.

The response of the electrolysis system was also simulated for different current densities in a range 500-5000 $A \cdot m^{-2}$. The gas evolution rate increases in higher current densities affecting both the startup duration and the frequency of valve opening. Consequently, at lower current densities, the startup period is longer and the valves operate less often since the pressure build-up is slower. The induced pressure and electrolyte level fluctuations due to the operation of the valves are predicted to be at the same level independently of the current density.

6.2. CROSSOVERS

The crossovers model was developed using MATLAB to examine how the induced flow and pressure response affects the mass transport of dissolved O_2 and H_2 to the opposite side both through the separators of the half-cell compartments and the mixing line. The examined physical mass transport mechanisms were diffusion and pressure-driven convection. In addition to these, the effect of the local electrolyte supersaturation phenomenon was quantitatively taken into consideration with the form of an enhancement factor applied

to the separator boundaries (for O_2 in the anodes and H_2 in the cathodes). Furthermore, the induced crossover contents were examined concerning the explosive limits as are defined in literature for the company's operating conditions (pressure and temperature) and according to the shutdown safety margins (50% of LEL and UEL).

The following observations and conclusions are made for the crossovers when the electrolyzer operates at the target current density:

- The crossovers of both electrolysis gases are gradually increasing during the startup period and finally reach a stable average value during the main operating state. In the absence of supersaturation (SF=1), the gaseous H_2 impurity in the O_2 side is estimated 0.1154 mol%, while that of O_2 in H_2 side is 0.0169 mol% without the formation of explosive mixtures.

- An increase of the supersaturation factor by 10 leads to almost 1% and 0.1% higher H_2 and O_2 crossovers respectively. Thus, this indicates that the effect of the oversaturated concentration of the dissolved gases in the electrode boundary layer, which is in contact with the separator in the case of the zero-gap configuration, has a strong effect mainly on the H_2 crossover. At even higher supersaturation factors (SF>30), the gaseous mixture in the O_2 tank falls above the industrial safety limit of 2.65 mol% H_2 indicating the need for shutdown. On the other hand, the mixture in the H_2 tank does not pose a risk since the O_2 content remains below 1%.

- A more general conclusion is that the frequent operation of the valves keeps the crossovers limited since when they open, part of the impurities is also thrown out of the system. The high operating pressure of 50 bar and the mixing electrolyte cycles strategy do not seem to have the same level of effect on the crossovers as is observed in other studies in literature (i.e. Trinke [58] measured experimentally a H_2 impurity of 2.9 mol% at 10 bar pressure, 3000 $A{\cdot}m^{-2}$ and mixing cycles strategy). This difference is attributed to the operation of the valves.

The crossovers were also estimated for different current densities, using a supersaturation factor of 10. The model qualitatively predicted a similar to other experimental works ([58], [22]) behavior with higher cross-contamination in lower current densities limiting the safe operational window above 1500 $A{\cdot}m^{-2}$. In a larger intensity of supersaturation, the minimum safe current density is expected to be higher.

A comparison of the model results with the experimental data indicates that the supersaturation intensity is between 5 and 15 times higher than the solubility for both electrolysis gases. Moreover, it is concluded that the model predicts lower O_2 and higher H_2 crossovers, probably due to the underestimation of the differential pressure between the half-cell compartments. However, considering the model simplifications, the predicted crossovers are very close to the preliminary experimental data showing that system can safely run above 2000 $A{\cdot}m^{-2}$.

7

RECOMMENDATIONS

This final chapter provides recommendations to upgrade and extend the developed models and some advice on possible system modifications and experimental work to minimize the observed problems and identify safety risks.

7.1. MODELING

- The first model that predicts the system's dynamic response does not take into account the buoyancy effect of the rising bubbles, assuming incompressible flow in all the elements of the network and ideal bubble accumulation in the flash tanks. An update of the model is recommended to account also for the bubbly flow in the relevant elements (stack half-cells and pipes leading the bubbles to the flash tanks) and examine at what level the already predicted flow response will be affected.

- In this work, the temperature was assumed to be constant at 90 ^{o}C, which is the company's target operating point. However, in the real system, the temperature will present variations through the different elements. Thus, the developed models can be extended by adding a temperature network to predict how the produced at electrodes heat is transferred in the system, how the temperature at relevant points changes and how these variations affect the crossovers since the solubility of dissolved gases increases in lower temperatures.

- The continuous stirred tank reactor (CSTR) approach that was followed in the crossovers model can be altered by adopting a different method (i.e. plug flow reactor or CSTR in series) to take into account the local mass transfer between the supersaturated electrode and electrolyte bulk.

7.2. SYSTEM MODIFICATIONS

The main threat to the system integrity was identified to be the high differential pressure between the half-cell compartments, which reaches its highest value when both valves operate simultaneously during the main operating state. It is recommended to alter the valve opening strategy (during the main operating state) as follows:

- Do not operate the two valves simultaneously.

- Decrease the pressure control valve (PV2) opening duration.

- After the closure of valve PV2, wait some seconds (so the oscillating behavior will be damped) before the electrolyte level control valve (PV1) opens.
- Open the electrolyte level control valve with increased duration.

The aforementioned strategy will probably reduce the maximum differential pressure spikes but not largely since it is shown that a single valve opening causes a maximum pressure gradient of 0.76 bar. Another recommendation is to add properly sized capillary tubes on the downstream side of the valves and increase the opening duration to the time-scale of seconds. This modification will decrease the flow coefficient and smooth out the gas flow that is purged out of the electrolysis system.

7.3. EXPERIMENTS

The experimental system (bunker twin) that was modeled in this project, is at the first stages of operation at the time being. It is recommended to run multiple and long time experiments at different current densities to observe and evaluate its dynamic response, monitor continuously the gas purity at the buffers and examine the long term cross contamination. According to the findings of this work, the following experiments are recommended:

- Use a velocimetry device to evaluate the induced flow velocity and direction when the purging valves operate.
- Install more pressure sensors in the setup to be able to monitor the pressure closer to the stack and estimate experimentally the induced differential pressure between the anodes-cathodes.
- Reduce the pressure sampling time to the milliseconds scale to evaluate the induced oscillatory behavior from the operation of the valves.
- Observe through the transparent stack the bubble behavior when the valves operate and examine if bubbles are dragged out by the flow at the bottom channel in cases of electrolyte back-flow.

Bibliography

[1] Agfa zirfon perl utp 500. https://www.agfa.com/specialty-products/solutions/membranes/zirfon/.

[2] Asco engineering information: Flow data, flow factor and orifice size. https://www.asconumatics.eu/images/site/upload/_en/pdf1/00011gb.pdf.

[3] Matlab 2020 documentation. http://mathworks.com.

[4] Zero emission fuels webpage. http://zeroemissionfuels.com.

[5] Tasneem Abbasi and S.A. Abbasi. 'renewable' hydrogen: Prospects and challenges. *Renewable and Sustainable Energy Reviews*, 15(6):3034 – 3040, 2011.

[6] Z. Abdin, C.J. Webb, and E.MacA. Gray. Modelling and simulation of an alkaline electrolyser cell. *Energy*, 138:316 – 331, 2017.

[7] David Apsley. Unsteady flow in pipes. University of Manchester, 2013. MACE20041: Hydraulics 2, Lecture notes T5.

[8] Sandor Balog, Dominic A. Urban, Ana M. Milosevic, Federica Crippa, Barbara Rothen-Rutishauser, and Alke Petri-Fink. Taylor dispersion of nanoparticles. *Journal of Nanoparticle Research*, 19(8):287, 2017.

[9] Anton Bergant, Angus Ross Simpson, and John Vìtkovsk[ygrave]. Developments in unsteady pipe flow friction modelling. *Journal of Hydraulic Research*, 39(3):249–257, 2001.

[10] Sedat Biringen. A note on the numerical stability of the convection-diffusion equation. *Journal of Computational and Applied Mathematics*, 7(1):17 – 20, 1981.

[11] Jörn Brauns and Thomas Turek. Alkaline water electrolysis powered by renewable energy: A review. *Processes*, 8(2):248, Feb 2020.

[12] Greig Chisholm and Leroy Cronin. Chapter 16 - hydrogen from water electrolysis. In Trevor M. Letcher, editor, *Storing Energy*, pages 315 – 343. Elsevier, Oxford, 2016.

[13] S. W. Churchill. Fricton-factor equation spans all fluid-flow regimes. *Chemical Engineering*, 1977.

[14] George W. Crabtree, Mildred S. Dresselhaus, and Michelle V. Buchanan. The Hydrogen Economy. *Physics Today*, 57(12):39–44, dec 2004.

[15] Martín David, Hernán Alvarez, Carlos Ocampo-Martinez, and Ricardo Sánchez-Peña. Dynamic modelling of alkaline self-pressurized electrolyzers: a phenomenological-based semiphysical approach. *International Journal of Hydrogen Energy*, 45(43):22394 – 22407, 2020.

[16] Martín David, Carlos Ocampo-Martínez, and Ricardo Sánchez-Peña. Advances in alkaline water electrolyzers: A review. *Journal of Energy Storage*, 23:392 – 403, 2019.

[17] R.M. de Jonge, E. Barendrecht, L.J.J. Janssen, and S.J.D. van Stralen. Gas bubble behaviour and electrolyte resistance during water electrolysis. *International Journal of Hydrogen Energy*, 7(11):883 – 894, 1982.

[18] Ibrahim Dincer and Canan Acar. Review and evaluation of hydrogen production methods for better sustainability. *International Journal of Hydrogen Energy*, 40(34):11094 – 11111, 2015.

[19] J. Eigeldinger and H. Vogt. The bubble coverage of gas-evolving electrodes in a flowing electrolyte. *Electrochimica Acta*, 45(27):4449 – 4456, 2000.

[20] Philipp Haug. *Experimental and theoretical investigation of gas purity in alkaline water electrolysis*. PhD thesis, Mar 2019.

[21] Philipp Haug, Matthias Koj, and Thomas Turek. Influence of process conditions on gas purity in alkaline water electrolysis. *International Journal of Hydrogen Energy*, 42(15):9406 – 9418, 2017.

[22] Philipp Haug, Bjarne Kreitz, Matthias Koj, and Thomas Turek. Process modelling of an alkaline water electrolyzer. *International Journal of Hydrogen Energy*, 42(24):15689 – 15707, 2017.

[23] J.W. Haverkort. Modeling and experiments of binary electrolytes in the presence of diffusion, migration, and electro-osmotic flow. *Phys. Rev. Applied*, 14:044047, Oct 2020.

[24] Michael Hoel and Snorre Kverndokk. Depletion of fossil fuels and the impacts of global warming. *Resource and Energy Economics*, 18(2):115–136, 1996.

[25] Marijke Huysmans and Alain Dassargues. Review of the use of péclet numbers to determine the relative importance of advection and diffusion in low permeability environments. *Hydrogeology Journal*, 13(5):895–904, 2005.

[26] H Janssen, J.C Bringmann, B Emonts, and V Schroeder. Safety-related studies on hydrogen production in high-pressure electrolysers. *International Journal of Hydrogen Energy*, 29(7):759 – 770, 2004.

[27] L. J. J. Janssen and E. Barendrecht. Mass transfer at gas evolving electrodes. *Journal of Applied Electrochemistry*, 15(4):549–555, 1985.

[28] M Bo Knaster and LA Apelbaum. Solubility of hydrogen and oxygen in concentrated potassium hydroxide solutions. *Russ J Phys*, 38(1):223–225, 1964.

[29] Subramani Krishnan, Matthew Fairlie, Philipp Andres, Thijs de Groot, and Gert Jan Kramer. Chapter 10 - power to gas (h2): alkaline electrolysis. In Martin Junginger and Atse Louwen, editors, *Technological Learning in the Transition to a Low-Carbon Energy System*, pages 165 – 187. Academic Press, 2020.

[30] Henryk Kudela. Hydraulic losses in pipes. *Wroclaw University of Science*, 2012.

[31] N. Kumar and N. Khanduja. Mathematical modelling and simulation of cstr using mit rule. In *2012 IEEE 5th India International Conference on Power Electronics (IICPE)*, pages 1–5, 2012.

[32] Pijush K. Kundu, Ira M. Cohen, and David R. Dowling. Chapter 4 - conservation laws. In Pijush K. Kundu, Ira M. Cohen, and David R. Dowling, editors, *Fluid Mechanics (Sixth Edition)*, pages 109 – 193. Academic Press, Boston, sixth edition edition, 2016.

[33] Hans Petter Langtangen and Svein Linge. *Finite Difference Computing with PDEs: A Modern Software Approach*. Springer Publishing Company, Incorporated, 1st edition, 2017.

[34] Damien Le Bideau, Philippe Mandin, Mohamed Benbouzid, Myeongsub Kim, and Mathieu Sellier. Review of necessary thermophysical properties and their sensivities with temperature and electrolyte mass fractions for alkaline water electrolysis multiphysics modelling. *International Journal of Hydrogen Energy*, 44(10):4553 – 4569, 2019.

[35] R.L. LeRoy and A.K. Stuart. Advanced unipolar electrolysis. *International Journal of Hydrogen Energy*, 6(6):589 – 599, 1981.

[36] Juan Sebastian Lopez-Echeverry, Simon Reif-Acherman, and Eduard Araujo-Lopez. Peng-robinson equation of state: 40 years through cubics. *Fluid Phase Equilibria*, 447:39 – 71, 2017.

[37] Bruce R Munson, Donald F Young, Theodore H Okiishi, and Wade W Huebsch. Fundamentals of fluid mechanics, john wiley & sons. *Inc., USA*, 2006.

[38] Reyhaneh Norooz, Hamid Shamloo, and Maryam Mousavıfard. A review of one-dimensional unsteady friction models for transient pipe flow. *Cumhuriyet Üniversitesi Fen Edebiyat Fakültesi Fen Bilimleri Dergisi*, 36:2278 – 2288, 2015.

[39] Turkuler Ozgumus, Moghtada Mobedi, and Unver Ozkol. Determination of kozeny constant based on porosity and pore to throat size ratio in porous medium with rectangular rods. *Engineering Applications of Computational Fluid Mechanics*, 8(2):308–318, January 2014.

[40] Robert Phillips and Charles W. Dunnill. Zero gap alkaline electrolysis cell design for renewable energy storage as hydrogen gas. *RSC Adv.*, 6:100643–100651, 2016.

[41] Amitava Roy, Simon Watson, and David Infield. Comparison of electrical energy efficiency of atmospheric and high-pressure electrolysers. *International Journal of Hydrogen Energy*, 31(14):1964 – 1979, 2006.

[42] Viswanathan Saji. *Molybdenum-Based Electrocatalysts for Hydrogen Generation by Water Electrolysis*, pages 43–56. 08 2014.

[43] F. J. Salzano, G. Skaperdas, and A. Mezzina. Water vapor electrolysis at high temperature: Systems considerations and benefits. *International Journal of Hydrogen Energy*, 10(12):801–809, 1985.

[44] Diogo M. F. Santos, Cesar A. C. Sequeira, and Jose L. Figueiredo. Hydrogen production by alkaline water electrolysis. *Química Nova*, 36:1176 – 1193, 00 2013.

[45] Maximilian Schalenbach, Wiebke Lueke, and Detlef Stolten. Hydrogen diffusivity and electrolyte permeability of the zirfon PERL separator for alkaline water electrolysis. *Journal of The Electrochemical Society*, 163(14):F1480–F1488, 2016.

[46] Maximilian Schalenbach, Geert Tjarks, Marcelo Carmo, Wiebke Lueke, Martin Mueller, and Detlef Stolten. Acidic or alkaline? towards a new perspective on the efficiency of water electrolysis. *Journal of The Electrochemical Society*, 163(11):F3197–F3208, 2016.

[47] V. Schröder, B. Emonts, H. Janßen, and H.-P. Schulze. Explosion limits of hydrogen/oxygen mixtures at initial pressures up to 200 bar. *Chemical Engineering & Technology*, 27(8):847–851, 2004.

[48] C. A. C. Sequeira, D. M. F. Santos, B. Šljukić, and L. Amaral. Physics of electrolytic gas evolution. *Brazilian Journal of Physics*, 43(3):199–208, 2013.

[49] Süha Sevük. Steady and unsteady flow simulation in pipe networks. *Advances in Engineering Software (1978)*, 1(3):107–113, 1979.

[50] Shigeo Shibata. The concentration of molecular hydrogen on the platinum cathode. *Bulletin of the Chemical Society of Japan*, 36(1):53–57, 1963.

[51] H.B Suffredini, J.L Cerne, F.C Crnkovic, S.A.S Machado, and L.A Avaca. Recent developments in electrode materials for water electrolysis. *International Journal of Hydrogen Energy*, 25(5):415 – 423, 2000.

[52] Mónica Sánchez, Ernesto Amores, Lourdes Rodríguez, and Carmen Clemente-Jul. Semi-empirical model and experimental validation for the performance evaluation of a 15 kw alkaline water electrolyzer. *International Journal of Hydrogen Energy*, 43(45):20332 – 20345, 2018.

[53] Geoffrey Ingram Taylor. Dispersion of soluble matter in solvent flowing slowly through a tube. *Proceedings of the Royal Society of London. Series A. Mathematical and Physical Sciences*, 219(1137):186–203, 1953.

[54] Geoffrey Ingram Taylor. The dispersion of matter in turbulent flow through a pipe. *Proceedings of the Royal Society of London. Series A. Mathematical and Physical Sciences*, 223(1155):446–468, 1954.

[55] Min J. Tham, Robert Dixon Walker, and Keith E. Gubbins. Diffusion of oxygen and hydrogen in aqueous potassium hydroxide solutions. *J. Phys. Chem.*, 74(8):1747–1751, April 1970.

[56] Llewellyn Thomas. Elliptic problems in linear differential equations over a network: Watson scientific computing laboratory. *Columbia Univ., NY*, 1949.

[57] Bernhard Tjaden, Samuel J Cooper, Daniel JL Brett, Denis Kramer, and Paul R Shearing. On the origin and application of the bruggeman correlation for analysing transport phenomena in electrochemical systems. *Current Opinion in Chemical Engineering*, 12:44 – 51, 2016. Nanotechnology / Separation Engineering.

[58] P. Trinke, P. Haug, J. Brauns, B. Bensmann, R. Hanke-Rauschenbach, and T. Turek. Hydrogen crossover in PEM and alkaline water electrolysis: Mechanisms, direct comparison and mitigation strategies. *Journal of The Electrochemical Society*, 165(7):F502–F513, 2018.

[59] H. Vogt. The rate of gas evolution of electrodes—i. an estimate of the efficiency of gas evolution from the supersaturation of electrolyte adjacent to a gas-evolving electrode. *Electrochimica Acta*, 29(2):167 – 173, 1984.

[60] H. Vogt. Mechanisms of mass transfer of dissolved gas from a gas-evolving electrode and their effect on mass transfer coefficient and concentration overpotential. *Journal of Applied Electrochemistry*, 19(5):713–719, 1989.

[61] H. Vogt. The concentration overpotential of gas evolving electrodes as a multiple problem of mass transfer. *Journal of The Electrochemical Society*, 137:1179–1184, 1990.

[62] Dianne Wiley and Gustavo Fimbres Weihs. *Electroosmotic Drag in Membranes*, pages 653–654. Springer Berlin Heidelberg, Berlin, Heidelberg, 2016.

[63] Kai Zeng and Dongke Zhang. Recent progress in alkaline water electrolysis for hydrogen production and applications. *Progress in Energy and Combustion Science*, 36(3):307 – 326, 2010.

[64] Bahman Zohuri. *The Chemical Element Hydrogen*, pages 1–35. Springer International Publishing, Cham, 2019.

[65] E. Zoulias, Elli Varkaraki, N. Lymberopoulos, Chris Christodoulou, and George Karagiorgis. A review on water electrolysis. *TCJST*, 4:41–71, 01 2004.

[66] Øystein Ulleberg. Modeling of advanced alkaline electrolyzers: a system simulation approach. *International Journal of Hydrogen Energy*, 28(1):21 – 33, 2003.

Appendices

A

HYDRAULIC CIRCUIT MODEL

A.1. FLASH TANKS EQUATIONS DERIVATION

The mass and momentum conservation for both flash tanks were derived using a deforming control volume which follows the movement of liquid electrolyte on the y-direction (moving upper surface) and is fixed on the x-direction. The integral forms of the unsteady mass and momentum equations are listed below [32].

MASS CONSERVATION

$$\frac{\partial}{\partial t}\int_V \rho \cdot dV + \int_S \rho \cdot (\vec{u}_r \bullet \hat{n}) \cdot dA = 0 \tag{A.1}$$

In the above equation, the first term with the volume integral refers to the rate of mass change inside the control volume V, while the second term is the net mass flow rate through the control surface S. Moreover, $\hat{n}$ is the unit vector pointing out of a control surface S.

MOMENTUM CONSERVATION

$$\frac{\partial}{\partial t}\int_V \rho \cdot \vec{u} \cdot dV + \int_S \rho \cdot \vec{u} \cdot (\vec{u}_r \bullet \hat{n}) \cdot dA = \int_S -P \cdot \hat{n} \cdot dA + \vec{F}_{\text{viscous}} + \int_V \rho \cdot \vec{g} \cdot dV \tag{A.2}$$

The above equation is an expression of Newton's second law in integral form. On the LHS, the first term is the rate of momentum change inside the control volume V and the second term is the rate of momentum flow through the control surface S. The RHS includes the sum of forces, which are categorized in surface and body forces. The surface forces include the pressure (first term) and the viscous contribution (second term), while the body force acted is the gravity (for this system).

In mass and momentum equations, $\vec{u}_r$ is the fluid velocity relative to the control surface, with:

$$\vec{u}_r = \vec{u} - \vec{u}_S \tag{A.3}$$

where $\vec{u}_S$ is the control surface velocity and $\vec{u}$ is the fluid velocity as observed in an inertial frame of reference.

A.1.1. OXYGEN FLASH TANK (T1)

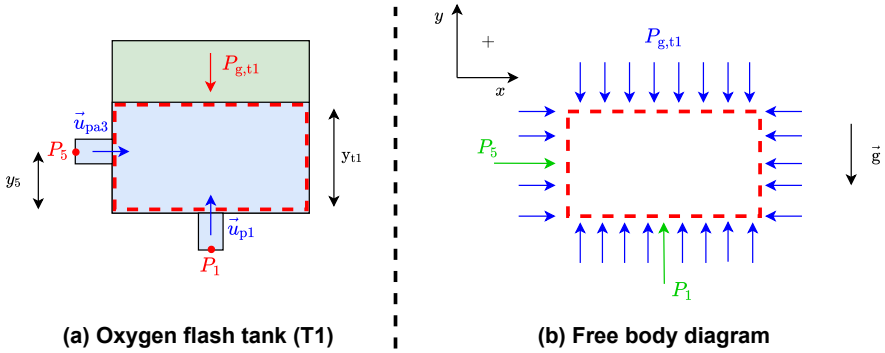

Figure A.1: (a) O_2 flash tank with liquid electrolyte deforming control volume and (b) control volume free body diagram showing pressures on the surfaces.

Figure A.1 depicts the deforming control volume (red dashed line) that was selected to derive the equations for the O_2 flash tank. The control volume includes and follows the movement of the liquid electrolyte. This means that only the upper surface, which is in contact with the accumulated gas, can move in the y direction and so the relative velocity there is zero according to equation A.3. Using equation A.1, the mass conservation reads (under the assumption of incompressible flow):

$$\frac{\partial}{\partial t}\left(\rho \cdot A_t \cdot y_{t1}\right) - \rho \cdot A_p \cdot u_{p1} - \rho \cdot A_p \cdot u_{pa3} = 0 \rightarrow$$

$$A_t \cdot \dot{y}_{t1} = A_p \cdot \left(u_{p1} + u_{pa3}\right) \tag{A.4}$$

where A_t and A_p are the flash tank and connected pipes cross section areas respectively.

The momentum equation for the examined control volume is split in the two directions. Firstly, each term will be separately presented (in vector form). The unsteady term reads:

$$\frac{\partial}{\partial t}\int_V \rho \vec{u} dV = \frac{\partial}{\partial t}\left[\rho \cdot A_t \cdot y_{t1} \cdot \begin{pmatrix} 0 \\ \dot{y}_{t1} \end{pmatrix}\right] = \begin{pmatrix} 0 \\ \rho \cdot A_t \cdot y_{t1} \cdot \ddot{y}_{t1} + \rho \cdot A_t \cdot \dot{y}_{t1}^2 \end{pmatrix} \tag{A.5}$$

The rate of momentum flow through the control surface reads:

$$\int_A \rho \vec{u}\left(\vec{u}_r \bullet \hat{n}\right) dA = \rho \cdot A_p \cdot \begin{pmatrix} 0 \\ u_{p1} \end{pmatrix} \cdot \left[\begin{pmatrix} 0 \\ u_{p1} \end{pmatrix} \bullet \begin{pmatrix} 0 \\ -1 \end{pmatrix}\right] + \rho \cdot A_p \cdot \begin{pmatrix} u_{pa3} \\ 0 \end{pmatrix} \cdot \left[\begin{pmatrix} u_{pa3} \\ 0 \end{pmatrix} \bullet \begin{pmatrix} -1 \\ 0 \end{pmatrix}\right] = \begin{pmatrix} -\rho \cdot A_p \cdot u_{pa3}^2 \\ -\rho \cdot A_p \cdot u_{p1}^2 \end{pmatrix} \tag{A.6}$$

The pressure contribution of the surface forces reads:

$$\int_A -P \bullet \hat{n} dA = -P_1 \cdot A_p \cdot \begin{pmatrix} 0 \\ -1 \end{pmatrix} - P_{g,t1} \cdot A_t \cdot \begin{pmatrix} 0 \\ 1 \end{pmatrix} - \left(P_{g,t1} + \rho \cdot g \cdot y_{t1}\right) \cdot \left(A_t - A_p\right) \cdot \begin{pmatrix} 0 \\ -1 \end{pmatrix} - P_5 \cdot A_p \cdot \begin{pmatrix} -1 \\ 0 \end{pmatrix} - \left[P_{g,t1} + \rho \cdot g \cdot \left(y_{t1} - y_5\right)\right] \cdot A_p \cdot \begin{pmatrix} 1 \\ 0 \end{pmatrix} = \begin{pmatrix} \left(P_5 - P_{g,t1}\right) \cdot A_p - \rho \cdot g \cdot \left(y_{t1} - y_5\right) \cdot A_p \\ \left(P_1 - P_{g,t1}\right) \cdot A_p + \rho \cdot g \cdot y_{t1} \cdot \left(A_t - A_p\right) \end{pmatrix} \tag{A.7}$$

The body force (liquid electrolyte weight) has the following form:

$$\int_V \rho \cdot \vec{g} \cdot dV = \rho \cdot A_t \cdot y_{t1} \cdot \begin{pmatrix} 0 \\ -g \end{pmatrix} \tag{A.8}$$

The viscous force is assumed to have an effect on the y direction (where the electrolyte mainly flows in the flash tank) and was calculated with the same way as in the pipe elements (eq. 4.12). In vector form, it reads:

$$\vec{F}_{\text{viscous}} = \begin{pmatrix} 0 \\ -\lambda_{D.t1} \cdot \frac{\rho \cdot y_{t1} \cdot A_t}{2 \cdot d_t} \cdot \dot{y}_{t1} \cdot |\dot{y}_{t1}| \end{pmatrix} \tag{A.9}$$

Having written all the terms of the momentum equation for the deforming control volume, the final equations for the two directions are presented below.

y DIRECTION:

$$\rho \cdot A_t \cdot y_{t1} \cdot \ddot{y}_{t1} + \rho \cdot A_t \cdot \dot{y}_{t1}^2 - \rho \cdot A_p \cdot u_{p1}^2 = (P_1 - P_{g,t1}) \cdot A_p - \rho \cdot g \cdot A_p \cdot y_{t1} - \lambda_{D,t1} \cdot \frac{\rho \cdot y_{t1} \cdot A_t}{2 \cdot d_t} \cdot \dot{y}_{t1} \cdot |\dot{y}_{t1}| \tag{A.10}$$

x DIRECTION:

$$-\rho \cdot A_p \cdot u_{pa3}^2 = (P_5 - P_{g,t1}) \cdot A_p - \rho \cdot g \cdot (y_{t1} - y_5) \cdot A_p \tag{A.11}$$

A.1.2. HYDROGEN FLASH TANK (T2)

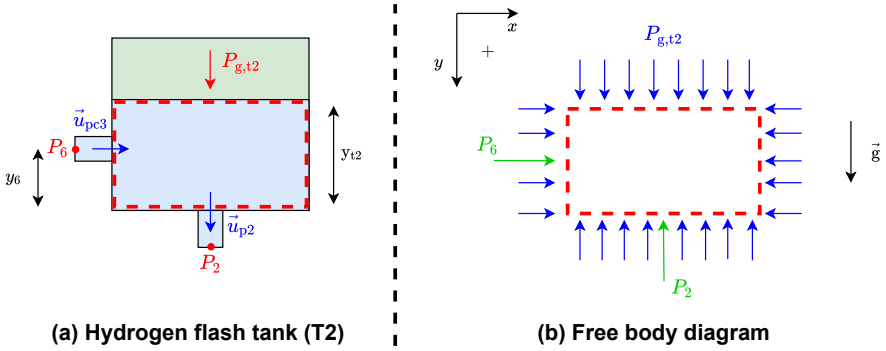

Figure A.2: (a) H_2 flash tank with liquid electrolyte deforming control volume and (b) control volume free body diagram showing pressures on the surfaces.

For the H_2 flash tank, a similar control volume with a deforming upper surface was selected. The coordinates system is in agreement with that of the O_2 tank. The equations derivation was carried out in the same way. The mass conservation reads:

$$A_t \cdot \dot{y}_{t2} = A_p \cdot (u_{pc3} - u_{p2}) \tag{A.12}$$

The momentum conservation has the following form in the two directions:

y DIRECTION:

$$\rho \cdot A_t \cdot y_{t2} \cdot \ddot{y}_{t2} + \rho \cdot A_t \cdot \dot{y}_{t2}^2 + \rho \cdot A_p \cdot u_{p2}^2 = (P_{g,t2} - P_2) \cdot A_p + \rho \cdot g \cdot A_p \cdot y_{t2} - \lambda_{D,t2} \cdot \frac{\rho \cdot y_{t2} \cdot A_t}{2 \cdot d_t} \cdot \dot{y}_{t2} \cdot |\dot{y}_{t2}| \tag{A.13}$$

x DIRECTION:

$$-\rho \cdot A_{\mathrm{p}} \cdot u_{\mathrm{pc3}}^2 = \left(P_6 - P_{\mathrm{g,t2}}\right) \cdot A_{\mathrm{p}} - \rho \cdot \mathrm{g} \cdot \left(y_{\mathrm{t2}} - y_6\right) \cdot A_{\mathrm{p}} \tag{A.14}$$

A.2. MATHEMATICAL MODEL EQUATIONS

In this section, the set of equations of the developed mathematical model are summarized. The two flash tanks have the same cross-section area A_{t} and the same diameter d_{t}. All the pipe elements have the same cross-section area A_{p} and diameter d_{p}, except for elements Pa2 & Pc2 (representing anodes and cathodes respectively).

Table A.1: Mass and momentum conservation equations for the corresponding elements and nodes as presented in figure 4.1.

#	Equation	Element/node
1	$A_{\mathrm{t}} \cdot \dot{y}_{\mathrm{t1}} = A_{\mathrm{p}} \cdot \left(u_{\mathrm{p1}} + u_{\mathrm{pa3}}\right)$	T1-liquid
2	$A_{\mathrm{t}} \cdot \ddot{y}_{\mathrm{t1}} = A_{\mathrm{p}} \cdot \left(a_{\mathrm{p1}} + a_{\mathrm{pa3}}\right)$	T1-liquid
3	$\rho \cdot A_{\mathrm{t}} \cdot y_{\mathrm{t1}} \cdot \ddot{y}_{\mathrm{t1}} + \rho \cdot A_{\mathrm{t}} \cdot \dot{y}_{\mathrm{t1}}^2 - \rho \cdot A_{\mathrm{p}} \cdot u_{\mathrm{p1}}^2 = \left(P_1 - P_{\mathrm{g,t1}}\right) \cdot A_{\mathrm{p}} - \rho \cdot \mathrm{g} \cdot A_{\mathrm{p}} \cdot y_{\mathrm{t1}} - \lambda_D \cdot \frac{\rho \cdot y_{\mathrm{t1}} \cdot A_{\mathrm{t}}}{2 \cdot d_{\mathrm{t}}} \cdot \dot{y}_{\mathrm{t1}} \cdot \left\lvert \dot{y}_{\mathrm{t1}} \right\rvert$	T1-liquid
4	$\rho \cdot A_{\mathrm{p}} \cdot u_{\mathrm{pa3}}^2 = \left(P_{\mathrm{g,t1}} - P_5\right) \cdot A_{\mathrm{p}} + \rho \cdot \mathrm{g} \cdot \left(y_{\mathrm{t1}} - y_5\right) \cdot A_{\mathrm{p}}$	T1-liquid
5	$\frac{\partial(\rho_{\mathrm{g,t1}} \cdot V_{\mathrm{g,t1}})}{\partial t} = \dot{m}_{\mathrm{g,t1,in}} - \rho_{\mathrm{g,t1}} \cdot \dot{Q}_{\mathrm{valve,t1}}$	T1-gas
6	$V_{\mathrm{g,t1}} = V_{\mathrm{t,t1}} - A_{\mathrm{t}} \cdot y_{\mathrm{t1}}$	T1-gas
7	$A_{\mathrm{t}} \cdot \dot{y}_{\mathrm{t2}} = A_{\mathrm{p}} \cdot \left(u_{\mathrm{pc3}} - u_{\mathrm{p2}}\right)$	T2-liquid
8	$A_{\mathrm{t}} \cdot \ddot{y}_{\mathrm{t2}} = A_{\mathrm{p}} \cdot \left(a_{\mathrm{pc3}} - a_{\mathrm{p2}}\right)$	T2-liquid
9	$\rho \cdot A_{\mathrm{t}} \cdot y_{\mathrm{t2}} \cdot \ddot{y}_{\mathrm{t2}} + \rho \cdot A_{\mathrm{t}} \cdot \dot{y}_{\mathrm{t2}}^2 + \rho \cdot A_{\mathrm{p}} \cdot u_{\mathrm{p2}}^2 = \left(P_{\mathrm{g,t2}} - P_2\right) \cdot A_{\mathrm{p}} + \rho \cdot \mathrm{g} \cdot A_{\mathrm{p}} \cdot y_{\mathrm{t2}} - \lambda_D \cdot \frac{\rho \cdot y_{\mathrm{t2}} \cdot A_{\mathrm{t}}}{2 \cdot d_{\mathrm{t}}} \cdot \dot{y}_{\mathrm{t2}} \cdot \left\lvert \dot{y}_{\mathrm{t2}} \right\rvert$	T2-liquid
10	$\rho \cdot A_{\mathrm{p}} \cdot u_{\mathrm{pc3}}^2 = \left(P_{\mathrm{g,t2}} - P_6\right) \cdot A_{\mathrm{p}} + \rho \cdot \mathrm{g} \cdot \left(y_{\mathrm{t2}} - y_6\right) \cdot A_{\mathrm{p}}$	T2-liquid
11	$\frac{\partial(\rho_{\mathrm{g,t2}} \cdot V_{\mathrm{g,t2}})}{\partial t} = \dot{m}_{\mathrm{g,t2,in}} - \rho_{\mathrm{g,t2}} \cdot \dot{Q}_{\mathrm{valve,t2}}$	T2-gas
12	$V_{\mathrm{g,t2}} = V_{\mathrm{t,t2}} - A_{\mathrm{t}} \cdot y_{\mathrm{t2}}$	T2-gas
13	$\rho \cdot A_{\mathrm{p}} \cdot L_{\mathrm{p1}} \cdot a_{\mathrm{p1}} = (P_4 - P_1) \cdot A_{\mathrm{p}} + \rho \cdot g \cdot A_{\mathrm{p}} \cdot (h_4 - h_1) - \left(\lambda_{D,\mathrm{p1}} \cdot \frac{\rho \cdot L_{\mathrm{p1}} \cdot A_{\mathrm{p}}}{2 \cdot d_{\mathrm{p}}} + \lambda_{L,\mathrm{p1}} \cdot \frac{\rho \cdot A_{\mathrm{p}}}{2}\right) \cdot u_{\mathrm{p1}} \cdot \left\lvert u_{\mathrm{p1}} \right\rvert$	P1
14	$\rho \cdot A_{\mathrm{p}} \cdot L_{\mathrm{p2}} \cdot a_{\mathrm{p2}} = (P_2 - P_3) \cdot A_{\mathrm{p}} + \rho \cdot g \cdot A_{\mathrm{p}} \cdot (h_2 - h_3) - \left(\lambda_{D,\mathrm{p2}} \cdot \frac{\rho \cdot L_{\mathrm{p2}} \cdot A_{\mathrm{p}}}{2 \cdot d_{\mathrm{p}}} + \lambda_{L,\mathrm{p2}} \cdot \frac{\rho \cdot A_{\mathrm{p}}}{2}\right) \cdot u_{\mathrm{p2}} \cdot \left\lvert u_{\mathrm{p2}} \right\rvert$	P2
15	$\rho \cdot A_{\mathrm{p}} \cdot L_{\mathrm{p3}} \cdot a_{\mathrm{p3}} = (P_3 - P_4) \cdot A_{\mathrm{p}} + \left(\lambda_{D,\mathrm{p3}} \cdot \frac{\rho \cdot L_{\mathrm{p3}} \cdot A_{\mathrm{p}}}{2 \cdot d_{\mathrm{p}}} + \lambda_{L,\mathrm{p3}} \cdot \frac{\rho \cdot A_{\mathrm{p}}}{2}\right) \cdot u_{\mathrm{p3}} \cdot \left\lvert u_{\mathrm{p3}} \right\rvert$	P3
16	$\rho \cdot A_{\mathrm{p}} \cdot L_{\mathrm{pa1}} \cdot a_{\mathrm{pa1}} = (P_4 - P_{4a}) \cdot A_{\mathrm{p}} - \lambda_{D,\mathrm{pa1}} \cdot \frac{\rho \cdot L_{\mathrm{pa1}} \cdot A_{\mathrm{p}}}{2 \cdot d_{\mathrm{p}}} \cdot u_{\mathrm{pa1}} \cdot \left\lvert u_{\mathrm{pa1}} \right\rvert$	Pa1
17	$\rho \cdot A_{\mathrm{pa2}} \cdot L_{\mathrm{pa2}} \cdot a_{\mathrm{pa2}} = \left(P_{4a} - P_{4b}\right) \cdot A_{\mathrm{pa2}} + \rho \cdot g \cdot A_{\mathrm{pa2}} \cdot \left(h_{4a} - h_{4b}\right) - \lambda_{D,\mathrm{pa2}} \cdot \frac{\rho \cdot L_{\mathrm{pa2}} \cdot A_{\mathrm{pa2}}}{2 \cdot d_{\mathrm{pa2}}} \cdot u_{\mathrm{pa2}} \cdot \left\lvert u_{\mathrm{pa2}} \right\rvert$	Pa2
18	$\rho \cdot A_{\mathrm{p}} \cdot L_{\mathrm{pa3}} \cdot a_{\mathrm{pa3}} = \left(P_{4b} - P_5\right) \cdot A_{\mathrm{p}} + \rho \cdot g \cdot A_{\mathrm{p}} \cdot \left(h_{4b} - h_5\right) - \left(\lambda_{D,\mathrm{pa3}} \cdot \frac{\rho \cdot L_{\mathrm{pa3}} \cdot A_{\mathrm{p}}}{2 \cdot d_{\mathrm{p}}} + \lambda_{L,\mathrm{pa3}} \cdot \frac{\rho \cdot A_{\mathrm{p}}}{2}\right) \cdot u_{\mathrm{pa3}} \cdot \left\lvert u_{\mathrm{pa3}} \right\rvert$	Pa3
19	$\rho \cdot A_{\mathrm{p}} \cdot L_{\mathrm{pc1}} \cdot a_{\mathrm{pc1}} = (P_3 - P_{3a}) \cdot A_{\mathrm{p}} - \lambda_{D,\mathrm{pc1}} \cdot \frac{\rho \cdot L_{\mathrm{pc1}} \cdot A_{\mathrm{p}}}{2 \cdot d_{\mathrm{p}}} \cdot u_{\mathrm{pc1}} \cdot \left\lvert u_{\mathrm{pc1}} \right\rvert$	Pc1
20	$\rho \cdot A_{\mathrm{pc2}} \cdot L_{\mathrm{pc2}} \cdot a_{\mathrm{pc2}} = \left(P_{3a} - P_{3b}\right) \cdot A_{\mathrm{pc2}} + \rho \cdot g \cdot A_{\mathrm{pc2}} \cdot \left(h_{3a} - h_{3b}\right) - \lambda_{D,\mathrm{pc2}} \cdot \frac{\rho \cdot L_{\mathrm{pc2}} \cdot A_{\mathrm{pc2}}}{2 \cdot d_{\mathrm{pc2}}} \cdot u_{\mathrm{pc2}} \cdot \left\lvert u_{\mathrm{pc2}} \right\rvert$	Pc2
21	$\rho \cdot A_{\mathrm{p}} \cdot L_{\mathrm{pc3}} \cdot a_{\mathrm{pc3}} = \left(P_{3b} - P_6\right) \cdot A_{\mathrm{p}} + \rho \cdot g \cdot A_{\mathrm{p}} \cdot \left(h_{3b} - h_6\right) - \left(\lambda_{D,\mathrm{pc3}} \cdot \frac{\rho \cdot L_{\mathrm{pc3}} \cdot A_{\mathrm{p}}}{2 \cdot d_{\mathrm{p}}} + \lambda_{L,\mathrm{pc3}} \cdot \frac{\rho \cdot A_{\mathrm{p}}}{2}\right) \cdot u_{\mathrm{pc3}} \cdot \left\lvert u_{\mathrm{pc3}} \right\rvert$	Pc3
22	$\rho \cdot u_{\mathrm{p2}} \cdot A_{\mathrm{p}} = \rho \cdot u_{\mathrm{p3}} \cdot A_{\mathrm{p}} + \rho \cdot u_{\mathrm{pc1}} \cdot A_{\mathrm{p}}$	node 3
23	$\rho \cdot a_{\mathrm{p2}} \cdot A_{\mathrm{p}} = \rho \cdot a_{\mathrm{p3}} \cdot A_{\mathrm{p}} + \rho \cdot a_{\mathrm{pc1}} \cdot A_{\mathrm{p}}$	node 3
24	$\rho \cdot u_{\mathrm{p3}} \cdot A_{\mathrm{p}} = \rho \cdot u_{\mathrm{p1}} \cdot A_{\mathrm{p}} + \rho \cdot u_{\mathrm{pa1}} \cdot A_{\mathrm{p}}$	node 4
25	$\rho \cdot a_{\mathrm{p3}} \cdot A_{\mathrm{p}} = \rho \cdot a_{\mathrm{p1}} \cdot A_{\mathrm{p}} + \rho \cdot a_{\mathrm{pa1}} \cdot A_{\mathrm{p}}$	node 4
26	$\rho \cdot u_{\mathrm{pc1}} \cdot A_{\mathrm{p}} = \rho \cdot u_{\mathrm{pc2}} \cdot A_{\mathrm{pc2}} = \rho \cdot u_{\mathrm{pc3}} \cdot A_{\mathrm{p}}$	nodes 3a/3b
27	$\rho \cdot a_{\mathrm{pc1}} \cdot A_{\mathrm{p}} = \rho \cdot a_{\mathrm{pc2}} \cdot A_{\mathrm{pc2}} = \rho \cdot a_{\mathrm{pc3}} \cdot A_{\mathrm{p}}$	nodes 3a/3b
28	$\rho \cdot u_{\mathrm{pa1}} \cdot A_{\mathrm{p}} = \rho \cdot u_{\mathrm{pa2}} \cdot A_{\mathrm{pa2}} = \rho \cdot u_{\mathrm{pa3}} \cdot A_{\mathrm{p}}$	nodes 4a/4b
29	$\rho \cdot a_{\mathrm{pa1}} \cdot A_{\mathrm{p}} = \rho \cdot a_{\mathrm{pa2}} \cdot A_{\mathrm{pa2}} = \rho \cdot a_{\mathrm{pa3}} \cdot A_{\mathrm{p}}$	nodes 4a/4b

In addition to the equations of the above table, the gas flow rate exiting the system when the valves open was calculated using equations 4.7 and 4.8 as were described in chapter 4. Moreover, the gas entering the flash tanks was calculated using the Faraday equations 2.7 and 2.8 for O_2 (tank T1) and H_2 (tank T2) respectively (multiplied by the molar masses of the components to have the right units).

A.3. SIMULINK

The system of equations presented in table A.1 was implemented and solved in Simulink. As discussed in sub-section 4.2.4, the rapid variations of the system's parameters (pressures, velocities, electrolyte level in the flash tanks) make the problem stiff and for this reason, the variable time step option was selected. For this option, the software provides both explicit and implicit solvers. The implicit solvers are recommended in the software documentation [3] because they are designed for stiff problems and can be more efficient and faster in cases that the explicit solvers fail or crashing. The offered solvers for the variable time step option are listed below:

EXPLICIT SOLVERS (NON-STIFF):

- **ode45**: Based on a Runge-Kutta (4,5) pair (known also as Dormand-Prince method), which is a fifth-order method with fourth-order error estimation.
- **ode23**: Based on a Runge-Kutta (2,3) pair (known also as Bogacki-Shampine method), which is a third-order error estimation method. It is documented to be more efficient for problems that ode45 fails to solve and for problems with mild-stiffness.
- **ode113**: This is a variable order solver (based on Adams-Bashforth-Moulton method). It is recommended for problems with strict error tolerance or when ode45 fails.

IMPLICIT SOLVERS (STIFF):

- **ode15s**: A variable order solver, based on the numerical differentiation formulas (NDF).
- **ode23s**: Based on a modified second-order Rosenbrock method, can be more efficient in problems where ode15s fails.
- **ode23t**: This method is based on the trapezoidal rule. It is recommended for problems with moderate stiffness and is also free of numerical damping.
- **ode23tb**: This method uses TR-BDF2, which is an implicit two-stage Runge-Kutta formula. The first stage uses the trapezoidal rule and the second implements a second-order backward differentiation formula. The method can solve problems where ode15s fails.

The solution of the developed system of equations was iteratively calculated at each time step. Simulink detects automatically the algebraic variables, depending on how the user has defined the equations and tries to find a solution using an algebraic loop solver. MATLAB offers two different algorithms to solve algebraic loops: the Trust-Region and the Line-Search. In this project, the Trust-Region solver was used, which is also the default option of the program.

From the solvers mentioned above, several tests were done to select the one that offers a stable solution for the specific model. The system is computationally demanding because of the large number of equations and the main problem was the random crashes that happened during the simulations. From the solvers mentioned above, the implicit ode23s was the one selected since it ran smoothly and converged without any crashes. Apart from that, the explicit ode23 managed to converge without crashes. Moreover, the selected error tolerance was set to 10^{-4} by taking into account both accuracy and computational time. Furthermore, a maximum limit of 15 ms was set for the time step.

B

CROSSOVERS MODEL

B.1. GAS SOLUBILITY IN AQUEOUS POTASSIUM HYDROXIDE

This section describes the model implemented by Haug [20] to calculate the solubility of O_2 and H_2 inside aqueous KOH solutions. The method uses the Sechenov correlation, which relates a dissolved component concentration in aqueous KOH solution to that in pure water as a function of salt mass fraction.

$$\log\left(\frac{c^*_{i,H_2O}}{c^*_i}\right) = k_{S,i} \cdot w_{KOH} \tag{B.1}$$

where c^*_{i,H_2O} and c^*_i are the component i solubilities in pure water and aqueous KOH respectively, w_{KOH} is the mass fraction of the salt in the solution and $k_{S,i}$ is the Sechenov constant. This constant was estimated in [20] using experimental data provided by Knaster et al [28], who conducted experiments at 75 ^{o}C.

Table B.1: Sechenov constants for O_2 and H_2. These values are valid for KOH mass fractions from 5.4 wt% to 39.8 wt% [20].

Component	k_S [-]
O_2	3.66
H_2	3.14

The gas solubility in pure water was calculated by firstly estimating the Henry constant. The following empirical formula [20] relates the Henry constant of the dissolved in pure water gases to the operating temperature (valid for temperatures 273-647 K).

$$A \cdot \left(\log \bar{K}^{px}_{H,i}\right)^2 + B \cdot \left(\frac{1}{\bar{T}}\right)^2 + C \cdot \left(\log \bar{K}^{px}_{H,i}\right) \cdot \left(\frac{1}{\bar{T}}\right) + D \cdot \left(\log \bar{K}^{px}_{H,i}\right) + E \cdot \left(\frac{1}{\bar{T}}\right) - 1 = 0 \tag{B.2}$$

where $\bar{K}^{px}_{H,i} = K^{px}_{H,i} \cdot 10^{-4}$ and $\frac{1}{\bar{T}} = \frac{1}{T} \cdot 10^3$. The parameter K^{px}_H (in bar) is the Henry constant expressed as the partial pressure above the water (p) in bar over the molar mixing ratio in the liquid phase (x), while T is the operating temperature in K.

Table B.2: Parameters A-E used in eq. B.2 to estimate the Henry constant in pure water.

Gas	A	B	C	D	E
O_2	-0.0005943	-0.147	-0.0512	-0.1076	0.8447
H_2	-0.1233	-0.1366	0.02155	-0.2368	0.8249

The component i solubility in pure water was estimated using the following formula:

$$c^*_{i,H_2O} = \frac{\rho_{H_2O}}{M_{H_2O}} \cdot \frac{p_i}{K^{px}_{H,i}} \tag{B.3}$$

where ρ_{H_2O} is the density of water (in kg·m^{-3}) , M_{H_2O} is the molar mass of water (in kg·mol^{-1}), p_i is the partial pressure of component i above water (in bar) and $K^{px}_{H,i}$ the estimated from equation B.2 Henry constant (in bar).

Finally, the solubility of component i in aqueous KOH (30 wt% for this project) at different pressures was calculated using equation B.1.

B.2. NODES NUMBER DEPENDENCE STUDY

The 1-d transient advection-diffusion equation was solved multiple times at each time step for the various elements of the hydraulic network and the separators (fig. 4.4). A dependence study on the number of used nodes was conducted to ensure the accuracy of the transient solution, having as main constraint the computational power of the used computer (8 GB of RAM). The same number of nodes was applied for the spatial discretization of the pipe elements (P1, P2, P3, Pa1 and Pc1) and a different number for the separators.

Firstly, 50 nodes were selected for the separators and the pipe nodes number was gradually increased. Figures B.1 and B.2 illustrate how the variables of interest (crossed-over gases content) are affected by the number of pipe nodes.

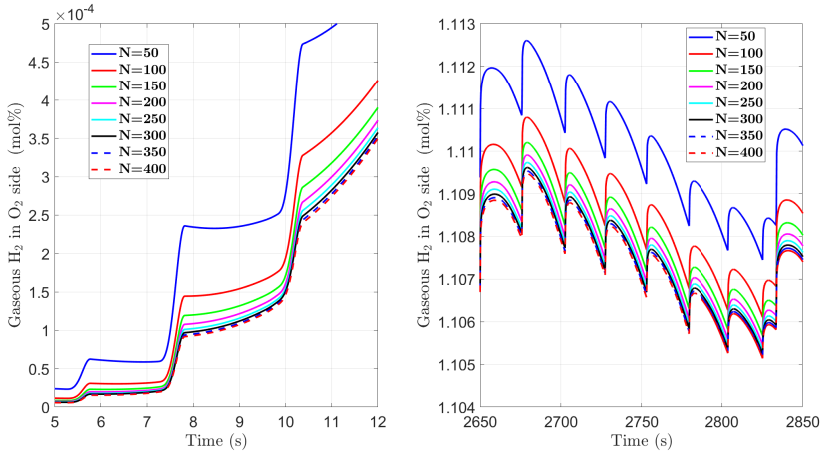

Figure B.1: Pipe nodes number effect on gas H_2 content in the O_2 side early in the startup (left graph) and during the main operation (right graph). The separator number of nodes was kept fixed to 50.

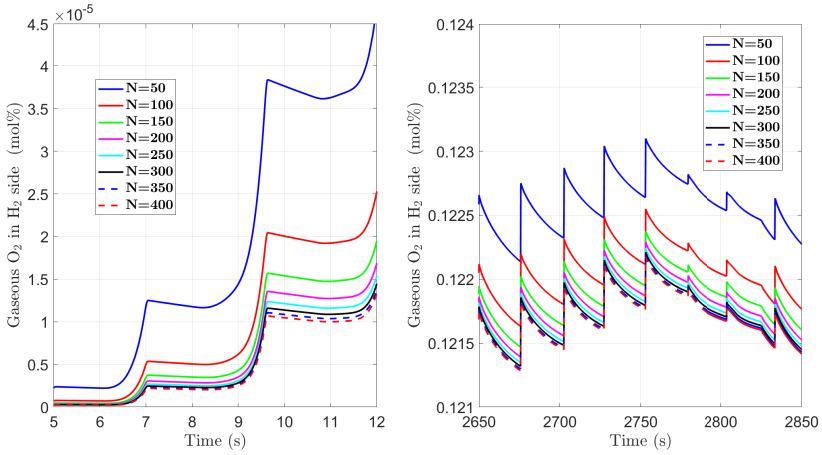

Figure B.2: Pipe nodes number effect on gas O_2 content in the H_2 side early in the startup (left graph) and during the main operation (right graph). The separator number of nodes was kept fixed to 50.

To be able to see the different solutions, two graphs are used in the above figures, where the left one focuses on a time interval during the startup, while the right one focuses on the main operating state. As can be seen, above 300 nodes (black line in all graphs), the solution remains almost the same for both H_2 and O_2 crossover and that was the selected value.

Subsequently, having selected 300 nodes for the pipe elements, a similar study was performed for the used nodes in the spatial discretization of the separators.

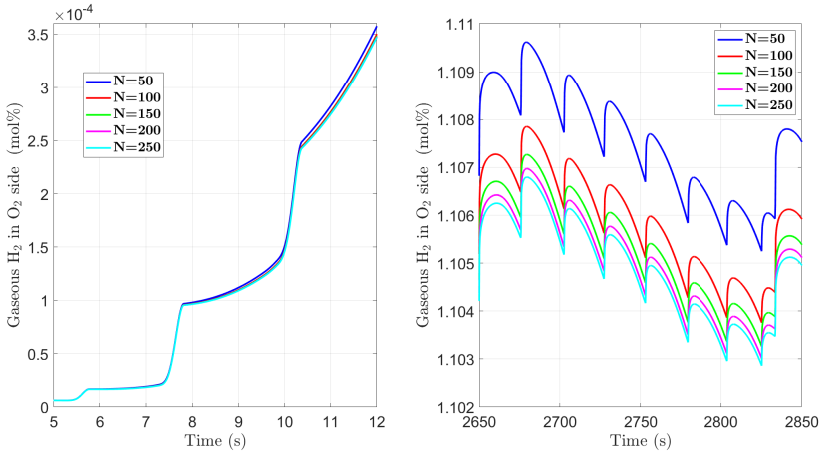

Figure B.3: Separator nodes number effect on gas H_2 content in the O_2 side early in the startup (left graph) and during the main operation (right graph). The pipe number of nodes was set to 300 as resulted from the previous analysis.

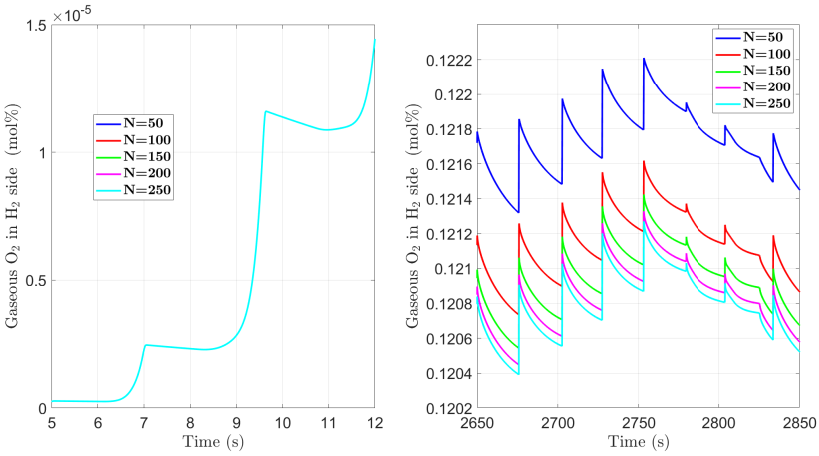

Figure B.4: Separator nodes number effect on gas O_2 content in the H_2 side early in the startup (left graph) and during the main operation (right graph). The pipe number of nodes was set to 300 as resulted from the previous analysis.

Observing figures B.3 and B.4, a conclusion can be made only from the main operating state (right graphs) since at the startup (left graphs) the lines almost coincide. The difference between the lines becomes less significant for more than 150 nodes. Thus the final selection for the separator was 200 nodes.

B.3. TRIDIAGONAL MATRIX ALGORITHM

In the crossovers model, a time-implicit numerical scheme was implemented to solve the transient advection-diffusion equation in the relevant elements and predict the mass transport of the dissolved gases in the system (eq. 4.22 or 4.23 depending on the flow direction). The used implicit scheme leads to a tridiagonal system of equations and has the following general form:

$$a_i \cdot x_{i-1} + b_i \cdot x_i + c_i \cdot x_{i+1} = d_i \tag{B.4}$$

or in matrix form:

$$\begin{bmatrix} b_1 & c_1 & 0 & 0 & 0 & 0 \\ a_2 & b_2 & c_2 & 0 & 0 & 0 \\ 0 & a_3 & b_3 & c_3 & 0 & 0 \\ & & \ddots & \ddots & \ddots & \\ 0 & 0 & 0 & a_{N-1} & b_{N-1} & c_{N-1} \\ 0 & 0 & 0 & 0 & a_N & b_N \end{bmatrix} \cdot \begin{bmatrix} x_1 \\ x_2 \\ x_3 \\ \vdots \\ x_{N-1} \\ x_N \end{bmatrix} = \begin{bmatrix} d_1 \\ d_2 \\ d_3 \\ \vdots \\ d_{N-1} \\ d_N \end{bmatrix}$$

where $a_1 = c_N = 0$. The matrix including a, b and c is tridiagonal because the non-zero elements are located in the main diagonal (b_i), the upper diagonal (c_i) and the lower diagonal (a_i). This type of system is solved using the TDMA method or Thomas algorithm [56], which is based on a simplified Gaussian elimination method. The algorithm starts with a forward elimination of the arrays as:

$$i = 1 \;\rightarrow\; \tilde{c}_i = \frac{c_i}{b_i} \quad \text{and} \quad \tilde{d}_i = \frac{d_i}{b_i}$$

$$i = 2,3,\cdot\cdot,N \;\rightarrow\; \tilde{c}_i = \frac{c_i}{b_i - a_i \cdot \tilde{c}_{i-1}} \quad \text{and} \quad \tilde{d}_i = \frac{\tilde{d}_i - a_i \cdot \tilde{d}_{i-1}}{b_i - a_i \cdot \tilde{c}_{i-1}}$$

The solution x is found by backward substitution as:

$$i = N \;\rightarrow\; x_N = \tilde{d}_N$$
$$i = N-1, N-2, \cdot\cdot, 1 \;\rightarrow\; x_i = \tilde{d}_i - \tilde{c}_i \cdot x_{i+1}$$